INFLUENCE OF PROCESSING VARIABLES ON THE MORPHOLOGY AND MICROSTRUCTURE OF A NON-STOICHIOMETRIC COMPLEX CONCENTRATED ALLOY

by

AIDAN M. MITCHELL

MARK L. WEAVER, COMMITTEE CHAIR
LIN LI
MATTHEW KASEMER

A THESIS

Submitted in partial fulfillment of the requirements
for the degree of Master of Science
in the Department of Metallurgical and Materials Engineering
in the Graduate School of
The University of Alabama

TUSCALOOSA, ALABAMA

2022

Copyright Aidan M. Mitchell 2022
ALL RIGHTS RESERVED

ABSTRACT

The development of high-entropy alloys has been a major area of research in recent years. The compositionally complex alloy $Al_{10}Co_{25}Cr_8Fe_{15}Ni_{36}Ti_6$ has been promoted as an optimized chemistry exhibiting medium hardness with good ductility and high tensile strength. This thesis aims to provide insight into the growth of $Al_{10}Co_{25}Cr_8Fe_{15}Ni_{36}Ti_6$ as a surface coating and into the influence of coating morphology on its interdiffusion behavior. Coatings were deposited via high rate unbalanced direct current magnetron sputtering. Deposition conditions were selected to survey processing-property relations relative to the structure zone model for thick film growth proposed by Thornton. Thick micro-scale coatings were deposited onto CMSX-8 Ni-based superalloy substrates at various temperatures and Ar gas pressures and later annealed to observe diffusion behavior. Coating morphology, chemical analysis, and crystallographic identification were performed using scanning electron microscopy, energy-dispersive x-ray spectroscopy, and x-ray diffraction. Coatings produced at 5 mTorr Ar pressure displayed dense Zone T or mixed Zone T + Zone 2 morphologies and the least amount of diffusion into the substrate upon annealing. Some of the samples at high pressures and temperatures possessed porous, fibrous Zone 2 morphologies caused by a high incident angle between the substrate and sputter gun.

LIST OF ABBREVIATIONS AND SYMBOLS

at%	Atomic percent
BCC	Body centered cubic
CCA	Complex concentrated alloy
DC	Direct current
EDS	Energy-dispersive x-ray spectroscopy
FCC	Face centered cubic
HCP	Hexagonal close packed
HEA	High entropy alloy
SEM	Scanning electron microscopy
VEC	Valence electron concentration
XRD	X-ray diffraction
ΔH_{mix}	Standard enthalpy of mixing
ΔS_{mix}	Ideal configuration entropy of mixing
$\Delta\chi$	Electronegativity difference
δ	Atomic size difference
Ω	Empirical HEA phase formation factor
B2	Ordered BCC crystal structure
$L1_2$	Ordered FCC crystal structure

ACKNOWLEDGEMENTS

I'd like to take this opportunity to thank my advisor, Dr. Mark L. Weaver. His continued encouragement and support made this thesis possible.

I'd also like to thank my committee members Dr. Lin Li and Dr. Matthew Kasemer for their assistance and guidance.

This research was partially supported by National Science Foundation grant number DMR-2105364.

Lastly, to all my friends and family, I thank them for their endless and at times overbearing support through the research process.

CONTENTS

ABSTRACT ii

LIST OF ABBREVIATIONS AND SYMBOLS iii

ACKNOWLEDGEMENTS iv

LIST OF TABLES vii

LIST OF FIGURES viii

CHAPTER 1: INTRODUCTION 1

1.1 General Background 1

1.2 Motivation 2

CHAPTER 2: LITERATURE REVIEW 5

2.1 Background on HEAs 5

2.2 Four Core Effects of HEAs 6

2.2.1 High entropy 6

2.2.2 Sluggish Diffusion 7

2.2.3 Severe lattice distortion 7

2.2.4 Cocktail effect 8

2.3 Influences of Core Effects 8

2.4 HEA Phase Formation Rules 9

2.5 High Entropy Superalloys 12

2.6 HEA Composition Optimization 13

2.7 HEA Coatings.....15

CHAPTER 3: EXPERIMENTAL PROCEDURES.....18

3.1 Sputtering Target and Substrate Preparation.....18

3.2 Coating Deposition.....21

3.3 Heat Treatment.....23

3.4 Structural Analysis.....23

CHAPTER 4: RESULTS AND DISCUSSION.....25

4.1 Heating Stage Temperature Gradient.....25

4.2 Series 1 Coatings – Initial Screening.....28

4.3 Series 2 Coatings – As Deposited.....30

4.4 Series 2 Coatings - Annealed.....39

4.5 Series 3 Coatings – Thicker Coatings After Annealing.....39

CHAPTER 5: SUMMARY, CONCLUSIONS AND FUTURE WORK.....47

5.1 Summary and Conclusions.....47

5.2 Future Work.....48

REFERENCES.....50

APPENDIX A: TEMPERATURE GRADIENT DERIVATION.....62

APPENDIX B: COMPOSITION PROFILES FOR AS-DEPOSITED SERIES 2 COATINGS .65

APPENDIX C: COMPOSITION PROFILES FOR ANNEALED SERIES 2 COATINGS.....77

APPENDIX D: SHORT OVERVIEW OF STRUCTURE ZONE MODELS IN PVD.....90

LIST OF TABLES

Table 2-1. Ideal mixing entropies for common alloys. 6

Table 3-1: Composition of alloy sputtering targets and CMSX-8 substrates.....20

Table 3-2: Deposition series 1 - 30-minute deposition working conditions. 22

Table 3-3: Deposition Series 2, 1.5-hour deposition working conditions and heat treatments.....22

Table 3-4: Deposition series 3, 3-hour deposition working conditions and heat treatments. 23

Table 4-1: Thickness measurements for Series 1 depositions. 29

Table 4-2: Thickness measurements of as deposited Series 2 coatings. 33

Table 4-3: IDZ measurements of annealed Series 2 coatings. 40

Table 4-4: Thickness and IDZ measurements of Series 3 coatings. 43

Table 4-5: Composition of separated FCC and B2 phases after 1-hour 1000 °C anneal.....43

LIST OF FIGURES

Figure 2-1. Different alloy classes based on entropy. 5

Figure 2-2. A plot of δ versus ΔH_{mix} for the alloy investigated in this study. 13

Figure 2-3: As-cast $Al_{10}Co_{25}Cr_8Fe_{15}Ni_{36}Ti_6$ adapted from Butler et al. [46]. 15

Figure 2-4: Structure zone model for predicting coating morphology. 17

Figure 3-1: Positioning of samples on substrate plate. 19

Figure 4-1: A picture of the substrate plate showing the temperature gradient. 26

Figure 4-2: Temperature distributions across the substrate plate. 27

Figure 4-3: Cross section and topography images of some as-deposited Series 1 coatings. 32

Figure 4-4: Cross section and topography images of as-deposited Series 2 coatings. 34

Figure 4-5: Structure zone model for the Series 2 coatings deposited in this study. 35

Figure 4-6: XRD patterns of as-deposited coatings produced at 5 mTorr working pressure.....36

Figure 4-7: XRD patterns of as-deposited coatings produced at 15 mTorr working pressure.....37

Figure 4-8: XRD patterns of as-deposited coatings produced at 30 mTorr working pressure.....38

Figure 4-9: Cross section images and composition profiles for annealed Series 2 coatings.....41

Figure 4-10: Cross section images of the annealed Series 3 coatings (300W, 5 mTorr). 44

Figure 4-11: XRD patterns for Series 3 coatings.....45

Figure B-1: Center, Series 2 coating deposited at 5 mTorr. 66

Figure B-2: Position 2, Series 2 coating deposited at 5 mTorr. 67

Figure B-3: Position 3, Series 2 coating deposited at 5 mTorr. 68

Figure B-4: Edge, Series 2 coating deposited at 5 mTorr. 69

Figure B-5: Position 2, Series 2 coating deposited at 15 mTorr. 70

Figure B-6: Position 3, Series 2 coating deposited at 15 mTorr. 71

Figure B-7: Edge, Series 2 coating deposited at 15 mTorr. 72

Figure B-8: Center, Series 2 coating deposited at 30 mTorr. 73

Figure B-9: Position 2, Series 2 coating deposited at 30 mTorr. 74

Figure B-10: Position 3, Series 2 coating deposited at 30 mTorr. 75

Figure B-11: Edge, Series 2 coating deposited at 30 mTorr. 76

Figure C-1: Center, annealed Series 2 coating deposited at 5 mTorr. 78

Figure C-2: Positon 2, annealed Series 2 coating deposited at 5 mTorr. 79

Figure C-3: Position 2, annealed Series 3 coating deposited at 5 mTorr. 80

Figure C-4: Edge, annealed Series 2 coating deposited at 5 mTorr. 81

Figure C-5: Center, annealed Series 2 coating deposited at 15 mTorr. 82

Figure C-6: Position 2, annealed Series 2 coating deposited at 15 mTorr. 83

Figure C-7: Position 2, annealed Series 3 coating deposited at 15 mTorr. 84

Figure C-8: Edge, annealed Series 2 coating deposited at 15 mTorr. 85

Figure C-9: Center, annealed Series 2 coating deposited at 30 mTorr. 86

Figure C-10: Position 2, annealed Series 2 coating deposited at 30 mTorr. 87

Figure C-11: Position 3, annealed Series 2 coating deposited at 30 mTorr. 88

Figure C-12: Edge, Series 2 coating deposited at 30 mTorr. 89

Figure D-1: Structure zone model for thermally evaporated thick films [134].....90

Figure D-2: Structure zone model for predicting coating morphology [25]. 91

Figure D-3: Structure zone model that includes Zone M [124].....93

Figure D-4: Modified SZM showing expansion of Zone T with increasing bombardment. 94

Figure D-5: Grovernor's SZM for evaporated metal films [51]. 95

CHAPTER 1: INTRODUCTION

1.1 General Background

High-entropy alloys (HEAs) have become an increasingly important field of alloy design and application. The basis for these new alloys primarily comes from the seminal studies from Cantor and Yeh [1]. The nomenclature for this classification of alloys describes the incredibly high entropy of mixing these materials possess compared to traditional alloys [2-6]. HEAs feature five or more elemental components often mixed in equiatomic or near-equiatomic concentrations, typically ranging between 3 – 35 atomic %. Many HEAs form simple solid solution phases with high symmetry face-centered cubic, body-centered cubic, or hexagonal close packed crystal structures which impart them with often unique physical, chemical, and mechanical properties compared to conventional alloys [1,4,7,8]. This opens the door for HEAs to be used in some existing and future engineering applications [2,3,9-12]. Though the formation of compositionally complex, single phase solid solution alloys remains one of the founding ideas driving HEA research, it has become evident that most of the so-called HEAs are multi-phase and are non-stoichiometric [13]. This broader range of compositions and microstructures, which has been extended downwards to include alloys consisting of three or more principal elements with element concentrations often greater than 35%, have been captured in the related names complex concentrated alloys or compositionally complex alloys (i.e., CCAs), baseless alloys, multi-principal element alloys (MPEAs), and metal buffets (MBs) [14].

From an alloy design perspective, HEAs and CCAs, due to their reportedly high ranges of solid solubility, offer immense potential for fine tuning of alloy composition to achieve desirable

microstructures and properties [5]. This flexibility has stimulated considerable interest from the thin films and coatings communities (some recent reviews are provided in the following references, [9,14-23]). This attention is primarily driven by desires to exploit their higher hardness, favorable wear and corrosion resistance, and purported resistance to diffusion. HEA/CCA coatings have been fabricated in a variety of ways including laser or plasma cladding, vacuum arc deposition, thermal spraying, cold spraying, evaporating, electrodeposition, and magnetron sputtering [24]. Though it is certainly not the fastest method of deposition, magnetron sputtering offers several advantages with regards to coating or thin film development [25,26]. With sputtering it is possible to produce metals, ceramics, multilayers and composites with high dimensional precision and good composition control. Furthermore, through careful control of deposition conditions such as substrate temperature and/or bias, working gas pressure, and reactive gases, film/coating morphology (i.e., grain size and shape) and microstructure can be tailored making this technique viable as a high-throughput material development tool for new materials [15,26-29]. As such, it is important to establish the influences of various deposition parameters on the resulting microstructures.

1.2 Motivation

The SCOPUS abstract and citation database lists more than 250 investigations of magnetron sputtered HEA thin films and coatings, some (but not all) of which are summarized in references [18,19,26,30-41]. In all this work, there has been only one systematic study to focus on the influences of substrate temperature and working gas pressure on film/coating morphology in metallic films [41]. The motivation for this study was to investigate the influences of those deposition parameters on the morphologies and microstructures of thick films of the

$Al_{10}Co_{25}Cr_8Fe_{15}Ni_{36}Ti_6$ CCA when grown at high rates via direct current (DC) unbalanced magnetron sputtering.

The $Al_{10}Co_{25}Cr_8Fe_{15}Ni_{36}Ti_6$ CCA and more recently derived variants have been mentioned as potential replacements for high temperature steels and more expensive Ni-based superalloys or for use as high temperature coatings due to their high tensile strengths and favorable resistances to chemical attack and environmental degradation [10,12,33,41-48]. Focusing on the coating application; next to nothing is known about how the structure of this alloy evolves when it is processed via magnetron sputtering. Because the fabrication of dense and conformal thin films and coatings will be required if HEAs are to achieve practical use in those forms, this thesis will investigate the influences of processing variables on the microstructures of thick HEA coatings of $Al_{10}Co_{25}Cr_8Fe_{15}Ni_{36}Ti_6$ produced via direct current (DC) magnetron sputtering. Since being proposed by Thornton, the structures and properties of physical vapor deposited thin films and coatings have been widely discussed on the basis of the SZM [49-56]. Only a few studies focusing on HEAs have broached this subject [39,41,57-60], often indirectly. Of those only Savan et al. have approached it systematically [41].

This thesis will contribute towards the systematic evaluation of the changes in film morphology/structure of concentrated alloys such as HEAs as functions of homologous substrate-temperature and working gas pressure. This thesis will also contribute towards the development of combinatorial studies using magnetron sputtering. In recent years there has been a proliferation of such studies, some of which can be found in the following references, [28,29,61-70]. However, many researchers do not address the morphology of the deposited materials which is certain to influence microstructures, properties, and related material behaviors. If accurate correlations between thin film or coating materials and bulk materials,

more thorough elucidation of morphology is needed. This work will also contribute towards improved combinatorial work by considering the changes that occur when depositing coatings via magnetron sputtering under conditions where a temperature gradient exists across the substrate plate along with regions where deposition occurs at oblique angles of incidence.

CHAPTER 2: LITERATURE REVIEW

2.1 Background on HEAs

High entropy alloys are by their original definition alloys that are composed of five or more elemental constituents in equiatomic or near-equiatomic ratios (i.e., ~5 to 35 at%) [5,9,71]. Miracle et al. then further devised a unique interpretation that coupled the entropy argument $\Delta S_{mix} \geq 1.5R$ (where R is the ideal gas constant) along with the standard definition of HEAs [9]. Alloys satisfying this entropy requirement are considered high-entropy, while those below are classified as medium-entropy or low-entropy, as shown in Fig. 2-1 [71]. Table 2-1 shows the ideal mixing entropies calculated for some common alloys, along with those for four, five, six, and seven element equiatomic alloys [9]. It is evident that many common alloys that exhibit a single dominant constituent display medium or low ideal mixing entropies. Likewise, equiatomic alloys with five or more elements all exhibit a high entropy character.

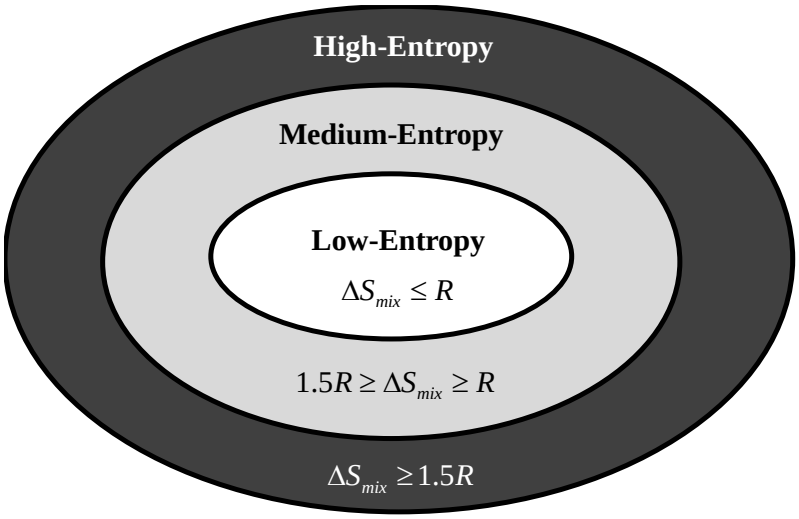

Figure 2-1. Different alloy classes based on entropy. Adapted from reference [71].

Table 2-1. Ideal Mixing Entropies for Common Alloys. Adapted from reference [71].

Alloy	ΔS_{mix} (ideal)
Inconel 718	1.31R (medium entropy)
Hastelloy X	1.37R (medium entropy)
Al Alloy 7075	0.43R (low entropy)
316 Stainless steel	1.15R (medium entropy)
304 Stainless steel	0.96R (low entropy)
4340 Low-alloy steel	0.22R (low entropy)
Equiatomic 4 element HEA	1.39R (medium entropy)
Equiatomic 5 element HEA	1.61R (high entropy)
Equiatomic 6 element HEA	1.79R (high entropy)
Equiatomic 7 element HEA	1.95R (high entropy)

2.2 Four Core Effects of HEAs

The microstructures and properties of HEAs are postulated to be determined by four core effects: (1) high entropy, (2) sluggish diffusion, (3) severe lattice distortion, and (4) the cocktail effect. Each effect is briefly reviewed below.

2.2.1 High entropy

Initially, it was proposed that increased configurational entropy in equimolar or near-equimolar alloys containing five or more constituent elements can favor the formation of single phase solid solution microstructures with simple BCC, FCC, or HCP crystal structures [72,73]. However, more recent analysis of published literature indicates that configurational entropy

alone doesn't determine phase formation [5]. Instead, entropy and enthalpy must be considered together.

2.2.2 Sluggish Diffusion

Sluggish diffusion was proposed to occur in HEAs due to large variations in potential energy between lattice sites [72,74]. Tsai et al. noted that Co, Cr, Fe, Mn, and Ni all displayed slower diffusion rates in high entropy CoCrFeMnNi matrices than in pure metals or in less complex alloys composed of the same or similar constituents which they attributed to differences in the activation energies for self-diffusion [74]. These results were later examined by Beke et al. [75] who reported that the differences in the diffusion rates were more likely due to temperature insensitive correlation factors inherent to compositionally complex HEAs. Kulkarni et al. [76] investigated interdiffusion in quaternary FeNiCoCr alloys, ultimately concluding that diffusional interactions between components is strong and must be considered when assessing diffusion effects. More recently, Dabrowa and co-workers [77-79], Osetsky et al. [80], and Mehta and Sohn [81,82] have revealed additional structural and kinetic contributors to diffusion in HEAs that cast some doubt on its occurrence. Miracle and Senkov [5] noted that the diffusion coefficients in some HEAs are higher than those in conventional materials when compared at the same temperatures. Though the concept of sluggish diffusion kinetics is still being debated, there is little doubt that diffusivity is altered in some way in HEAs in comparison with conventional alloys and that this could have an influence on the evolution of microstructure during sputter deposition.

2.2.3 Severe lattice distortion

Severe lattice distortion was proposed to arise from an atomic size mismatch caused by the inclusion of different atom types in solid solution and is enhanced by non-symmetrical bond

energies and electronic structures [71]. It has been postulated that this could ultimately lead to a diminished sensitivity to temperature effects [71]. Severe lattice distortion has also been inferred to explain the relatively high strengths observed in HEAs [71,72,83,84]. However, it has been noted that this effect has not been sufficiently quantified to judge its occurrence or influence [5,85,86].

2.2.4 Cocktail effect

The cocktail effect has been described as ranging from an atomic-scale multi-element composite effect to a micro-scale multiphase composite effect depending upon alloy composition, constitution (i.e., number of phases), and processing method [87]. These same phenomena are observed in conventional metal alloys but are generically reported to be far more significant in HEAs. As such, Yeh describes them as useful guidelines for HEA design for specific purposes or applications [2].

2.3 Influences of Core Effects

In their review papers, Pickering and Jones [88] and Miracle and Senkov [5] have noted that none of the reported core effects may be as significant as initially believed. Very few experimental examples of entropic stabilization of solid solution phases have been reported. Both experimental results and theory suggest that intermetallic phase formation or phase separation are more likely consequences of the addition of more components to an alloy. Furthermore, very limited evidence exists concerning the extent of lattice strain in HEAs. It can be hypothesized based on Hume-Rothery type arguments that high lattice strains (aka, severe lattice distortion) would promote rapid intermetallic phase formation. In some cases, the normalized activation energies for diffusion in HEAs are higher than in conventional alloys; however, the effect of variations in the pre-exponential factor, Do, must be accounted for.

Reports of rapid precipitation or phase separation in HEAs suggests that diffusion kinetics are not slow at all. It is also not clear what the cocktail effect refers to and how this effect differs from observations made of conventional alloys.

2.4 HEA Phase Formation Rules

A set of empirically determined factors, termed the phase formation rules, have been developed to facilitate the prediction of the numbers and types of phases that could form in each alloy based on its chemical composition. These rules were originally used to aid in the design of single phase, solid solution HEAs. The phase formation rules are not the emphasis of this thesis, but an understand of them is essential to fully understand the basic methodology behind HEAs.

There are six factors encompassed in the rules as categorized in the literature: δ, ΔH_{mix}, ΔS_{mix}, Ω, $\Delta\chi$, and VEC [2,72,83,84,89-98]. The enthalpy of mixing, ΔH_{mix}, is defined by:

$$\Delta H_{mix} = \sum_{i=1, i\neq j}^{n} \Omega_{ij} C_i C_j \tag{1}$$

and

$$\Omega_{ij} = 4\Delta H_{ij}^{mix} \tag{2}$$

where C_i and C_j are the concentration of components i and j, respectively. The term ΔH_{ij}^{mix} is an interaction parameter based on the Miedema model for binary liquid alloys [99]. Having a near zero or negative enthalpy of mixing is generally ideal since it allows entropy ΔS_{mix} to dominate in the Gibbs free energy expression $\Delta G_{mix} = \Delta H_{mix} - T\Delta S_{mix}$ [2,72,89,90,98]. This entropy dominance has been experimentally shown to destabilize intermetallic phases, with ΔH_{mix} typically in the range of −15 to 5 kJ/mol [72,89,92,97,98].

The configurational entropy of mixing, ΔS_{mix}, is defined by [71,92,100]:

$$\Delta S_{mix} = -R \sum_{i=1}^{n} C_i \ln(C_i) \tag{4}$$

where C_i is the concentration of component i and R is the ideal gas constant (8.314 $JK^{-1}mol^{-1}$). In this expression, only the configurational component of entropy is included, since it is assumed to dominate over the other three contributions: vibrational, electronic, and magnetic [71]. This definition is based on a regular solution model and is only dependent on the relative composition of the alloy. Some of the literature suggests that this term is ideal for the formation of solid solution phases when in excess of $1.61R$ [72,89,97,98]. This restricts quinary HEAs to only include equiatomic compositions where the entropy is maximized [71]. However, many of the quinary HEAs in the literature that exhibit solid solution type microstructures are not equiatomic [89,101]. Thus, as mentioned previously, the remainder of this dissertation will assume high-entropy character corresponds to $\Delta S_{mix} \geq 1.5R$ [5,71].

The electronegativity difference, $\Delta\chi$, is defined by [72,89,91]:

$$\chi = \left[\sum_{i=1}^{n} C_i \left(\chi_i - \bar{\chi}\right)^2\right]^{1/2} \tag{4}$$

and

$$\bar{\chi} = \sum_{i=1}^{n} C_i \chi_i \tag{5}$$

where χ_i is the Pauling electronegativity for component i. Based on the Hume-Rothery rules, large electronegativity differences between alloying elements stabilize compound formation [89,92]. Thus, the retention of simple solid solution microstructures in HEAs requires small values of $\Delta\chi$ [89].

The valence electron concentration (VEC) is defined by [72,89,92]:

$$VEC = \sum_{i=1}^{n} C_i (VEC)_i \tag{6}$$

where the VEC is the average valence electron concentration considering all elements and their respective concentrations. This term has proven to be useful in predicting the crystal structures of the phases that form. For example, alloys with VEC values greater than 8 have been found to stabilize FCC type phases, while alloys with VEC values below ~6.87 stabilize BCC structures [89,93]. Similarly, alloys with mid-range VECs are expected to form a combination of FCC and BCC type phases. In a similar regard, it is known that elements such as Co and Ni tend to stabilize FCC type phases and Al and Ti tend to stabilize BCC/B2 type phases.

The atomic size difference, δ, is defined by [72,89,97]:

$$\delta = \left[\sum_{i=1}^{n} C_i \left(1 - \frac{r_i}{\bar{r}}\right)^2 \right]^{1/2} \times 100 \tag{7}$$

where r_i is the radius of component i, and $\bar{r}$ is the average atomic radius relative to the alloy constituents and their respective atomic concentrations. It was first proposed that solid solution phases tend to stabilize when $\delta \leq 6.6$ %, but in some cases, $\delta \leq 4.6$ % is required [84,89,90,92,97]. With larger atomic size differences, severe lattice distortion occurs, which tends to stabilize intermetallic phases [72]. Guo et al. showed that δ is a critical rule in predicting the stability of solid solution type microstructures in HEAs [72,92].

Lastly, Yang et al. proposed the parameter, Ω, defined by [72,84,89]:

$$\Omega = \frac{T_m \Delta S_{mix}}{|\Delta H_{mix}|} \tag{8}$$

and

$$T_m = \sum_{i=1}^{n} C_i (T_m)_i \tag{9}$$

where T_m is the theoretical melting temperature based on the mixture rule. The Ω parameter combines the influences of enthalpy and entropy into one respective term. Yang and Zhang deduced that solid solution phases should form in alloys with $\Omega \geq 1.1$ and $\delta \leq 6.6\%$, but that intermetallic phases could still form when $4.6\% < \delta < 6.6\%$ [84,98,102]. It is important to note that the Ω parameter is a necessary, but insufficient condition for predicting solid solution formation, since it assumes a quasi-chemical arrangement, thus neglecting the mismatch due to variations in the atomic radii of constituent atoms [84].

2.5 High Entropy Superalloys

Recently, Wang et al. examined the previously defined HEA phase formation rules relative to commercial superalloys [103]. The analysis focused enthalpy of mixing, atomic size difference, and VECs. All the superalloys investigated exhibited VECs in excess of 7.8, which should ultimately stabilize FCC phases. It was discovered that solid-solution strengthened superalloys were in the range of ($0\ \mathrm{kJ/mol} \geq \Delta H_{mix} \geq -7\ \mathrm{kJ/mol}$) and ($2\% \leq \delta \leq 6\%$), while the precipitation strengthened superalloys were in the range of ($3\ \mathrm{kJ/mol} \geq \Delta H_{mix} \geq -18\ \mathrm{kJ/mol}$) and ($3\% \leq \delta \leq 8\%$) [103]. These ranges are shown plotted in Fig. 2-2 with the enthalpy and delta values from the alloy examined in this thesis. Wang et al. concluded that HEAs for structural applications should mimic the findings based on superalloys [103]. In other words, structural HEAs should have minor enthalpy of mixing and atomic size difference terms with relatively high VECs [103]. $Al_{10}Co_{25}Cr_8Fe_{15}Ni_{36}Ti_6$ CCA being investigated in this study exhibits a multi-phase microstructure.

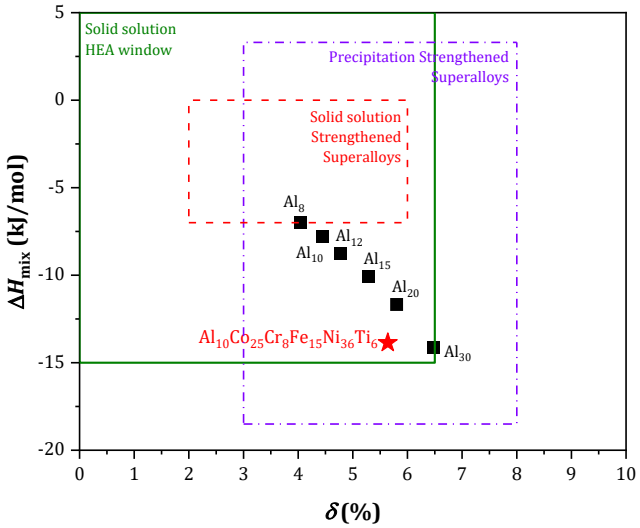

Figure 2-2. A plot of δ versus ΔH_{mix} for the alloy investigated in this study along with the ranges for commercial solid-solution strengthened and precipitation-strengthened superalloys. Included are the alloys investigated by Butler in his study of AlNiCoCrFe based HEAs [104]. Figure adapted from reference [103].

2.6 HEA Composition Optimization

A survey of published literature shows that most of the work on HEAs has involved study of bulk alloys containing Al, Co, Cr, Fe, and Ni as primary constituents [5-7,10,11]. A lot of work has gone into the optimization of HEA compositions. With the compositional flexibility provided by HEAs mechanical and chemical properties can be fine-tuned to meet specific needs. Some recent reviews of typical microstructures, properties, and potential applications for HEAs and CCAs can be found in references [5-8,93,97].

Manzoni and colleges have performed extensive studies on the emerging Al-Co-Cr-Cu-Fe-Ni-Ti family of HEAs and compared the most promising compositions: equiatomic AlCoCrCuFeNi and equiatomic AlCoCrFeNi along with $Al_{23}Co_{15}Cr_{23}Cu_8Fe_{15}Ni_6$, $Al_8Co_{17}Cr_{17}Cu_8Fe_{17}Ni_{33}$, $Al_8Co_{17}Cr_{14}Cu_8Fe_{17}Ni_{34.8}Mo_{0.1}T_1W_{0.1}$ and $Al_{10}Co_{25}Cr_8Fe_{15}Ni_{36}Ti_6$ [10,44,100,105-111]. These compositions were selected from an exhaustive ThermoCalc™

search of nearly 200 chemistries within this HEA family. After optimum heat treatment the microstructures and mechanical properties were compared between the six compositions. Manzoni et al. determined that $Al_{10}Co_{25}Cr_8Fe_{15}Ni_{36}Ti_6$ was the most optimized of the tested HEAs, exhibiting medium hardness with good ductility and excellent tensile strength [43]. Cu was found to be a strong segregating element resulting in poor microstructure, resulting in its complete removal from the final composition. Mechanically, this novel HEA tends to outperform other FCC solid solution forming commercial alloys like IN617 and Alloy 800H. The mechanical properties of $Al_{10}Co_{25}Cr_8Fe_{15}Ni_{36}Ti_6$ can be tuned even further [11,47]. It's been shown that small additions of Hf and Zr can significantly raise ultimate tensile strength. It is worth noting that several other research groups have also published information regarding additional high entropy superalloys based on the Al-Co-Cr-Fe-Ni-Ti system that show Ni-based superalloy like microstructures (a brief listing can be found in references [10,42,73,112-118]).

A large focus of HEA development has been focused on the cultivation of a multiphase microstructure, like modern Ni-based superalloys. Miracle and Senkov's review of 648 unique HEA chemistries found 435 instances of multiphase microstructures. Microstructurally, $Al_{10}Co_{25}Cr_8Fe_{15}Ni_{36}Ti_6$ features a two-phase matrix consisting of disordered FCC (γ) and ordered FCC or $L1_2$ (γ') phases with a tertiary ordered BCC, NiAl type B2, precipitate phase at elevated temperatures [10-12,48]. The crystal structure of bulk $Al_{10}Co_{25}Cr_8Fe_{15}Ni_{36}Ti_6$ was investigated by Butler et al., summarized in Fig. 2-3 [47]. Despite the alloy matrix being comprised of two phases, it has been extremely difficult to distinguish γ/γ' peaks due to similar lattice parameters and strong preferred orientations. In one of their studies Manzoni et al. observed the FCC and $L1_2$ lattice parameters to be within 0.002 nm of each other [12].

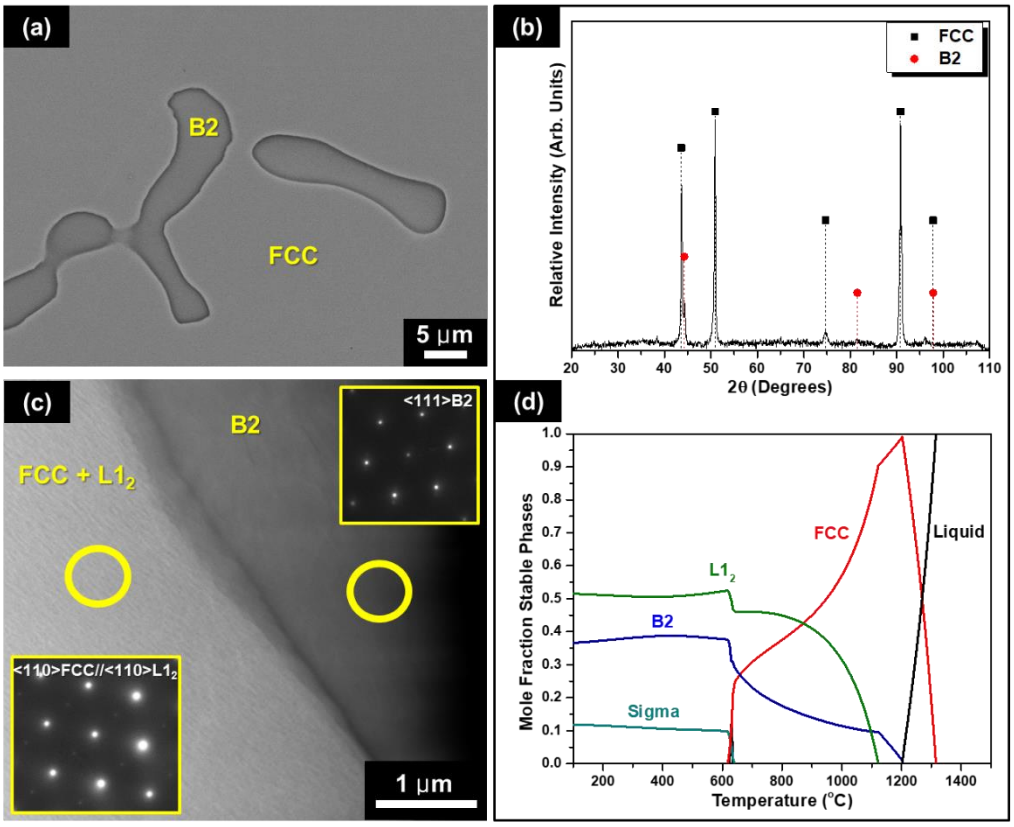

Figure 2-3: As-cast $Al_{10}Co_{25}Cr_8Fe_{15}Ni_{36}Ti_6$ adapted from Butler et al. [46]. Micrographs of phases, (a) and (c); XRD pattern (b); and ThermoCalc phase prediction (d).

2.7 HEA Coatings

Until recently there have been very few investigations of thick HEA coatings. Most researchers have focused on coatings or thin films with thickness less than ~2 µm. In addition, the majority of this work has focused on the growth of high-entropy nitride, oxide, and carbide films rather than metals [15,26,34,40,119].

A valuable resource for researching coatings above the nanoscale deposited via sputtering are the seminal papers by John Thornton [120,121]. Thornton researched thick film growth using physical vapor deposition processes. He presented a structure zone model (SZM) that predicted coating morphology based on substrate homologous temperature and argon working pressure, seen in Fig. 2-4. Zone 1 structures are grown at low temperatures and med to high working

pressures. At these conditions the temperature is too low for diffusion causing rough grains with voids. Any surface roughness on the substrate is exaggerated on the coating surface. At higher temperatures the structure evolves into Zone T. Zone T morphologies typically grow on smooth, homogeneous substrates which accommodates the growth of densely packed fibrous grains. Zone T structures are also characterized by high dislocations density, giving the coating high hardness and strength with minimal ductility. Zone 2 structures are formed at homologous temperatures high enough for surface diffusion-controlled growth. This allows the formation of dense columnar grains of larger size. Zone 3 structures form starting at homologous temperatures around 0.8. At this temperature the coating can recrystallize during the deposition process. Due to the Hall-Petch relationship, Thornton notes that the larger grain sizes of Zone 2 and 3 morphologies leads to decreased strength and hardness [25]. Thornton's structure zone model serves as a baseline for predicting coating structure. The working pressure and temperature zone boundaries for complex alloys differ from those for pure metals. This study aims to provide insight into the effects of deposition parameters on the growth of $Al_{10}Co_{25}Cr_8Fe_{15}Ni_{36}Ti_6$ coatings.

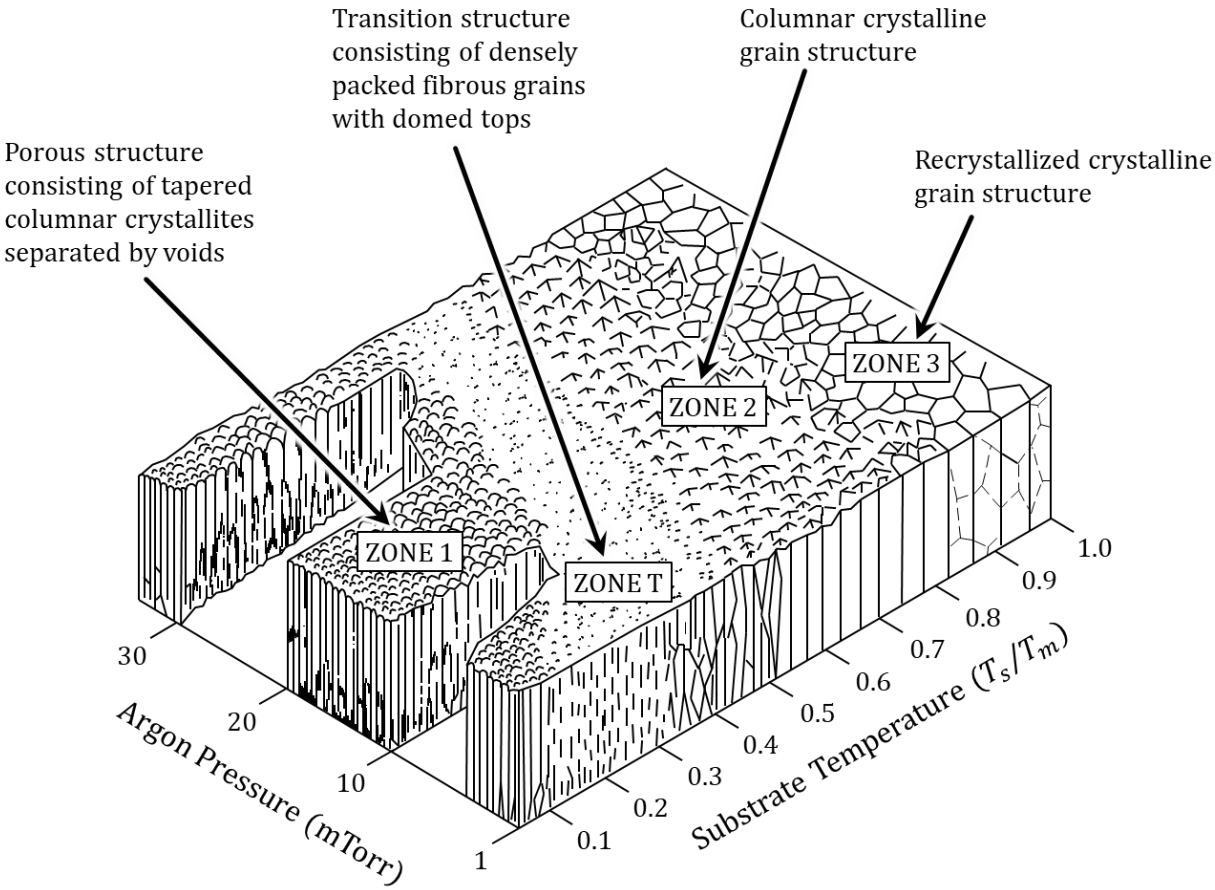

Figure 2-4: Structure zone model for predicting coating morphology. This figure was adapted from Thornton [25].

CHAPTER 3: EXPERIMENTAL PROCEDURES

3.1 Sputtering Target and Substrate Preparation

The bulk alloy targets of $Al_{10}Co_{25}Cr_8Fe_{15}Ni_{36}Ti_6$ were produced via vacuum arc melting in a Ti-gettered argon atmosphere on a water-cooled Cu hearth. These bulk alloy samples were melted several times to ensure homogeneity. All elemental components used to fabricate the bulk HEA had purities of 99.9% or higher. The resulting cast ingots were then machined to 50.5 mm diameter by 6.3 mm thickness.

Single crystal Ni-based superalloy substrates, CMSX-8, which were ground to a 1200 grit surface finish were used as substrates. Substrate dimensions of 15.9 mm × 9.5 mm × 3.3 mm were used in this thesis. After grinding the substrates were ultrasonically cleaned in sequential acetone, methanol, ethanol, and isopropanol baths. The compositions for the bulk $Al_{10}Co_{25}Cr_8Fe_{15}Ni_{36}Ti_6$ targets and substrates are listed in Table 3.1.

For each coating deposition series, four substrates were placed radially from the center of the heating stage, as shown in Fig. 3.1. This was done because there was a visible temperature gradient on the substrate plate, which was composed of Inconel 625 [122]. The substrate plate is heated by two USHIO 240V-1000W halogen bulbs located under the center of the plate. The circular substrate plate radius measures 84.5 mm (i.e., 3.325 in) in diameter with the edge sample (position 4) being approximately 76.2 mm (i.e., 3 in) from the center, directly under the target. Positions 3 and 2 were approximately 50.8 mm and 25.4 mm respectively from the center (position 1). The target to sample sputtering distance (i.e., throw distance) was set to

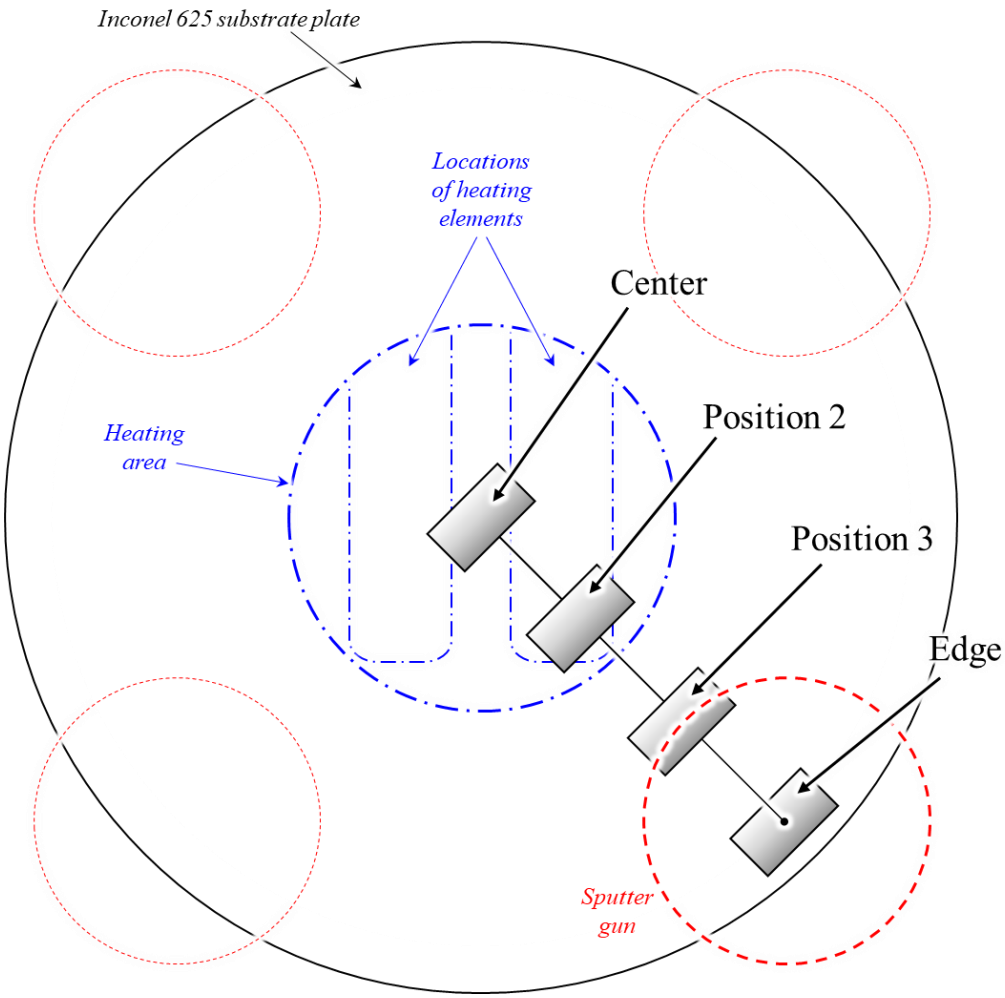

Figure 3-1: Positioning of samples on substrate plate. The heavy blue dash-dot-dash lines indicate the relative locations of the heating area and heating elements beneath the stage. The red dotted outlines denote the relative location of the sputter gun relative to the substrates. One gun was used for each deposition series.

Table 3-1: Composition of $Al_{10}Co_{25}Cr_8Fe_{15}Ni_{36}Ti_6$ sputtering targets and CMSX-8 substrates.

$Al_{10}Co_{25}Cr_8Fe_{15}Ni_{36}Ti_6$ Sputtering Targets			CMSX-8		
	At. %	Wt. %		At. %	Wt. %
Ni	35.1	38.3	Ni	62.88	59.9
Co	24.9	27.3	Co	10.45	10
Al	10.5	5.2	Al	13.02	5.7
Cr	8.4	8.1	Cr	6.40	5.4
Ti	6.2	5.5	Ti	0.90	0.7
Fe	15	15.6	Ta	2.72	8
			W	2.68	8
			Re	0.49	1.5
			Mo	0.39	0.6
			Hf	0.07	0.2

approximately 38.1 mm (i.e., 1.5 in), the minimum distance achievable in the sputtering system used. No stage rotation was applied during deposition.

3.2 Coating Deposition

Unbalanced direct current (DC) magnetron sputtering was used to deposit the $Al_{10}Co_{25}Cr_8Fe_{15}Ni_{36}Ti_6$ CCA. This condition was selected because it yields a higher deposition rate and produces a denser microstructure. Coatings were applied using and AJA International, Inc. ORION 4 sputtering system with downward facing targets. After loading the chamber was pumped back down to an internal pressure of at least 5.0×10^{-5} Pa. Once a low enough initial pressure was achieved, the heating stage was turned on and slowly ramped to 650 °C, the selected deposition temperature. The chamber was then soaked at temperature until the vacuum recovered to at least 5×10^{-3} Pa or better. The substrates were RF biased at 25V for 5-10 minutes before deposition began while the target was being brought up to designated power. Ultra-high purity argon was pumped into the chamber at various rates to achieve the desired working pressure for each deposition.

The working conditions for the various depositions, designated as Series 1-3 in this thesis, are listed in Tables 3.2-4. For Series 1, a 30-minute deposition was done using four different conditions: variations of 225 and 300 W powers at 5 or 30 mTorr argon pressure. Series 2 samples consist of 1.5-hour depositions at 300 W target power. These coatings were grown at 5, 15, and 30 mTorr argon pressure. Half of the samples were then marked for annealing. The final set of samples, Series 3, were made with a 3-hour deposition done at 5 mTorr working pressure and then annealed.

Table 3-2: Deposition series 1 - 30-minute deposition working conditions. All samples in this series were analyzed as deposited.

Parameters / Heat Treatment	225 Watts		300 Watts	
	5 mTorr	30 mTorr	5 mTorr	30 mTorr
As Deposited	Center	Center	Center	Center
	Position 2	Position 2	Position 2	Position 2
	Position 3	Position 3	Position 3	Position 3
	Edge	Edge	Edge	Edge

Table 3-3: Deposition Series 2 – 1.5-hour deposition working conditions and heat treatments.

Parameters / Heat Treatment	300 Watts		
	5 mTorr	15 mTorr	30 mTorr
As Deposited	Center	Center	Center
	Position 2	Position 2	Position 2
	Position 3	Position 3	Position 3
	Edge	Edge	Edge
Annealed	Center	Center	Center
	Position 2	Position 2	Position 2
	Position 3	Position 3	Position 3
	Edge	Edge	Edge

Table 3-4: Deposition series 3 – 3-hour deposition working conditions and heat treatments.

Parameters / Heat Treatment	300 Watts
	5 mTorr
Annealed	Center
	Position 2
	Position 3
	Edge

3.3 Heat Treatment

Samples designated for heat treatment were annealed in a tube furnace at 1000 °C. Ultra-high purity argon was pumped through the furnace to minimize the chances for oxidation. After an hour of heating the samples were removed from the furnace and air cooled to room temperature.

3.4 Structural Analysis

X-ray diffraction (XRD) was conducted on coated surfaces of the as-deposited samples from Series 2 and the annealed samples from Series 3 to determine the predominant phases present. After XRD analysis, samples were mounted and polished to a 0.05 μm surface finish for scanning electron microscopy (SEM). All SEM work was done with a Thermo Fisher Scientific Apreo™ 2 SEM in the secondary electron and backscattered electron modes. The resulting images were used to evaluate the quality, structure, and thickness of the coatings. Energy dispersive X-ray spectroscopy (EDS) was used to verify the chemistries of the sputtering targets and superalloy substrates, and to determine the chemistries of the coatings and any phases that formed within them. EDS was also used to create composition gradient charts for Series 2 and 3 samples. The resulting composition gradient charts were used to assess the extent of

interdiffusion between the coatings and substrates in the form of an interdiffusion zone (IDZ) size.

CHAPTER 4: RESULTS AND DISCUSSION

4.1 Heating Stage Temperature Gradient

When the heating stage was brought up to high temperatures, a visible temperature gradient could be seen with the center of the substrate plate being hotter than the edge (Fig. 4-1). Substrate temperature has a major effect on the morphology of the coating. Therefore, calculations were performed to estimate the temperature at different positions on the plate. The full calculation can be found in Appendix A. Inconel 625, the material that the substrate plate is made from, has a thermal conductivity of 19 W/m·°C at 649 °C [25]. Using the inverse-square law and the wattage of the USHIO bulbs, the amount of heat power applied to the plate was calculated to be approximately 678 W. Using the equation:

$$q = \frac{k}{s} A(T_{center} - T_{edge}) \tag{4-1}$$

where q is heat transfer, k is thermal conductivity, s is the distance from the heating area to the edge, A is the heating area of contact, and T represents the temperatures at the edge and center of the plate. Using this relationship and given a 650 °C center temperature, the temperatures of the Position 3 and Edge samples were estimated to be 545 and 350 °C respectively.

To qualitatively assess the accuracy of these calculations, temperature stickers were applied to the surface of the substrate plate. The stickers, which were capable of maximum temperature of 260 °C, changed color at all positions confirming that the edge temperature of the plate was at least above 260 °C. As substrate temperature has a profound impact on coating morphology, the temperature gradient was experimentally assessed by placing a type-K thermocouple beneath a representative superalloy substrate which was placed at the selected

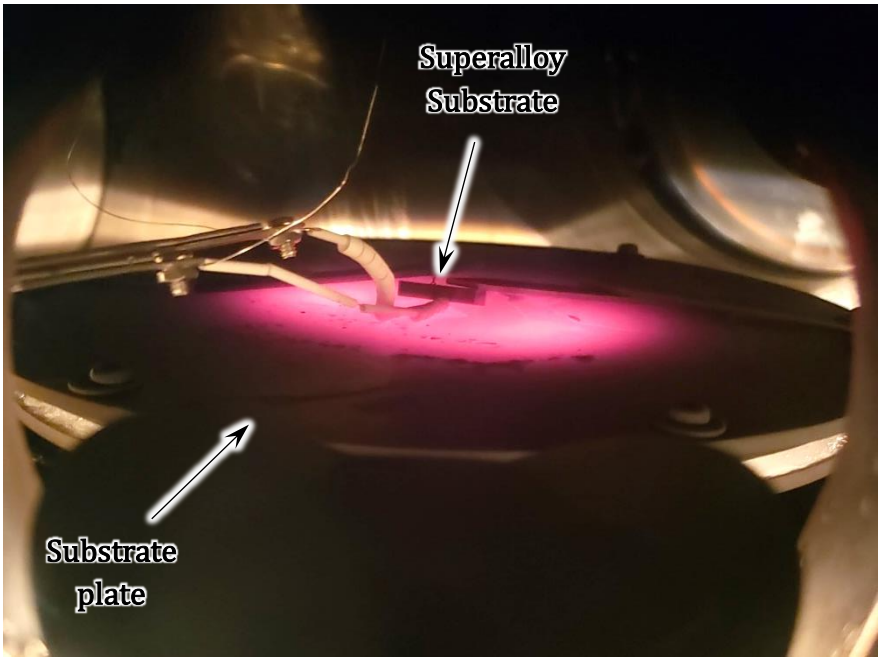

Figure 4-1: A picture of the substrate plate showing the temperature gradient. In this image the temperature was set at 650°C. This image also shows the thermocouple beneath a substrate located in the center of the substrate plate.

deposition positions on the substrate plate. The temperature was then raised sequentially from room temperature up to 650°C with isothermal holds of one hour or more to achieve a near steady state. The heating stage temperature is measured by a thermocouple that is located approximately 1 mm below the bottom of the substrate plate. That temperature and substrate temperatures were then recorded. The results are included in Fig. 4-2.

As expected, the temperatures decreased as the distance from the center of the plate increased. Two observations were unexpected. First, the temperature on top of the substrate lagged the setpoint by almost 100°C at 650°C. Second, the temperatures recorded at positions 2 and 3 on the substrate plate were lower than the temperature measured at the edge. The temperature lag at the plate center can be attributed to the location of the system control thermo-

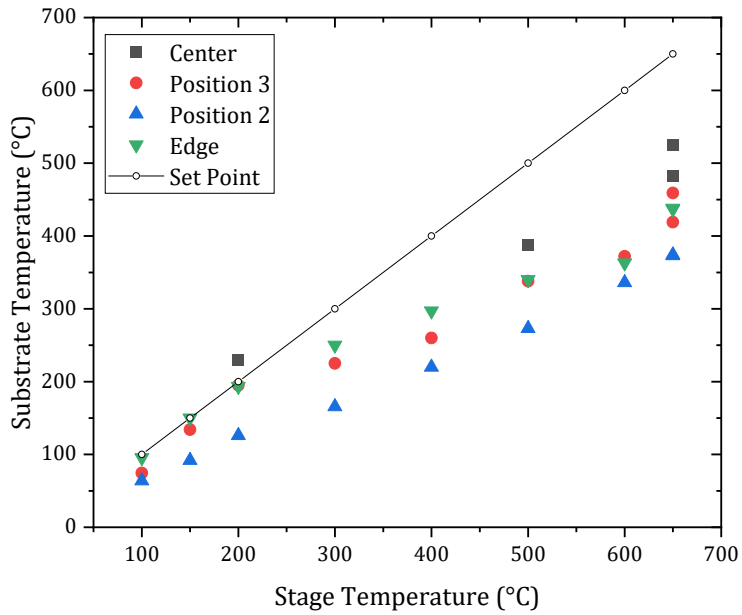

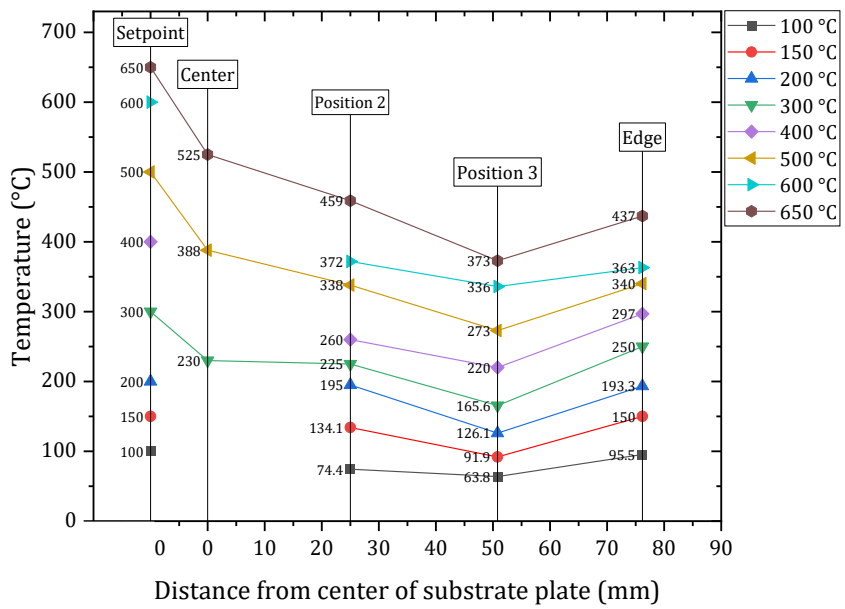

Figure 4-2: Temperature distributions across the substrate plate. (a) Plot of measured stage and substrate temperatures versus the temperature setpoint. (b) alternate plot showing the temperature profile across the substrate plate.

couple relative to the heating elements and to location of the measurement thermocouple which is on top of the substrate plate.

As for the temperature lag at positions 2 and 3; the reason is directly related to the design of the substrate plate and the fact that no rotation was used during deposition. The bottom side of the substrate plate has a series of concentric rings welded to the bottom to provide stiffening and to act as fins to distribute heat more uniformly provided that the stage is rotating. No stage rotation was used in this study. This resulted in two visible hot spots on the substrate plate, just above the underlying heating elements. Furthermore, the stiffening rings encompass the region between positions 2 and 3 on the substrate plate. It is hypothesized these fins acted more as a heat sink when the stage was not rotated resulting in a slightly reduced temperature in those regions.

4.2 Series 1 Coatings – Initial Screening

Series 1 depositions were completed to rapidly assess the influences of power level and working gas pressure on film/coating morphology. Due to the presence of the temperature gradient, this series of tests also allowed for a qualitative assessment of the influence of substrate temperature. The thicknesses and temperatures for the Series 1 deposits are shown in Table 4.1. As expected, the coatings formed at lower pressure are thicker than the coatings formed at higher pressure. Coatings located closer to the center of the substrate plate, farther away from the sputter gun, were also thinner. Looking at samples with matching pressure and temperature parameters at the different powers, the 300 W depositions were at least 50% thicker with some coatings upwards of 70% thicker for each condition compared to the 225 W deposits.

Table 4-1: Thickness measurements for Series 1 depositions.

Target Power	Working Pressure	Position	Substrate Temperature (°C) Calculated/Actual	Homologous Temperature	Thickness (µm)
225 W	5 mTorr	Center	650 / 525	0.517	0.5559
		Position 2	650 / 459	0.474	0.9909
		Position 3	545 / 373	0.419	1.0393
		Edge	350 / 437	0.460	1.3353
	30 mTorr	Center	650 / 525	0.517	0.3527
		Position 2	650 / 459	0.474	0.7778
		Position 3	545 / 373	0.419	1.1643
		Edge	350 / 437	0.460	1.1353
300 W	5 mTorr	Center	650 / 525	0.517	0.9274
		Position 2	650 / 459	0.474	1.4864
		Position 3	545 / 373	0.419	1.9355
		Edge	350 / 437	0.460	2.0564
	30 mTorr	Center	650 / 525	0.517	0.6039
		Position 2	650 / 459	0.474	1.1722
		Position 3	545 / 373	0.419	1.7583
		Edge	350 / 437	0.460	1.7462

Fig. 4.3 shows representative images of the different morphologies observed in this series of depositions. Homologous temperatures were determined based upon the solidus temperature

of 1270°C reported by Manzoni et al. [123]. Fig. 4-3(a) shows the center sample deposited at 30 mTorr. With a homologous temperature of 0.517, a Zone 2 morphology was expected based on the SZM. However, the porous structure observed in the cross section and topography is reminiscent of a Zone 1 morphology but with wider columns. A review of published literature suggests that this high porosity is a product of the high incident angle of sputtering [124-126]. This phenomenon is explored further in the thicker coatings of Series 2. Mukherjee and Gall have demonstrated that typical Zone 2 morphologies are suppressed by increased angles of incidence during sputtering due to shadowing effects leading in the most extreme cases to the formation of structures consisting of rods, columns and protrusions separated by voids or at the highest temperatures to equiaxed grains with whiskers [126].

All the coatings produced at 5 mTorr, represented by Fig. 4-3(b), exhibit the smooth featureless morphology typical of Zone T coatings. Fig. 4-3 (c) and (d) show coatings produced at the same working conditions at different target powers. These coatings show an intermediate hybrid between the Zone T and Zone 2 structure with dense distinctive fibrous grains with no voids. No major morphological differences were observed between coatings produced at different powers with the same pressure and temperature parameters.

4.3 Series 2 Coatings – As Deposited

An additional working pressure condition at 15 mTorr was added for the Series 2 depositions. A 1.5 hr deposition time and 300 W target power were used to produce thicker coatings, as seen in Table 4-2. Appendix B contains images and concentration profiles from the as-deposited coatings indicating no interdiffusion between the coatings and substrates during deposition. The Series 2 as-deposited coatings show similar trends to the trial depositions (i.e., Series 1). The coatings grown at 5 mTorr all display the featureless cross section and smooth

surface topology typical of Zone T with the 30 mTorr coatings exhibiting more porous and columnar structures.

Fig. 4-4 displays representative topographic and cross-sectional images of the Series 2 as-deposited coatings. Fig. 4-4 (a) gives a better image of the of the porous Zone 2 coatings than was observed in the high-pressure center stage samples of Series 1. As was noted in section 4.2, the porosity is a result of shadowing caused by the angular growth of the coating columns. The tips of the columns display the faceted tops that are indicative of a Zone 2 morphology. This topography is seen again in the (b) and (c) images and matches the model developed by Mukherjee and Gall [126]. All the 5 mTorr coatings, represented in (d), continue to display smooth Zone T morphologies.

Fig. 4-5 shows the observed SZM of the coatings studied in this thesis. Shadowing caused by a high angle between the target and substrate resulted in the occurrence of porous Zone 2 morphologies for coatings deposited on in the center position and in position 2 on the substrate plate at higher working pressures.

The thicker coatings allowed for XRD phase confirmation. Fig. 4-6 – Fig. 4-8 shows XRD patterns for the as-deposited coatings. On the thinner coatings some peaks from the CMSX-8 substrate were registered. Peaks were identified for the expected FCC and BCC/B2 phases. The lattice parameters for the FCC matrix and BCC phases were determined to be 3.592 and 2.869 Å respectively. This result concurs with previously determined lattice parameters [46]. A set of three peaks near 40 °2θ were detected on each scan. After conducting additional scans these peaks were found to come from the aluminum alloy sample holder.

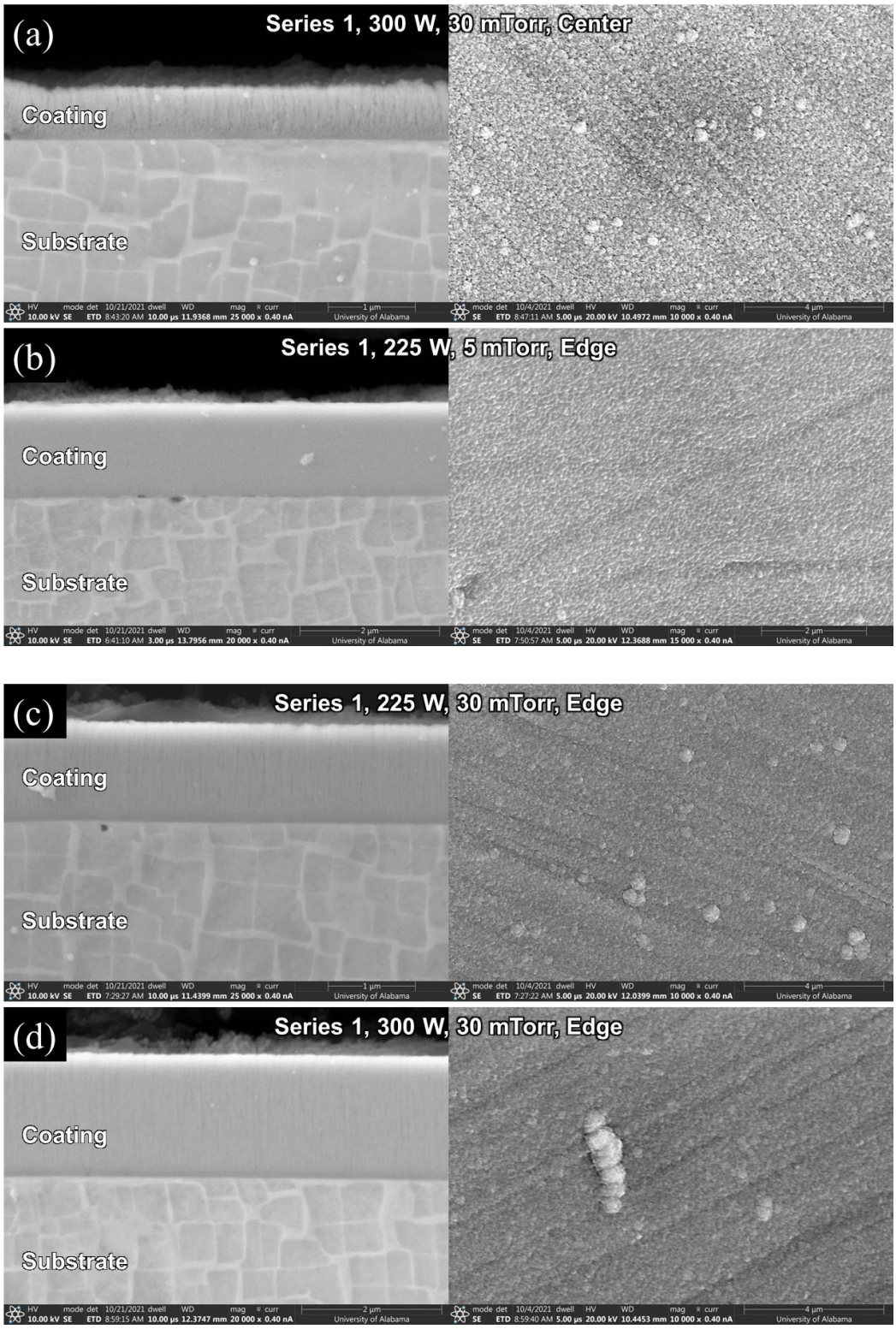

Figure 4-3: Representative cross section and topography images of some as-deposited Series 1 coatings. (a) 300 W, 30 mTorr Center (b) 225 W, 5 mTorr Edge (c) 225 W, 30 mTorr Edge and (d) 300 W, 30 mTorr Edge.

Table 4-2: Thickness measurements of as deposited Series 2 coatings.

Target Power	Working Pressure	Position	Substrate Temperature (°C) Calculated/Actual	Homologous Temperature	Thickness (µm)
300 W	5 mTorr	Center	650 / 525	0.517	2.4639
		Position 2	650 / 459	0.474	4.4925
		Position 3	545 / 373	0.419	5.6988
		Edge	350 / 437	0.460	5.9518
	15 mTorr	Center	650 / 525	0.517	1.7108
		Position 2	650 / 459	0.474	3.3378
		Position 3	545 / 373	0.419	4.8442
		Edge	350 / 437	0.460	5.3166
	30 mTorr	Center	650 / 525	0.517	1.1884
		Position 2	650 / 459	0.474	2.4925
		Position 3	545 / 373	0.419	3.8768
		Edge	350 / 437	0.460	4.6052

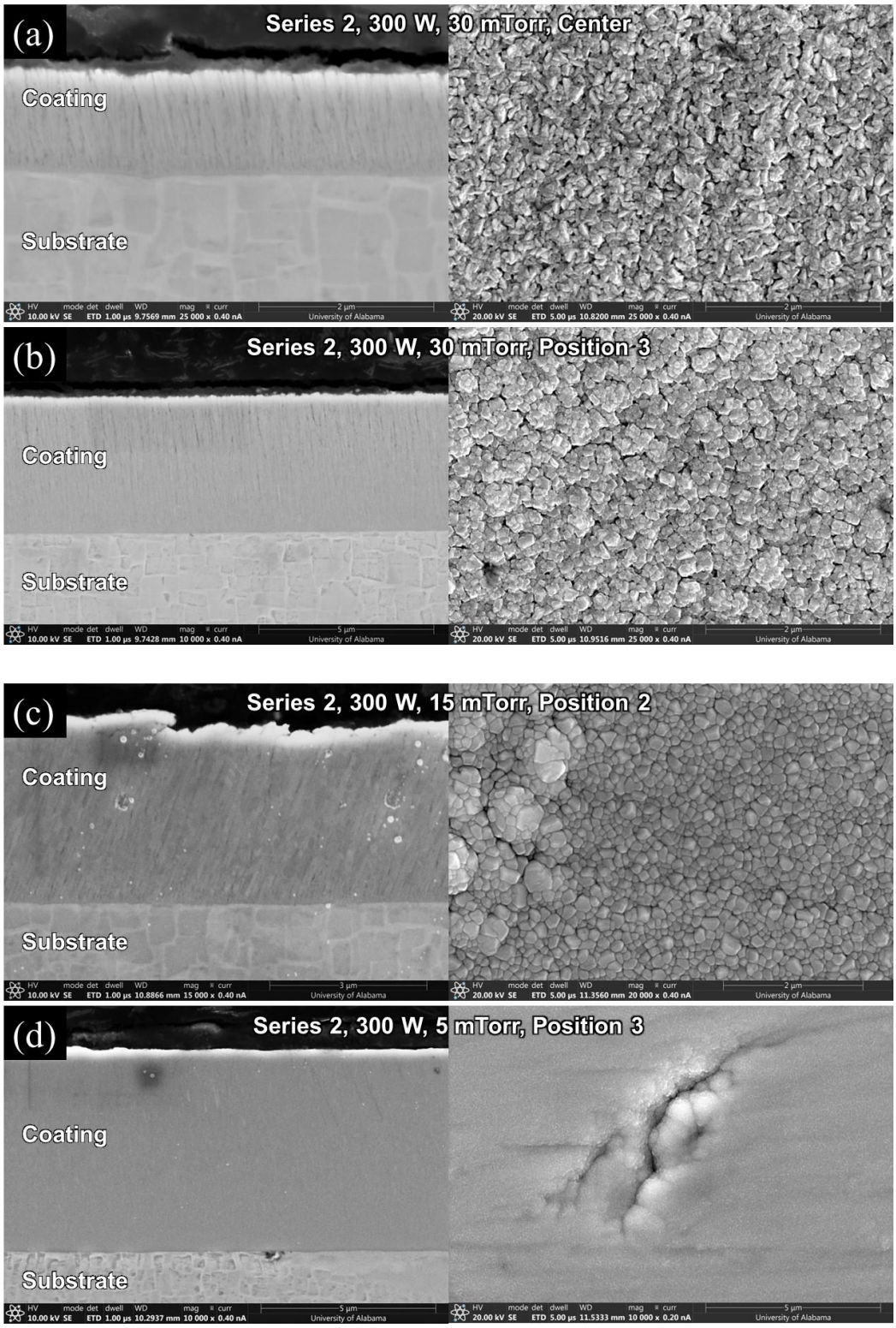

Figure 4-4: Representative cross section and topography images of as-deposited Series 2 coatings. (a) 30 mTorr Center (b) 30 mTorr Position 3 (c) 15 mTorr Position 2 and (d) 5 mTorr Position 3

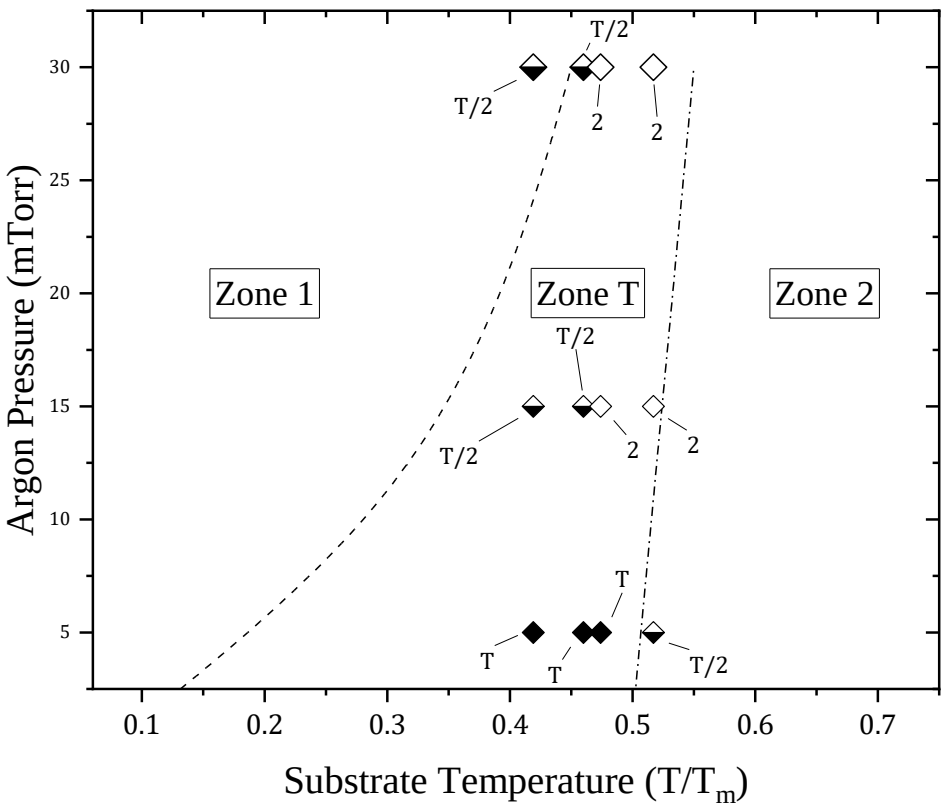

Figure 4-5: Structure zone model determined for the Series 2 $Al_{10}Co_{25}Cr_8Fe_{15}Ni_{36}Ti_6$ coatings deposited in this study. Coating conditions were 300 W at T = 650 °C. The approximate boundaries between coating regimes, as defined by Thornton [25], are schematically represented with dotted lines.

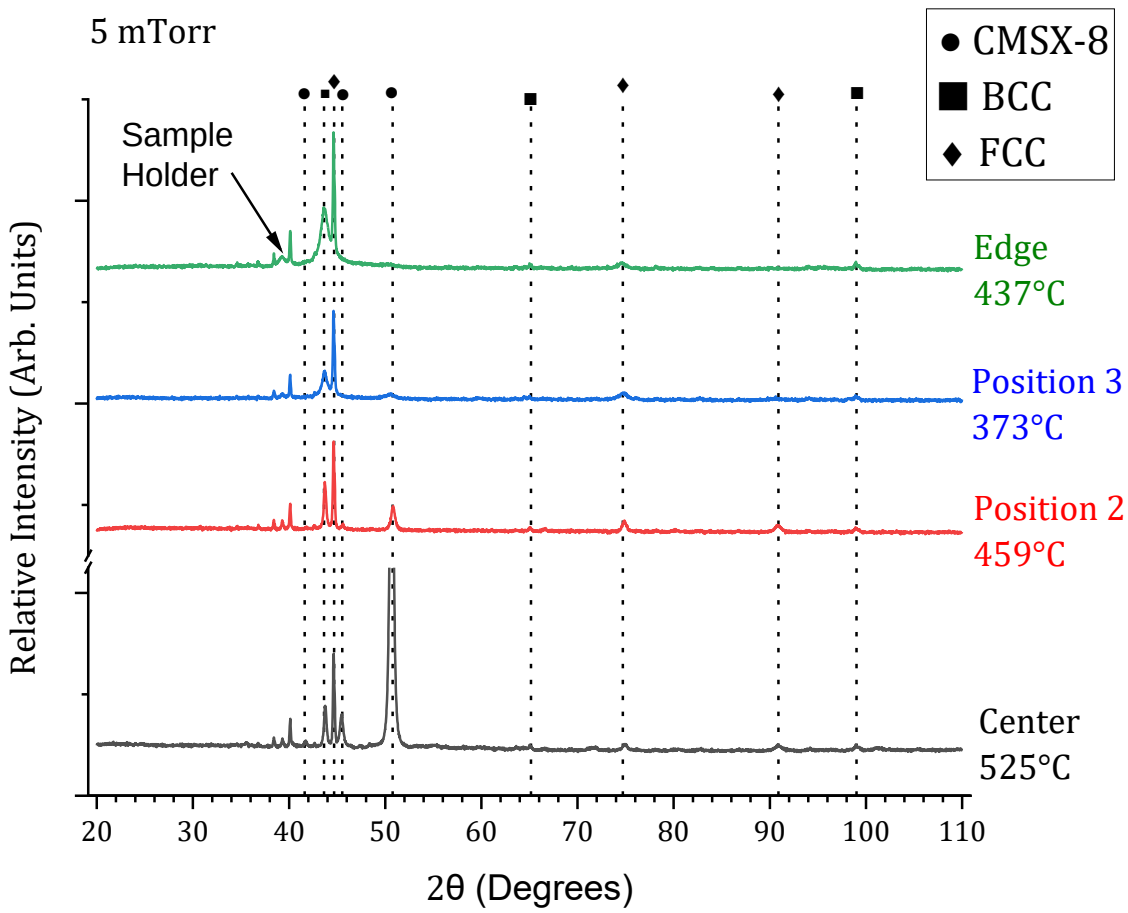

Figure 4-6: XRD patterns of as-deposited coatings produced at 5 mTorr working pressure.

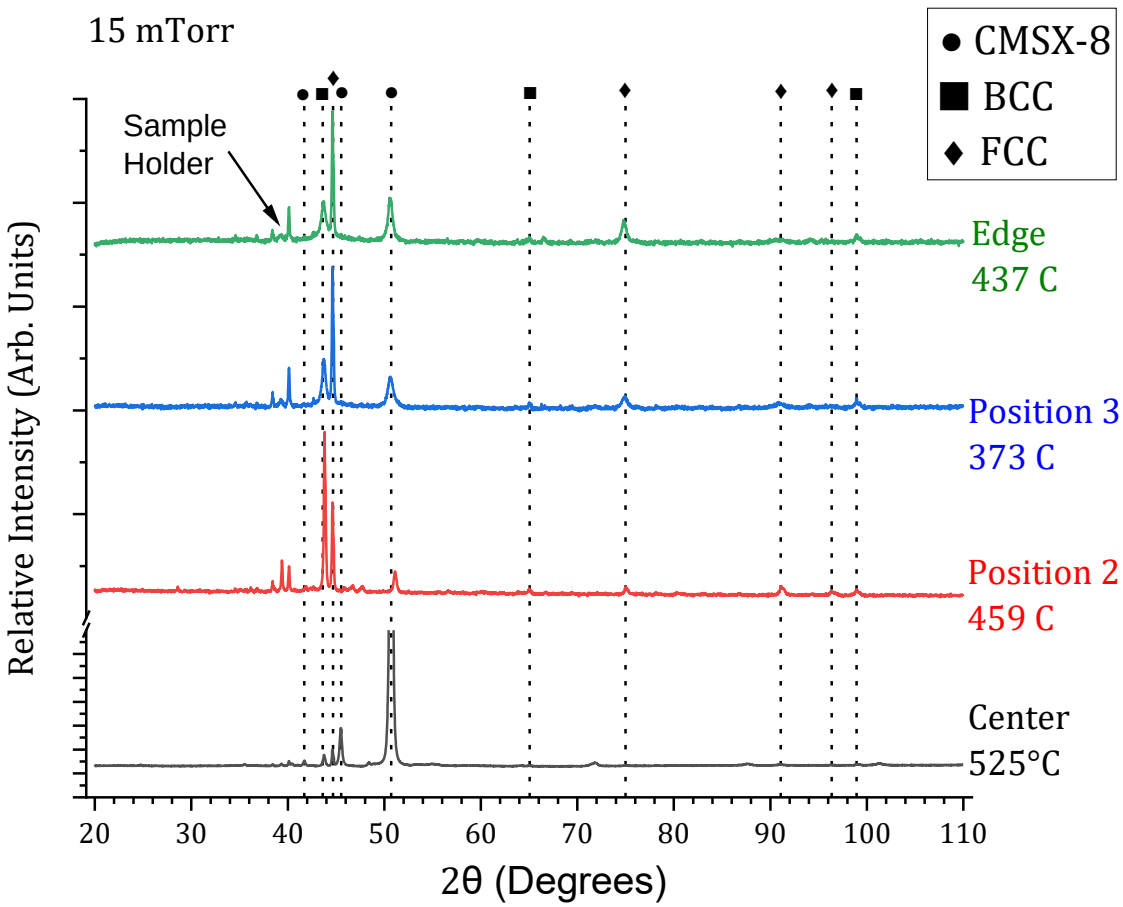

Figure 4-7: XRD patterns of as-deposited coatings produced at 15 mTorr working pressure.

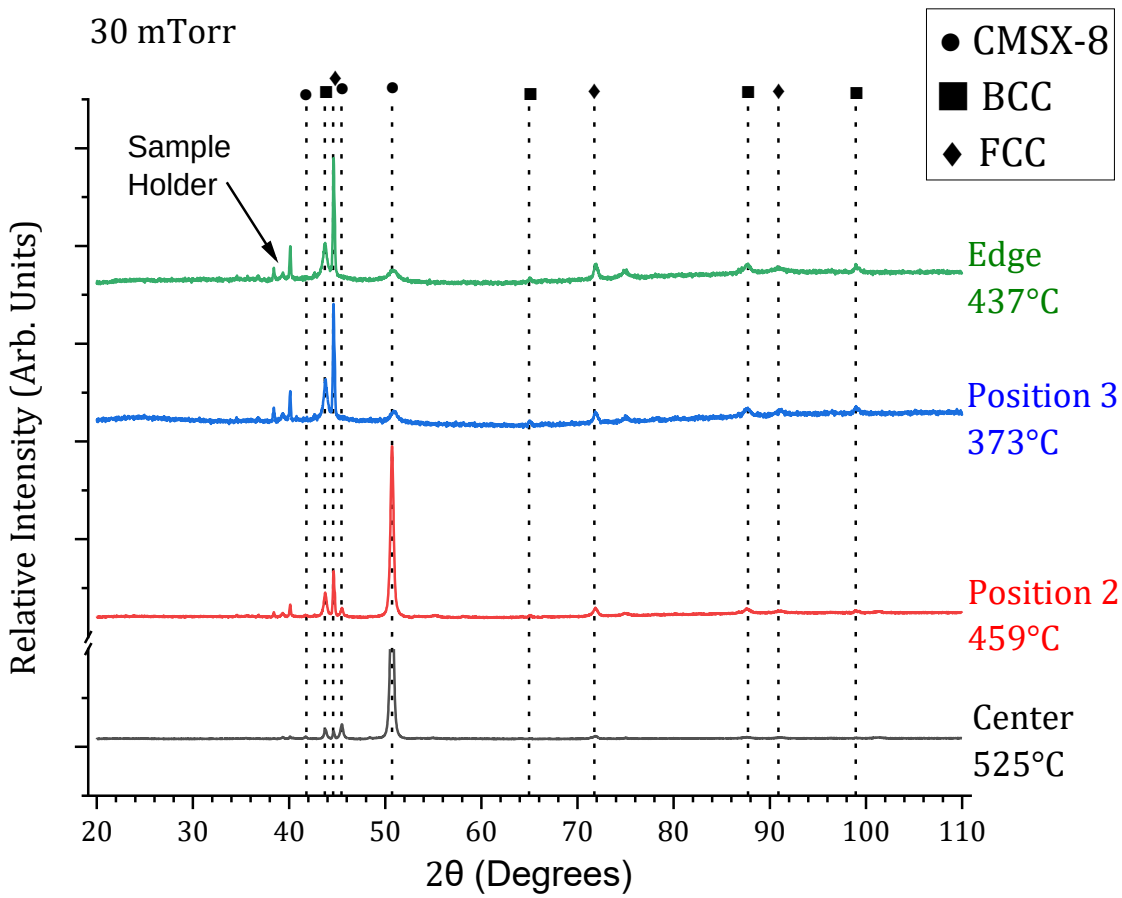

Figure 4-8: XRD patterns of as-deposited coatings produced at 30 mTorr working pressure.

4.4 Series 2 Coatings - Annealed

The Series 2 coatings were annealed to observe morphology changes and to preliminarily assess coating/substrate interdiffusion behavior. Table 4-3 gives the measured IDZ thickness. These measurements were determined by analyzing the composition profiles collected using EDS analysis. Fig. 4-9 shows representative photos of annealed cross sections with their corresponding composition profiles. The Zone T, 5 mTorr coatings displayed the smallest IDZs overall. The 30 mTorr center sample composition profile showed a relatively consistent composition through the cross section. Therefore, no IDZ could be measured for that coating. Each sample showed Al diffusing out of the coating and towards the surface. The Re, Mo, and Hf components of the CMSX-8 substrate were excluded from the composition profiles. Their respective atomic percentages in the superalloy are too low for accurate EDS measurements. The 5 mTorr coatings showed evidence of phase separation within the coating. This was further investigated in the Series 3 depositions.

4.5 Series 3 Coatings – Thicker Coatings After Annealing

The final series of depositions were all produced at 5 mTorr for 3 hours to obtain coatings with thickness that was more representative of commercial coatings and bulk materials. These deposition conditions also yielded the densest coatings which interdiffused the least during the Series 2 anneals.

The thickness and IDZ measurements of the coatings are displayed in Table 4-4. As seen in the 5 mTorr Series 2 coatings, some of the coatings showed evident phase separation resulting in the growth of BCC/B2 phases in an FCC matrix. Fig. 4-10 shows the cross sections and composition profiles of the Series 3 coatings. The position 3 sample (Fig. 4-10(c)) showed minor phase separation with the edge sample (Fig. 4-10(d)) exhibiting high levels of phase separation.

Table 4-3: IDZ measurements of annealed Series 2 coatings. Samples were annealed at 1000 °C for 1 hour.

Target Power	Working Pressure	Position	IDZ Thickness (µm)
300 W	5 mTorr	Center	0.4834
		Position 2	0.7246
		Position 3	0.9782
		Edge	0.9299
	15 mTorr	Center	0.753
		Position 2	1.2663
		Position 3	1.2563
		Edge	2.2289
	30 mTorr	Center	N/A
		Position 2	0.933
		Position 3	1.10552
		Edge	1.012

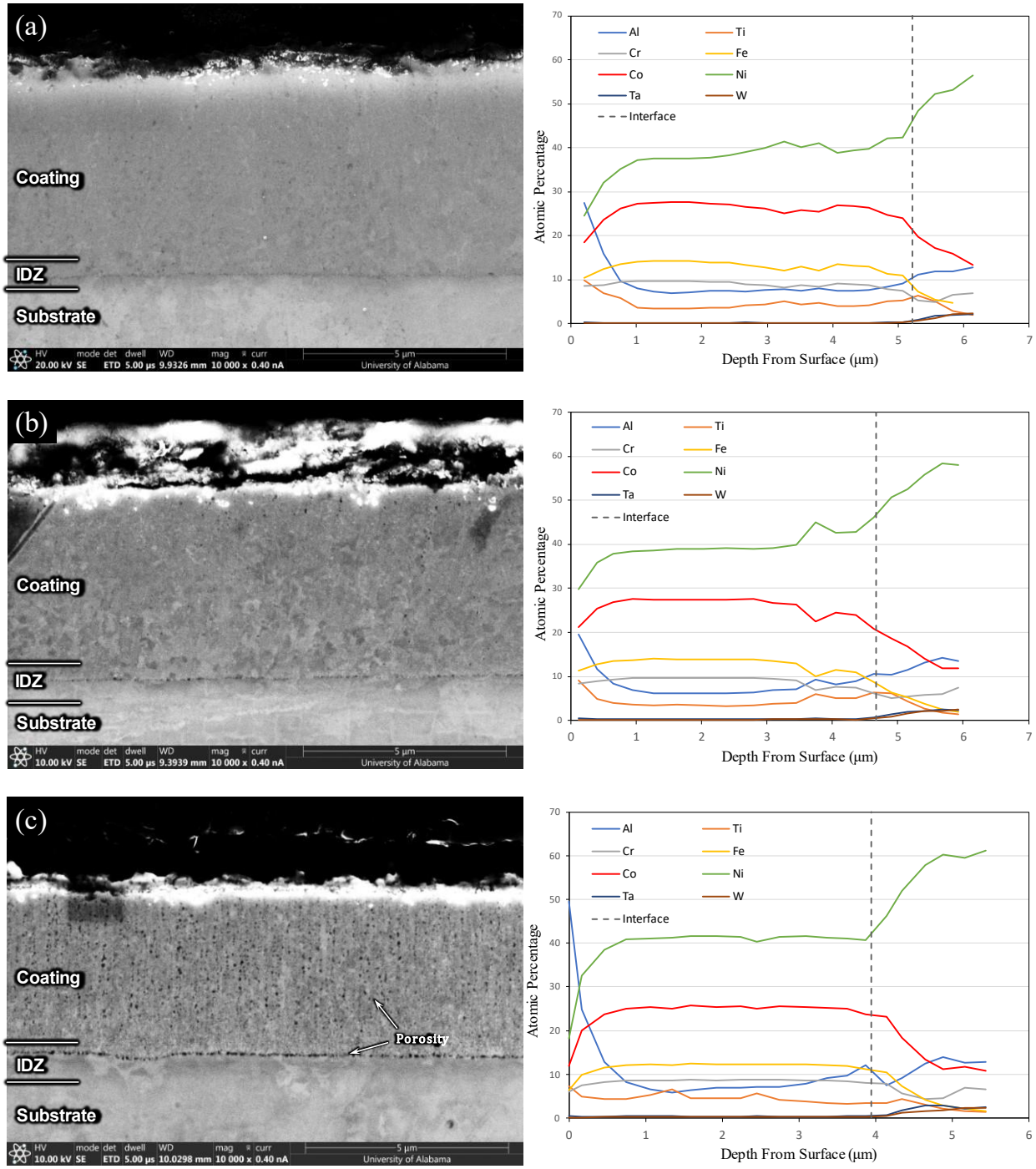

Figure 4-9: Representative cross section images and composition profiles for annealed Series 2 coatings. (a) 5 mTorr position 3 (b) 15 mTorr Edge and (c) 30 mTorr Edge. Complete composition profiles can be found in Appendix C.

The compositions of the separate phases were determined using EDS and are given in Table 4-5. The data for this analysis was collected from the edge sample because it showed the highest amount of distinct phase separation. The high standard deviations are most likely caused by the short heat treatment not allowing time for proper phase separation.

The coatings deposited at the lowest homologous temperatures (i.e., 0.419 at Position 3, 0.46 at edge, and 0.474 at Position 2) all exhibited Zone T morphologies while the one deposited at the highest temperature (center position) exhibited mixed Zone T/2 morphology. Surprisingly, the coating deposited at the highest temperature, which was the thinnest, exhibited the least amount of interdiffusion. This can be attributed to the fact that those coatings, because they are nearer Zone 2, are denser, and exhibit larger columnar features and fewer grain boundaries. It is well known that grain boundary diffusion is significantly faster than bulk diffusion [127]. Though more quantitative microscopy is warranted, this observation suggests that thinner coatings with the appropriate morphology can provide better resistance to interdiffusion than thicker ones if they possess the right morphology.

The XRD patterns of the annealed Series 3 coatings are shown in Fig. 4-11. The same FCC and BCC/B2 peaks observed in the Series 2 coatings were observed here along with several small oxide peaks that formed on the surface during air cooling. The oxide peaks positions most closely matched known values for α-Al_2O_3 and nickel chromate spinel ($NiCr_2O_4$) [128,129]. Three small peaks associated with the XRD sample holder were identified near 40 ° 2θ.

Table 4-4: Thickness and IDZ measurements of Series 3 coatings. Samples were annealed at 1000 °C for 1 hour.

Power	Working Pressure	Position	Coating Thickness (µm)	IDZ Thickness (µm)
300 W	5 mTorr	Center	4.843	1.4976
		Position 2	8.2123	2.2347
		Position 3	12.1256	3.1884
		Edge	14.1724	2.6207

Table 4-5: Composition of separated FCC and B2 phases after 1-hour 1000 °C anneal. Data gathered using EDS from Edge sample.

Phase	Al	Ti	Cr	Fe	Co	Ni
FCC	9.46 ± 0.56	4.01 ± 0.19	10.94 ± 0.30	16.87 ± 0.28	30.67 ± 0.72	27.83 ± 0.51
B2	27.21 ± 1.65	6.04 ± 0.22	3.51 ± 0.76	9.45 ± 0.67	21.9 ± 0.64	31.64 ± 0.28

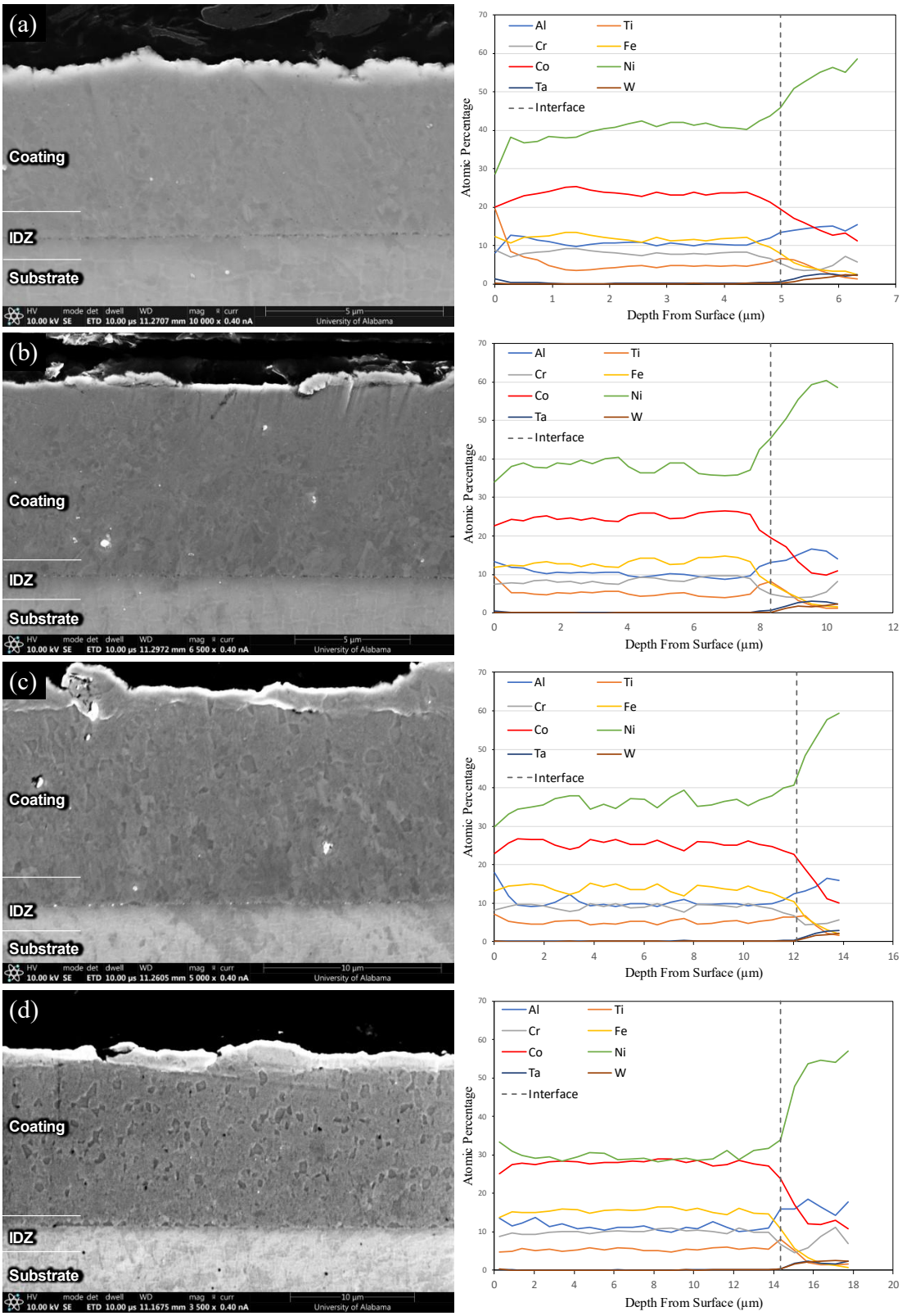

Figure 4-10: Cross section images of the annealed Series 3 coatings (300W, 5 mTorr). (a) Center (b) Position 2 (c) Position 3 and (d) Edge.

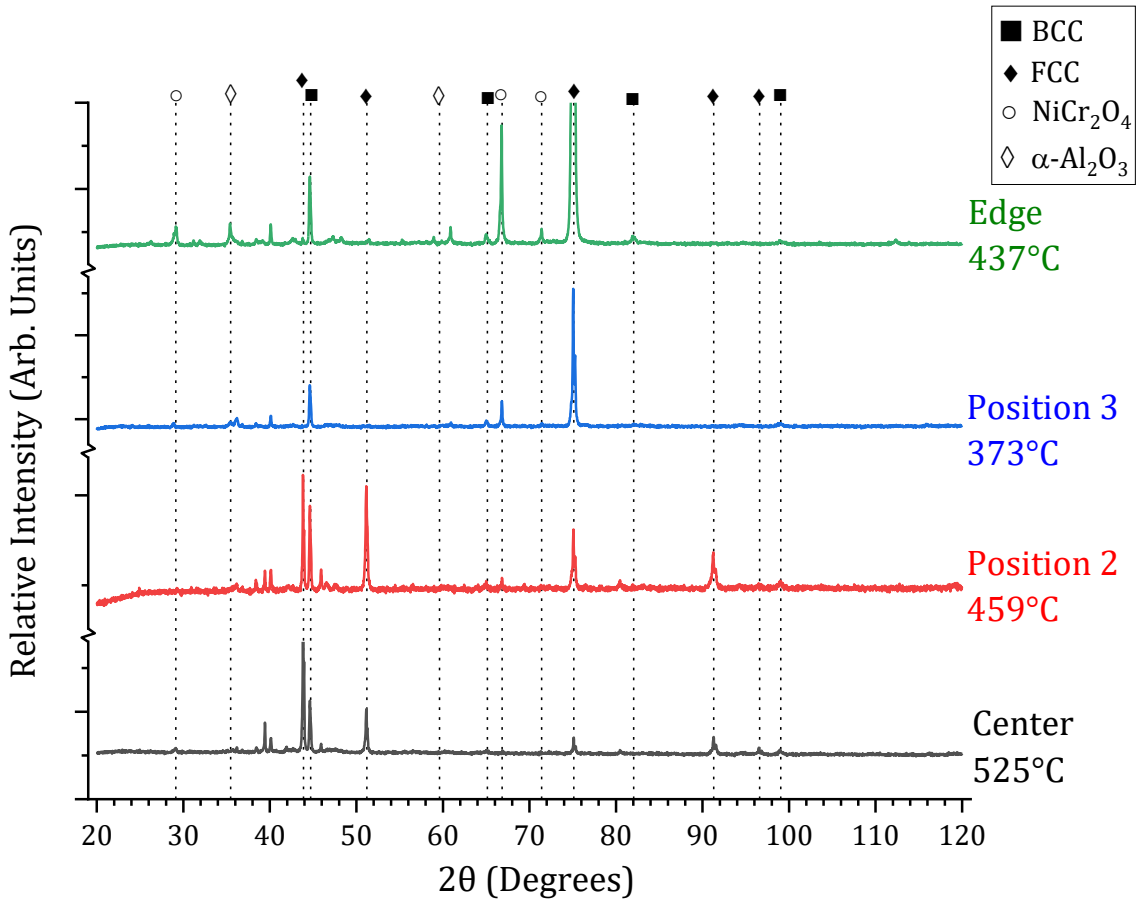

Figure 4-11: XRD patterns for Series 3 coatings. All coatings were annealed at 1000 °C for 1 hour.

Details concerning SZMs and coating morphology are provided in Appendix D. This study has shown that care must be taken when a single sputtering gun is used or when a series of guns are used and are offset from the center of the sample stage. Very different microstructural morphologies can evolve as functions of deposition power, pressure, substrate temperature and angle of incidence to the sputtering source. Angle of incidence and its influence of morphology are often overlooked in combinatorial studies of thin film and coating growth. It is well known that an off-normal deposition flux, enhances columnar growth leading to changes in column shape [124,130,131]. Rather than growing normal to the surface, columns grow towards the adatom source and may change shape due to a combination of substrate surface roughness, homologous temperature, adatom surface mobility, and geometrical shadowing effects. This often gives rise to the formation of several new microstructural morphologies (e.g., rods, columns, protrusions, and equiaxed grains with whiskers) and can lead to dramatic differences in properties such as hardness and chemical diffusion [126].

When producing thin films or coatings by sputtering, lower substrate temperatures tend to be favored to reduce processing costs and to avoid altering the microstructures and properties of the underlying substrate. However, it is well known that increased substrate temperature allows the deposition process to approach thermal equilibrium leading to more favorable properties and lower stress. To obtain high density smooth films at low substrate temperatures, films and coatings should be deposited at lower gas pressures and temperatures under Zone T conditions [55]. Surface roughness must be kept to a minimum as roughness encourages shadowing. Furthermore, where shadowing might be expected changes in deposition conditions (or apparatus) to promote surface diffusion will produce denser films that are more resistant to diffusion [132,133].

CHAPTER 5: SUMMARY, CONCLUSIONS AND FUTURE WORK

5.1 Summary and Conclusions

The goal of this thesis was to provide a better understanding of the influences of processing variables on the morphologies and microstructures of a CCA coating with specific emphasis on the applicability of the SZM to predict coating morphology. Coatings were processed using a single sputter gun that was oriented above the edge location on the substrate plate. A temperature gradient existed in the system running from the substrate plate center out to the edge of the plate. The sputtered $Al_{10}Co_{25}Cr_8Fe_{15}Ni_{36}Ti_6$ coatings exhibit Zone T morphologies when produced at 5 mTorr Ar gas pressure. Coatings produced at 15 and 30 mTorr Ar gas pressure had porous Zone 2 structures which were caused by a shadowing effect resulting from a high angle of incidence during sputtering. This phenomenon was primarily evident in the samples closest to the center of the sputtering stage, farthest away from the sputter guns. This observation supports the work of Mukerjee and Gall who showed that increasing angles of incidence can lead to the formation of well separated columns in the same range where sputtering with no angle of incidence would lead to dense columnar growth [126]. In lower temperature regions, Position 3 and edge, the coatings exhibited mixed structures that were classified as Zone T/2.

XRD analysis revealed that the as-deposited samples possessed the same phases as the bulk alloy. The annealed samples showed similar XRD results with the addition of small oxide peaks. The oxides likely formed during air cooling. The edge and Position 3 annealed samples showed distinct phase separation after the 1000 °C/1 hour anneal.

From the annealed series 2 coatings, it was confirmed that coatings with Zone T microstructures (deposited at 5 mTorr), which were the densest, diffused into the CMSX-8 substrates the least. Work on thicker coatings in the series 3 experiments showed that Zone T coatings deposited at the lowest temperatures interdiffused more rapidly than coatings deposited at higher temperatures. This difference is likely related to a reduction in available grain boundary area due to the growth of larger columns coarsening at higher temperatures or to a change in morphology to a mixture of Zones T and 2. The IDZs assigned in this work were defined based upon EDS composition profiles. More detailed work using more accurate techniques are warranted to obtain quantitative information. The degree of interdiffusion suggests that $Al_{10}Co_{25}Cr_8Fe_{15}Ni_{36}Ti_6$ could function as a diffusion barrier or bond coat under the right service conditions.

5.2 Future Work

Some recommendations for possible future work are provided below.

One of the limiting factors in this study was the inability to reach temperatures above half the melting temperature. Future studies can investigate the growth Zone 3 morphologies either using a higher temperature system or by implementing a combination of substrate biasing and glancing angle deposition as suggested by Mukherjee and Gall. The lower end of the structure zone model spectrum also needs to be researched.

Accurate thermal analysis must also be done for this alloy to better establish the homologous temperature ranges. Current calculations are based upon thermodynamic models that predict solidus temperatures of approximately 1270°C for this alloy. A more accurate determination is needed to better quantify what is happening during deposition.

Given the small amount of diffusion displayed in the 5 mTorr coatings, research could be put into assessing $Al_{10}Co_{25}Cr_8Fe_{15}Ni_{36}Ti_6$ as a potential diffusion barrier coating material. Interestingly, this alloy exhibits less apparent interdiffusion with a CMSX-8 substrate than a thicker NiAl-1Hf coating deposited and annealed under the same conditions. Along with this, annealing parameters should be explored to optimizing the microstructure after the sputtering process but prior to insertion into service.

Imaging of fracture cross-sections rather than the polished cross-sections used in this thesis would improve morphological assessment. Higher resolution imaging is also needed to better quantify coating morphologies. Transmission electron microscopy would allow imaging of substructure and establishment of column orientations.

REFERENCES

[1] B. Cantor, I. T. H. Chang, P. Knight and A. J. B. Vincent, "Microstructural development in equiatomic multicomponent alloys," *Materials Science and Engineering: A*, 375–377 (2004) 213-218. (doi: http://dx.doi.org/10.1016/j.msea.2003.10.257)

[2] J. W. Yeh, S. K. Chen, S. J. Lin, J. Y. Gan, T. S. Chin, T. T. Shun, C. H. Tsau and S. Y. Chang, "Nanostructured high-entropy alloys with multiple principal elements: Novel alloy design concepts and outcomes," *Advanced Engineering Materials*, 6 (2004) 299-303. (doi: 10.1002/adem.200300567)

[3] J. W. Yeh, Y. L. Chen, S. J. Lin and S. K. Chen, "High-entropy alloys - a new era of exploitation," *Materials Science Forum*, 560 (2007) 1-9.

[4] I. Florea, R. M. Florea, O. Baltatescu, V. Soare, R. Chelariu and I. Carcea, "High entropy alloys," *Journal of Optoelectronics and Advanced Materials*, 15 (2013) 761-767.

[5] D. B. Miracle and O. N. Senkov, "A critical review of high entropy alloys and related concepts," *Acta Materialia*, 122 (2017) 448-511. (doi: http://dx.doi.org/10.1016/j.actamat.2016.08.081)

[6] M. C. Gao, J.-W. Yeh, P. K. Liaw and Y. Zhang, eds., High-Entropy Alloys: Fundamentals and Applications (Springer, New York, 2016).

[7] B. S. Murty, J.-W. Yeh and S. Ranganathan, High Entropy Alloys, 2 Edition (Butterworth-Heinemann, Amsterdam, 2019).

[8] Y. Zhang, High-Entropy Materials: A Brief Introduction, (Springer Nature Singapore Pte Ltd., Singapore, 2019).

[9] D. B. Miracle, J. D. Miller, O. N. Senkov, C. Woodward, M. D. Uchic and J. Tiley, "Exploration and Development of High Entropy Alloys for Structural Applications," *Entropy*, 16 (2014) 494-525. (doi: https://doi.org/10.3390/e16010494)

[10] A. M. Manzoni, S. Singh, H. M. Daoud, R. Popp, R. Völkl, U. Glatzel and N. Wanderka, "On the Path to Optimizing the Al-Co-Cr-Cu-Fe-Ni-Ti High Entropy Alloy Family for High Temperature Applications," *Entropy*, 18 (2016) 104.

[11] Q. Ding, Y. Zhang, X. Chen, X. Fu, D. Chen, S. Chen, L. Gu, F. Wei, H. Bei, Y. Gao, M. Wen, J. Li, Z. Zhang, T. Zhu, R. O. Ritchie and Q. Yu, "Tuning element distribution, structure and properties by composition in high-entropy alloys," *Nature*, 574 (2019) 223-227. (doi: 10.1038/s41586-019-1617-1)

[12] S. Haas, A. M. Manzoni, M. Holzinger and U. Glatzel, "Influence of high melting elements on microstructure, tensile strength and creep resistance of the compositionally complex alloy $Al_{10}Co_{25}Cr_8Fe_{15}Ni_{36}Ti_6$," *Materials Chemistry and Physics,* 274 (2021). (doi: 10.1016/j.matchemphys.2021.125163)

[13] M. J. Yao, K. G. Pradeep, C. C. Tasan and D. Raabe, "A novel, single phase, non-equiatomic FeMnNiCoCr high-entropy alloy with exceptional phase stability and tensile ductility," *Scripta Materialia,* 72-73 (2014) 5-8. (doi: 10.1016/j.scriptamat.2013.09.030)

[14] S. Gorsse, D. B. Miracle and O. N. Senkov, "Mapping the world of complex concentrated alloys," *Acta Materialia,* 135 (2017) 177-187. (doi: http://dx.doi.org/10.1016/j.actamat.2017.06.027)

[15] Y. Chen, P. Munroe, Z. Xie and S. Zhang, "High-Entropy Alloy-Based Coatings: Microstructures and Properties," in "Protective Thin Coatings Technology", edited by S. Zhang, J.-M. Ting and W.-Y. Wu (CRC Press, Boca Raton, FL, 2021) p. 205-232.

[16] H. Cheng, Z. Pan, Y. Fu, X. Wang, Y. Wei, H. Luo and X. Li, "Review—Corrosion-Resistant High-Entropy Alloy Coatings: A Review," *Journal of The Electrochemical Society,* 168 (2021) 111502. (doi: 10.1149/1945-7111/ac34d0)

[17] A. K. Das, "A review on coating with high entropy alloy developed by laser energy based surfacing process," *Materials Today: Proceedings,* 52 (2022) 1551-1557. (doi: https://doi.org/10.1016/j.matpr.2021.11.234)

[18] R. K. Duchaniya, U. Pandel and P. Rao, "Coatings based on high entropy alloys: An overview," *Materials Today: Proceedings,* 44 (2021) 4467-4473. (doi: https://doi.org/10.1016/j.matpr.2020.10.720)

[19] J. Li, Y. Huang, X. Meng and Y. Xie, "A Review on High Entropy Alloys Coatings: Fabrication Processes and Property Assessment," *Advanced Engineering Materials,* 21 (2019) 1900343. (doi: https://doi.org/10.1002/adem.201900343)

[20] A. Meghwal, A. Anupam, B. S. Murty, C. C. Berndt, R. S. Kottada and A. S. M. Ang, "Thermal Spray High-Entropy Alloy Coatings: A Review," *Journal of Thermal Spray Technology,* 29 (2020) 857-893. (doi: 10.1007/s11666-020-01047-0)

[21] E. Lewin, "Multi-component and high-entropy nitride coatings—A promising field in need of a novel approach," *Journal of Applied Physics,* 127 (2020) 160901. (doi: 10.1063/1.5144154)

[22] A. D. Pogrebnjak, A. A. Bagdasaryan, I. V. Yakushchenko and V. M. Beresnev, "The structure and properties of high-entropy alloys and nitride coatings based on them," *Russian Chemical Reviews,* 83 (2014) 1027-1061. (doi: 10.1070/rcr4407)

[23] X. H. Yan, J. S. Li, W. R. Zhang and Y. Zhang, "A brief review of high-entropy films," *Materials Chemistry and Physics,* 210 (2018) 12-19. (doi: https://doi.org/10.1016/j.matchemphys.2017.07.078)

[24] S. Akrami, P. Edalati, M. Fuji and K. Edalati, "High-entropy ceramics: Review of principles, production and applications," *Materials Science and Engineering: R: Reports,* 146 (2021) 100644. (doi: https://doi.org/10.1016/j.mser.2021.100644)

[25] J. A. Thornton, "High Rate Thick Film Growth," *Annual Reviews of Materials Science,* 7 (1977) 239-260.

[26] S. K. Padamata, A. Yasinskiy, V. Yanov and G. Saevarsdottir, "Magnetron Sputtering High-Entropy Alloy Coatings: A Mini-Review," *Metals,* 12 (2022) 319. (doi: https://doi.org/10.3390/met12020319)

[27] J. R. Hattrick-Simpers, C. Jun, M. Murakami, A. Orozco, L. Knauss, R. J. Booth, E. W. Greve, S. E. Lofland, M. Wuttig and I. Takeuchi, "High-throughput screening of magnetic properties of quenched metallic-alloy thin-film composition spreads," *Applied Surface Science,* 254 (2007) 734-737. (doi: https://doi.org/10.1016/j.apsusc.2007.07.104)

[28] A. Ludwig, R. Zarnetta, S. Hamann, A. Savan and S. Thienhaus, "Development of multifunctional thin films using high-throughput experimentation methods," *International Journal of Materials Research,* 99 (2008) 1144-1149. (doi: doi:10.3139/146.101746)

[29] Z. Li, A. Ludwig, A. Savan, H. Springer and D. Raabe, "Combinatorial metallurgical synthesis and processing of high-entropy alloys," *Journal of Materials Research,* 33 (2018) 3156-3169. (doi: 10.1557/jmr.2018.214)

[30] V. Chaudhary, R. Chaudhary, R. Banerjee and R. V. Ramanujan, "Accelerated and conventional development of magnetic high entropy alloys," *Materials Today,* 49 (2021) 231-252. (doi: https://doi.org/10.1016/j.mattod.2021.03.018)

[31] D. B. Miracle, M. Li, Z. Zhang, R. Mishra and K. M. Flores, "Emerging Capabilities for the High-Throughput Characterization of Structural Materials," *Annual Review of Materials Research,* 51 (2021) 131-164. (doi: 10.1146/annurev-matsci-080619-022100)

[32] W. Li, P. Liu and P. K. Liaw, "Microstructures and properties of high-entropy alloy films and coatings: a review," *Materials Research Letters,* 6 (2018) 199-229. (doi: 10.1080/21663831.2018.1434248)

[33] N. A. Khan, B. Akhavan, H. Zhou, L. Chang, Y. Wang, L. Sun, M. M. Bilek and Z. Liu, "High entropy alloy thin films of $AlCoCrCu_{0.5}FeNi$ with controlled microstructure," *Applied Surface Science,* 495 (2019) 143560. (doi: https://doi.org/10.1016/j.apsusc.2019.143560)

[34] J.-W. Yeh, S.-J. Lin, M.-H. Tsai and S.-Y. Chang, "High-Entropy Coatings," in "High-Entropy Alloys: Fundamentals and Applications", edited by M. C. Gao, J.-W. Yeh, P. K. Liaw and Y. Zhang (Springer International Publishing, Cham, 2016) p. 469-491.

[35] Y. Zhang, C. C. Koch, S. G. Ma, H. Zhang and Y. Pan, "Fabrication Routes," in "High-Entropy Alloys: Fundamentals and Applications", edited by M. C. Gao, J.-W. Yeh, P. K. Liaw and Y. Zhang (Springer International Publishing, Cham, 2016) p. 151-179.

[36] J.-W. Yeh, A.-C. Yeh and S.-Y. Chang, "Potential Applications and Prospects," in "High-Entropy Alloys: Fundamentals and Applications", edited by M. C. Gao, J.-W. Yeh, P. K. Liaw and Y. Zhang (Springer International Publishing, Cham, 2016) p. 493-512.

[37] M. Tokarewicz and M. Grądzka-Dahlke, "Review of Recent Research on AlCoCrFeNi High-Entropy Alloy," *Metals*, 11 (2021) 1302. (doi: https://doi.org/10.3390/met11081302)

[38] Y. Zhang, Z. Zhang, X. Wang, W. Yao and X. Liang, "Structure and Properties of High-Entropy Amorphous Thin Films: A Review," *JOM*, 74 (2022) 794-807. (doi: 10.1007/s11837-021-05107-w)

[39] Y. Liang, P. Wang, Y. Wang, Y. Dai, Z. Hu, D. E. Tranca, R. Hristu, S. G. Stanciu, A. Toma, G. A. Stanciu, X. Wang and E. Fu, "Growth Mechanisms and the Effects of Deposition Parameters on the Structure and Properties of High Entropy Film by Magnetron Sputtering," *Materials*, 12 (2019) 3008. (doi: https://doi.org/10.3390/ma12183008)

[40] M. El Garah, P. Briois and F. Sanchette, "Recent Progress on High-Entropy Films Deposited by Magnetron Sputtering," *Crystals*, 12 (2022) 335.

[41] A. Savan, T. Allermann, X. Wang, D. Grochla, L. Banko, Y. Kalchev, A. Kostka, J. Pfetzing-Micklich and A. Ludwig, "Structure Zone Investigation of Multiple Principle Element Alloy Thin Films as Optimization for Nanoindentation Measurements," *Materials*, 13 (2020) 2113. (doi: https://doi.org/10.3390/ma13092113)

[42] A. M. Manzoni, S. Haas, J. M. Yu, H. M. Daoud, U. Glatzel, H. Aboulfadl, F. Mucklich, R. Duran, G. Schmitz, D. M. Tobbens, S. Matsumura, F. Vogel and N. Wanderka, "Evolution of γ/γ' phases, their misfit and volume fractions in $Al_{10}Co_{25}Cr_8Fe_{15}Ni_{36}Ti_6$ compositionally complex alloy," *Materials Characterization*, 154 (2019) 363-376. (doi: 10.1016/j.matchar.2019.06.009)

[43] H. M. Daoud, A. Manzoni, R. Volkl, N. Wanderka and U. Glatzel, "Microstructure and tensile behavior of $Al_8Co_{17}Cr_{17}Cu_8Fe_{17}Ni_{33}$ (at.%) high-entropy alloy," *JOM*, 65 (2013) 1805-1814. (doi: 10.1007/s11837-013-0756-3)

[44] A. Manzoni, H. Daoud, S. Mondal, S. Van Smaalen, R. Volkl, U. Glatzel and N. Wanderka, "Investigation of phases in $Al_{23}Co_{15}Cr_{23}Cu_8Fe_{15}Ni_{16}$ and $Al_8Co_{17}Cr_{17}Cu_8Fe_{17}Ni_{33}$ high entropy alloys and comparison with equilibrium phases predicted by Thermo-Calc," *Journal of Alloys and Compounds*, 552 (2013) 430-436. (doi: 10.1016/j.jallcom.2012.11.074)

[45] A. M. Manzoni, H. M. Daoud, R. Voelkl, U. Glatzel and N. Wanderka, "Influence of W, Mo and Ti trace elements on the phase separation in Al8Co17Cr17Cu8Fe17Ni33 based high entropy alloy," *Ultramicroscopy,* 159 (2015) 265-271. (doi: 10.1016/j.ultramic.2015.06.009)

[46] T. M. Butler, K. Garrick and M. L. Weaver, unpublished research, The University of Alabama, 2016.

[47] H. M. Daoud, A. M. Manzoni, N. Wanderka and U. Glatzel, "High-Temperature Tensile Strength of $Al_{10}Co_{25}Cr_8Fe_{15}Ni_{36}Ti_6$ Compositionally Complex Alloy (High-Entropy Alloy)," *JOM,* 67 (2015) 2271-2277. (doi: 10.1007/s11837-015-1484-7)

[48] S. Haas, A. M. Manzoni, F. Krieg and U. Glatzel, "Microstructure and Mechanical Properties of Precipitate Strengthened High Entropy Alloy $Al_{10}Co_{25}Cr_8Fe_{15}Ni_{36}Ti_6$ with Additions of Hafnium and Molybdenum," *Entropy (Basel, Switzerland),* 21 (2019) 169. (doi: 10.3390/e21020169)

[49] P. B. Barna and M. Adamik, "Fundamental structure forming phenomena of polycrystalline films and the structure zone models," *Thin Solid Films,* 317 (1998) 27-33. (doi: https://doi.org/10.1016/S0040-6090(97)00503-8)

[50] S. Craig and G. L. Harding, "Effects of argon pressure and substrate temperature on the structure and properties of sputtered copper films," *Journal of Vacuum Science and Technology,* 19 (1981) 205-215. (doi: 10.1116/1.571105)

[51] C. R. M. Grovenor, H. T. G. Hentzell and D. A. Smith, "The development of grain structure during growth of metallic films," *Acta Metallurgica,* 32 (1984) 773-781. (doi: https://doi.org/10.1016/0001-6160(84)90150-0)

[52] N. Kaiser, "Review of the fundamentals of thin-film growth," *Applied Optics,* 41 (2002) 3053-3060. (doi: 10.1364/AO.41.003053)

[53] E. Kusano, "Revisitation of the structure zone model based on the investigation of the structure and properties of Ti, Zr, and Hf thin films deposited at 70–600 °C using DC magnetron sputtering," *Journal of Vacuum Science & Technology A,* 36 (2018) 041506. (doi: 10.1116/1.5036555)

[54] E. Kusano, "Homologous substrate-temperature dependence of structure and properties of TiO2, ZrO2, and HfO2 thin films deposited by reactive sputtering," *Journal of Vacuum Science & Technology A,* 37 (2019) 051508. (doi: 10.1116/1.5100307)

[55] E. Kusano, "Structure-Zone Modeling of Sputter-Deposited Thin Films: A Brief Review," *Applied Science and Convergence Technology,* 28 (2019) 179-185. (doi: https://doi.org/10.5757/ASCT.2019.28.6.179)

[56] R. Messier, A. P. Giri and R. A. Roy, "Revised structure zone model for thin film physical structure," *Journal of Vacuum Science & Technology A,* 2 (1984) 500-503. (doi: 10.1116/1.572604)

[57] M. El Garah, S. Achache, A. Michau, F. Schuster and F. Sanchette, "Structural and mechanical properties of AlTiTaZr(N) medium entropy films (MEF) obtained by DC magnetron sputtering in dynamic mode," *Surface and Coatings Technology,* 396 (2020) 125941. (doi: https://doi.org/10.1016/j.surfcoat.2020.125941)

[58] M. El Garah, S. Achache, A. Michau, F. Schuster and F. Sanchette, "AlTiTaZr(-N) Medium-Entropy Films Deposited by Magnetron Sputtering with a Combinatorial Approach," *Journal of Materials Engineering and Performance,* 30 (2021) 4063-4071. (doi: 10.1007/s11665-021-05853-7)

[59] Y. S. Kim, H. J. Park, K. S. Lim, S. H. Hong and K. B. Kim, "Structural and Mechanical Properties of AlCoCrNi High Entropy Nitride Films: Influence of Process Pressure," *Coatings,* 10 (2020) 10. (doi: https://doi.org/10.3390/coatings10010010)

[60] Y. Shi, B. Yang, P. D. Rack, S. Guo, P. K. Liaw and Y. Zhao, "High-throughput synthesis and corrosion behavior of sputter-deposited nanocrystalline Alx(CoCrFeNi)100-x combinatorial high-entropy alloys," *Materials & Design,* 195 (2020) 109018. (doi: https://doi.org/10.1016/j.matdes.2020.109018)

[61] Y. J. Li, A. Kostka, A. Savan and A. Ludwig, "Correlative chemical and structural investigations of accelerated phase evolution in a nanocrystalline high entropy alloy," *Scripta Materialia,* 183 (2020) 122-126. (doi: https://doi.org/10.1016/j.scriptamat.2020.03.016)

[62] Y. Deng, Y. F. Guan and P. D. Rack, "Combinatorial synthesis and sputter parameter optimization of chromium-doped yttrium aluminum garnet photoluminescent thin films," *Thin Solid Films,* 515 (2006) 1721-1726. (doi: http://dx.doi.org/10.1016/j.tsf.2006.06.012)

[63] Y. P. Deng, Y. F. Guan, J. D. Fowlkes, S. Q. Wen, F. X. Liu, G. M. Pharr, P. K. Liaw, C. T. Liu and P. D. Rack, "A combinatorial thin film sputtering approach for synthesizing and characterizing ternary ZrCuAl metallic glasses," *Intermetallics,* 15 (2007) 1208-1216. (doi: http://dx.doi.org/10.1016/j.intermet.2007.02.011)

[64] T. Gebhardt, D. Music, T. Takahashi and J. M. Schneider, "Combinatorial thin film materials science: From alloy discovery and optimization to alloy design," *Thin Solid Films,* 520 (2012) 5491-5499. (doi: http://dx.doi.org/10.1016/j.tsf.2012.04.062)

[65] A. Kauffmann, M. Stüber, H. Leiste, S. Ulrich, S. Schlabach, D. V. Szabó, S. Seils, B. Gorr, H. Chen, H.-J. Seifert and M. Heilmaier, "Combinatorial exploration of the High Entropy Alloy System Co-Cr-Fe-Mn-Ni," *Surface and Coatings Technology,* 325 (2017) 174-180. (doi: https://doi.org/10.1016/j.surfcoat.2017.06.041)

[66] A. Marshal, K. G. Pradeep, D. Music, S. Zaefferer, P. S. De and J. M. Schneider, "Combinatorial synthesis of high entropy alloys: Introduction of a novel, single phase, body-centered-cubic FeMnCoCrAl solid solution," *Journal of Alloys and Compounds,* 691 (2017) 683-689. (doi: 10.1016/j.jallcom.2016.08.326)

[67] D. Naujoks, D. Koenig and A. Ludwig, "Exploration of ternary subsystems of superalloys by high-throughput thin film experimentation: Optical and electrical data of the Co-Al-W system," in 2014 MRS Fall Meeting, November 30, 2014 - December 5, 2014 (Materials Research Society, Boston, MA, United states, 2015) p. 145-150. (doi:10.1557/opl.2015.56)

[68] M. A. Payne, J. B. Miller and A. J. Gellman, "High-throughput characterization of early oxidation across AlxFeyNi1- x - y composition space," *Corrosion Science,* 91 (2015) 46-57. (doi: 10.1016/j.corsci.2014.10.034)

[69] M. A. Payne, J. B. Miller and A. J. Gellman, "High-Throughput Screening Across Quaternary Alloy Composition Space: Oxidation of (AlxFeyNi1-x-y)~0.8Cr~0.2," *ACS Combinatorial Science,* 18 (2016) 559-568. (doi: 10.1021/acscombsci.6b00047)

[70] R. Zarnetta, P. J. S. Buenconsejo, A. Savan, S. Thienhaus and A. Ludwig, "High-throughput study of martensitic transformations in the complete Ti–Ni–Cu system," *Intermetallics,* 26 (2012) 98-109. (doi: http://dx.doi.org/10.1016/j.intermet.2012.03.044)

[71] J. W. Yeh, "Alloy design strategies and future trends in high-entropy alloys," *JOM,* 65 (2013) 1759-1771. (doi: 10.1007/s11837-013-0761-6)

[72] Y. Zhang, T. T. Zuo, Z. Tang, M. C. Gao, K. A. Dahmen, P. K. Liaw and Z. P. Lu, "Microstructures and properties of high-entropy alloys," *Progress in Materials Science,* 61 (2014) 1-93. (doi: http://dx.doi.org/10.1016/j.pmatsci.2013.10.001)

[73] T.-K. Tsao, A.-C. Yeh, C.-M. Kuo and H. Murakami, "On The Superior High Temperature Hardness of Precipitation Strengthened High Entropy Ni-Based Alloys," *Advanced Engineering Materials,* 19 (2017). (doi: 10.1002/adem.201600475)

[74] K. Y. Tsai, M. H. Tsai and J. W. Yeh, "Sluggish diffusion in Co–Cr–Fe–Mn–Ni high-entropy alloys," *Acta Materialia,* 61 (2013) 4887-4897. (doi: http://dx.doi.org/10.1016/j.actamat.2013.04.058)

[75] D. L. Beke and G. Erdélyi, "On the diffusion in high-entropy alloys," *Materials Letters,* 164 (2016) 111-113. (doi: http://dx.doi.org/10.1016/j.matlet.2015.09.028)

[76] K. Kulkarni and G. P. S. Chauhan, "Investigations of quaternary interdiffusion in a constituent system of high entropy alloys," *AIP Advances,* 5 (2015). (doi: 10.1063/1.4931806)

[77] W. Kucza, J. Dąbrowa, G. Cieślak, K. Berent, T. Kulik and M. Danielewski, "Studies of “sluggish diffusion” effect in Co-Cr-Fe-Mn-Ni, Co-Cr-Fe-Ni and Co-Fe-Mn-Ni high entropy alloys; determination of tracer diffusivities by combinatorial approach," *Journal of Alloys and Compounds,* 731 (2018) 920-928. (doi: https://doi.org/10.1016/j.jallcom.2017.10.108)

[78] J. Dąbrowa, W. Kucza, G. Cieślak, T. Kulik, M. Danielewski and J.-W. Yeh, "Interdiffusion in the FCC-structured Al-Co-Cr-Fe-Ni high entropy alloys: Experimental studies and numerical simulations," *Journal of Alloys and Compounds,* 674 (2016) 455-462. (doi: http://dx.doi.org/10.1016/j.jallcom.2016.03.046)

[79] J. Dąbrowa and M. Danielewski, "State-of-the-Art Diffusion Studies in the High Entropy Alloys," *Metals,* 10 (2020) 347. (doi: https://doi.org/10.3390/met10030347)

[80] Y. N. Osetsky, L. K. Béland and R. E. Stoller, "Specific features of defect and mass transport in concentrated fcc alloys," *Acta Materialia,* 115 (2016) 364-371. (doi: http://dx.doi.org/10.1016/j.actamat.2016.06.018)

[81] A. Mehta and Y. Sohn, "Investigation of sluggish diffusion in FCC Al0.25CoCrFeNi high-entropy alloy," *Materials Research Letters,* 9 (2021) 239-246. (doi: 10.1080/21663831.2021.1878475)

[82] A. Mehta and Y. H. Sohn, "Fundamental core effects in transition metal high-entropy alloys: 'high-entropy' and 'sluggish diffusion' effects," *Diffusion Foundations,* 29 (2021) 75-93. (doi: https://doi.org/10.4028/www.scientific.net/df.29.75)

[83] Y. J. Zhou, Y. Zhang, Y. L. Wang and G. L. Chen, "Solid solution alloys of AlCoCrFeNiTix with excellent room-temperature mechanical properties," *Applied Physics Letters,* 90 (2007) -. (doi: doi:http://dx.doi.org/10.1063/1.2734517)

[84] X. Yang and Y. Zhang, "Prediction of high-entropy stabilized solid-solution in multi-component alloys," *Materials Chemistry and Physics,* 132 (2012) 233-238. (doi: http://dx.doi.org/10.1016/j.matchemphys.2011.11.021)

[85] Q. He and Y. Yang, "On Lattice Distortion in High Entropy Alloys," *Frontiers in Materials,* 5 (2018). (doi: 10.3389/fmats.2018.00042)

[86] L. R. Owen and N. G. Jones, "Lattice distortions in high-entropy alloys," *Journal of Materials Research,* 33 (2018) 2954-2969. (doi: 10.1557/jmr.2018.322)

[87] S. Ranganathan, "Alloyed pleasures: Multimetallic cocktails," *Current Science,* 85 (2003) 1404-1406.

[88] E. J. Pickering and N. G. Jones, "High-entropy alloys: a critical assessment of their founding principles and future prospects," *International Materials Reviews,* 61 (2016) 183-202. (doi: 10.1080/09506608.2016.1180020)

[89] A. K. Singh and A. Subramaniam, "On the formation of disordered solid solutions in multi-component alloys," *Journal of Alloys and Compounds,* 587 (2014) 113-119. (doi: http://dx.doi.org/10.1016/j.jallcom.2013.10.133)

[90] F. Zhang, C. Zhang, S. L. Chen, J. Zhu, W. S. Cao and U. R. Kattner, "An understanding of high entropy alloys from phase diagram calculations," *Calphad,* 45 (2014) 1-10. (doi: http://dx.doi.org/10.1016/j.calphad.2013.10.006)

[91] S. Fang, X. Xiao, L. Xia, W. Li and Y. Dong, "Relationship between the widths of supercooled liquid regions and bond parameters of Mg-based bulk metallic glasses," *Journal of Non-Crystalline Solids,* 321 (2003) 120-125. (doi: http://dx.doi.org/10.1016/S0022-3093(03)00155-8)

[92] S. Guo and C. T. Liu, "Phase stability in high entropy alloys: Formation of solid-solution phase or amorphous phase," *Progress in Natural Science: Materials International,* 21 (2011) 433-446. (doi: http://dx.doi.org/10.1016/S1002-0071(12)60080-X)

[93] S. Guo, Q. Hu, C. Ng and C. T. Liu, "More than entropy in high-entropy alloys: Forming solid solutions or amorphous phase," *Intermetallics,* 41 (2013) 96-103. (doi: http://dx.doi.org/10.1016/j.intermet.2013.05.002)

[94] F. Otto, Y. Yang, H. Bei and E. P. George, "Relative effects of enthalpy and entropy on the phase stability of equiatomic high-entropy alloys," *Acta Materialia,* 61 (2013) 2628-2638. (doi: http://dx.doi.org/10.1016/j.actamat.2013.01.042)

[95] S. Praveen, B. S. Murty and R. S. Kottada, "Alloying behavior in multi-component AlCoCrCuFe and NiCoCrCuFe high entropy alloys," *Materials Science and Engineering: A,* 534 (2012) 83-89. (doi: http://dx.doi.org/10.1016/j.msea.2011.11.044)

[96] Y. Zhang and W. j. Peng, "Microstructural control and properties optimization of high-entrop alloys," *Procedia Engineering,* 27 (2012) 1169-1178. (doi: http://dx.doi.org/10.1016/j.proeng.2011.12.568)

[97] Y. Zhang, X. Yang and P. K. Liaw, "Alloy design and properties optimization of high-entropy alloys," *JOM,* 64 (2012) 830-838. (doi: 10.1007/s11837-012-0366-5)

[98] Y. Zhang, Y. J. Zhou, J. P. Lin, G. L. Chen and P. K. Liaw, "Solid-Solution Phase Formation Rules for Multi-component Alloys," *Advanced Engineering Materials,* 10 (2008) 534-538. (doi: 10.1002/adem.200700240)

[99] A. Takeuchi and A. Inoue, "Classification of bulk metallic glasses by atomic size difference, heat of mixing and period of constituent elements and its applications to characterization of the main alloying element," *Materials Transactions,* 46 (2005) 2817-2829.

[100] S. Singh, N. Wanderka, B. S. Murty, U. Glatzel and J. Banhart, "Decomposition in multi-component AlCoCrCuFeNi high-entropy alloy," *Acta Materialia,* 59 (2011) 182-190. (doi: https://doi.org/10.1016/j.actamat.2010.09.023)

[101] W.-R. Wang, W.-L. Wang, S.-C. Wang, Y.-C. Tsai, C.-H. Lai and J.-W. Yeh, "Effects of Al addition on the microstructure and mechanical property of AlxCoCrFeNi high-entropy alloys," *Intermetallics,* 26 (2012) 44-51. (doi: http://dx.doi.org/10.1016/j.intermet.2012.03.005)

[102] Y. Zhang and Z. Yunjun, "Solid Solution Formation Criteria for High Entropy Alloys," *Materials Science Forum,* 561-565 (2007) 1337-1339. (doi: https://doi.org/10.4028/www.scientific.net/msf.561-565.1337)

[103] Z. Wang, Y. Huang, J. Wang and C. T. Liu, "Design of high entropy alloys based on the experience from commercial superalloys," *Philosophical Magazine Letters,* 95 (2015) 1-6. (doi: 10.1080/09500839.2014.987841)

[104] T. M. Butler, Phase Stability and Oxidation Behavior of AlNiCoCrFe Based High-Entropy Alloys, Ph.D. Dissertation, The University of Alabama, Tuscaloosa, AL, 2016.

[105] E. P. George, D. Raabe and R. O. Ritchie, "High-entropy alloys," *Nature Reviews Materials,* 4 (2019) 515-534. (doi: 10.1038/s41578-019-0121-4)

[106] E. P. George and R. O. Ritchie, "High-entropy materials," *MRS Bulletin,* (2022). (doi: 10.1557/s43577-022-00285-7)

[107] Y. Zhang, S. G. Ma and J. W. Qiao, "Morphology Transition from Dendrites to Equiaxed Grains for AlCoCrFeNi High-Entropy Alloys by Copper Mold Casting and Bridgman Solidification," *Metallurgical and Materials Transactions A,* 43 (2012) 2625-2630. (doi: 10.1007/s11661-011-0981-8)

[108] H.-Y. Chen, C.-W. Tsai, C.-C. Tung, J.-W. Yeh, T.-T. Shun, C.-C. Yang and S.-K. Chen, "Effect of the substitution of Co by Mn in Al-Cr-Cu-Fe-Co-Ni high-entropy alloys," *Annales De Chimie-science Des Materiaux,* 31 (2006) 685-698. (doi: 10.3166/acsm.31.685-698)

[109] K. B. Zhang, Z. Y. Fu, J. Y. Zhang, J. Shi, W. M. Wang, H. Wang, Y. C. Wang and Q. J. Zhang, "Annealing on the structure and properties evolution of the CoCrFeNiCuAl high-entropy alloy," *Journal of Alloys and Compounds,* 502 (2010) 295-299. (doi: http://dx.doi.org/10.1016/j.jallcom.2009.11.104)

[110] C.-C. Tung, J.-W. Yeh, T.-T. Shun, S.-K. Chen, Y.-S. Huang and H.-C. Chen, "On the elemental effect of AlCoCrCuFeNi high-entropy alloy system," *Materials Letters,* 61 (2007) 1-5. (doi: https://doi.org/10.1016/j.matlet.2006.03.140)

[111] A. Manzoni, H. Daoud, R. Völkl, U. Glatzel and N. Wanderka, "Phase separation in equiatomic AlCoCrFeNi high-entropy alloy," *Ultramicroscopy,* 132 (2013) 212-215. (doi: http://dx.doi.org/10.1016/j.ultramic.2012.12.015)

[112] M. Detrois, P. D. Jablonski, S. Antonov, S. Li, Y. Ren, S. Tin and J. A. Hawk, "Design and thermomechanical properties of a γ′ precipitate-strengthened Ni-based superalloy with high entropy γ matrix," *Journal of Alloys and Compounds,* 792 (2019) 550-560. (doi: https://doi.org/10.1016/j.jallcom.2019.04.054)

[113] T. Rieger, J. M. Joubert, M. Laurent-Brocq, L. Perrière, I. Guillot and J. P. Couzinié, "Study of the FCC+$L1_2$ two-phase region in complex concentrated alloys based on the Al–Co–Cr–Fe–Ni–Ti system," *Materialia,* 14 (2020) 100905. (doi: https://doi.org/10.1016/j.mtla.2020.100905)

[114] N. D. Stepanov, D. G. Shaysultanov, M. A. Tikhonovsky and S. V. Zherebtsov, "Structure and high temperature mechanical properties of novel non-equiatomic Fe-(Co, Mn)-Cr-Ni-Al-(Ti) high entropy alloys," *Intermetallics,* 102 (2018) 140-151. (doi: https://doi.org/10.1016/j.intermet.2018.09.010)

[115] J. Joseph, M. Annasamy, S. R. Kada, P. D. Hodgson, M. R. Barnett and D. M. Fabijanic, "Optimising the Al and Ti compositional window for the design of γ' (L12)-strengthened Al–Co–Cr–Fe–Ni–Ti high entropy alloys," *Materials Science and Engineering: A,* 835 (2022) 142620. (doi: https://doi.org/10.1016/j.msea.2022.142620)

[116] J. Chen, X. Zhou, W. Wang, B. Liu, Y. Lv, W. Yang, D. Xu and Y. Liu, "A review on fundamental of high entropy alloys with promising high–temperature properties," *Journal of Alloys and Compounds,* 760 (2018) 15-30. (doi: https://doi.org/10.1016/j.jallcom.2018.05.067)

[117] P. Pandey, S. Kashyap, D. Palanisamy, A. Sharma and K. Chattopadhyay, "On the high temperature coarsening kinetics of γ′ precipitates in a high strength Co37.6Ni35.4Al9.9Mo4.9Cr5.9Ta2.8Ti3.5 fcc-based high entropy alloy," *Acta Materialia,* 177 (2019) 82-95. (doi: https://doi.org/10.1016/j.actamat.2019.07.011)

[118] Y.-T. Chen, Y.-J. Chang, H. Murakami, S. Gorsse and A.-C. Yeh, "Designing high entropy superalloys for elevated temperature application," *Scripta Materialia,* 187 (2020) 177-182. (doi: 10.1016/j.scriptamat.2020.06.002)

[119] H.-C. Chen and J.-W. Yeh, "High-Entropy Coatings," in "Encyclopedia of Materials: Metals and Alloys", edited by F. G. Caballero (Elsevier, Oxford, 2022) p. 558-568.

[120] J. A. Thornton, "Influence of Apparatus Geometry and Deposition Conditions on the Structure and Topography of Thick Sputtered Coatings," *Journal of Vacuum Science and Technology,* 11 (1974) 666-670. (doi: https://doi.org/10.1116/1.1312732)

[121] T. K. Chen, T. T. Shun, J. W. Yeh and M. S. Wong, "Nanostructured nitride films of multi-element high-entropy alloys by reactive DC sputtering," *Surface and Coatings Technology,* 188-189 (2004) 193-200. (doi: https://doi.org/10.1016/j.surfcoat.2004.08.023)

[122] INCONEL® Alloy 625 Spec Sheet, (Special Metals, 2013).

[123] A. M. Manzoni, S. Haas, H. Daoud, U. Glatzel, C. Förster and N. Wanderka, "Tensile Behavior and Evolution of the Phases in the $Al_{10}Co_{25}Cr_8Fe_{15}Ni_{36}Ti_6$ Compositionally Complex/High Entropy Alloy," *Entropy,* 20 (2018) 646. (doi: https://doi.org/10.3390/e20090646)

[124] A. Lakhtakia and R. Messier, Sculptured Thin Films: Nanoengineered Morphology and Optics, (SPIE - The International Society for Optical Engineering, Bellingham, WA, 2005).

[125] M. Ohring, Materials Science of Thin Films, 2nd Edition (Academic Press, San Diego, 2002).

[126] S. Mukherjee and D. Gall, "Structure zone model for extreme shadowing conditions," *Thin Solid Films*, 527 (2013) 158-163. (doi: https://doi.org/10.1016/j.tsf.2012.11.007)

[127] E. J. Mittemeijer, "Microstructure and Diffusion," in "Fundamentals of Materials Science" (Springer, 2021) p. 450-460.

[128] α-Al_2O_3, ICDD file No. 00-046-1212, in "International Centre for Diffraction Data", edited by ICDD (International Centre for Diffraction Data, Newtown Square, PA 2010).

[129] $Ni(Cr_2O_4)$, ICDD file No. 01-088-0108, edited by ICDD (International Centre for Diffraction Data, Newtown Square, PA 2010).

[130] D. M. Mattox, Handbook of Physical Vapor Deposition (PVD) Processing, Second Edition (Elsevier, Amsterdam, The Netherlands, 2010).

[131] A. Barranco, A. Borras, A. R. Gonzalez-Elipe and A. Palmero, "Perspectives on oblique angle deposition of thin films: From fundamentals to devices," *Progress in Materials Science*, 76 (2016) 59-153. (doi: https://doi.org/10.1016/j.pmatsci.2015.06.003)

[132] R. F. Bunshah, "Thin films of refractory metals and refractory compounds," in Tungsten and Tungsten Alloys: Recent Advances, edited by A. Crowson and E. S. Chen (The Minerals, Metals and Materials Society, Metals Park, OH, 1991) p. 245-255.

[133] R. F. Bunshah, ed., Handbook of Deposition Technologies for Films and Coatings: Science, Technology and Applications (Noyes Publications, Park Ridge, NJ, 1994).

[134] B. A. Movchan and A. V. Demchishin, "Investigation of the structure and properties of thick vacuum- deposited films of nickel, titanium, tungsten, alumina and zirconium dioxide," *Fizika Metallov i Metallovedenie*, 28 (1969) 653-660.

[135] P. J. Kelly and R. D. Arnell, "Development of a novel structure zone model relating to the closed-field unbalanced magnetron sputtering system," *Journal of Vacuum Science & Technology A*, 16 (1998) 2858-2869. (doi: 10.1116/1.581432)

APPENDIX A: TEMPERATURE GRADIENT DERIVATION

Assumptions:

- Center of the heating stage is reaching the setpoint temperature
- Power from bulbs is lessened according to Inverse-Square Law
- Assume bulb is a perfect cylinder with radius and height 18.55 mm and 53.05 mm respectively
- Only upward facing surface of the bulb is supplying heat to the plate
- Only method of heat transfer through the stage is conduction
- Heating contact area of the plate is circular with a radius of 38.1 mm (1.5 in)
- Distance from edge of heating area to the edge of the plate is 38.1 mm (1.5 in)

Determining heat transfer to the stage:

Using the measurements of the bulb and the equation for the surface area along the length of a cylinder, the bulb surface area was calculated as follows:

$$A = \pi d h \tag{A-1}$$

$$A = \pi \cdot 0.01855 \text{ m} \cdot 0.05305 \text{ m} \tag{A-2}$$

$$A = 0.00309157 \text{ m}^2 \tag{A-3}$$

Assuming only the upward facing edge is heating the stage, we divide this area in half to obtain the effective bulb surface area, A_{eff}:

$$A_{eff} = \frac{0.00309157\text{m}^2}{2} = 0.001545785 \text{ m}^2 \tag{A-4}$$

The heating contact area, A_{hc}, was calculated to be:

$$A_{hc} = \pi r^2 = \pi \cdot 0.0381^2 m^2 = 0.004560367 \text{ m}^2 \tag{A-5}$$

The Inverse-Square Law states that the energy transfer to the sample stage is inversely proportional to the ratio of the areas:

$$\frac{A_{hc}}{A_{eff}} = \frac{0.004560357 \text{ m}^2}{0.001545785\, m^2} = 2.95 \tag{A-6}$$

Given two 1000 W bulbs and the inverse-square law ratio, the heat transfer power is calculated to be:

$$\frac{1000 \text{ W} * 2 \text{ bulbs}}{2.95} = 678 \text{ W} \tag{A-7}$$

Calculating edge temperature:

Conduction heat transfer equation

$$q = \frac{k}{s} \cdot A \cdot (T_1 - T_2) \tag{A-8}$$

Value for thickness s is the distance from the edge of the heating area to the edge of the substrate plate, i.e., 38.1 mm. Substituting values, we find:

$$678 \text{ W} = \frac{19 \text{ W/m°C}}{0.0381 \text{ m}} \cdot (0.004560367 \text{ m}^2) \cdot (650 - T_2) \tag{A-9}$$

where T_2 is in this case, the edge temperature. Solving we find:

$$\text{Edge Temeprature} = 350\ °C$$

If this calculation is repeated for Position 3 samples at 12.7 mm from the edge of the heating area, we find:

$$\text{Position 3 Temperature} = 545\ ℃$$

APPENDIX B: COMPOSITION PROFILES FOR AS-DEPOSITED SERIES 2 COATINGS

The 11 figures provided in this appendix are the EDS composition profiles for the as-deposited Series 2 coatings. The profiles verify that there was no interdiffusion between the coatings and superalloy substrates during deposition.

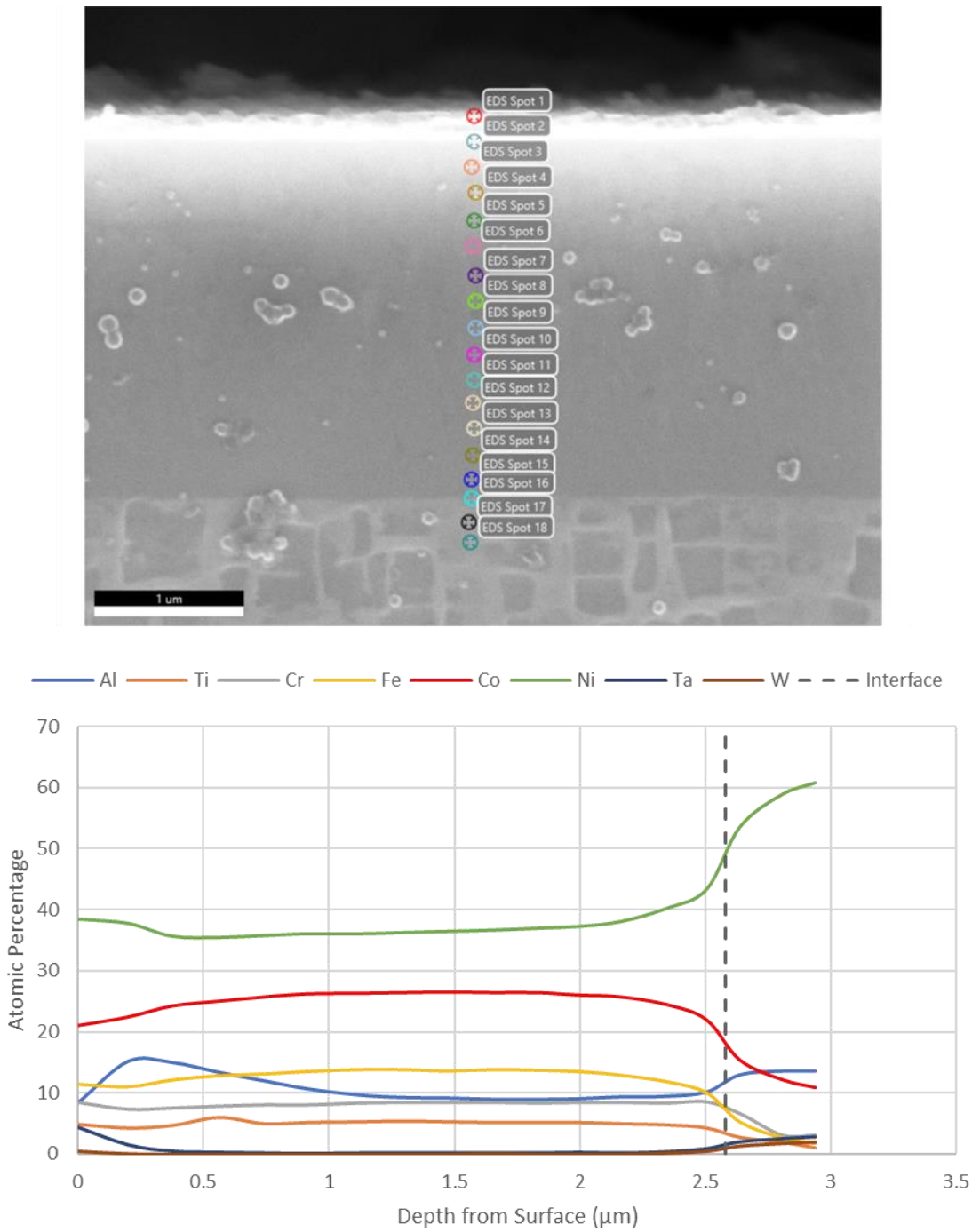

Figure B-1: (a) SEM image of the region of analysis and (b) corresponding EDS composition profile for a Series 2 coating deposited at 5 mTorr. Center substrate plate position.

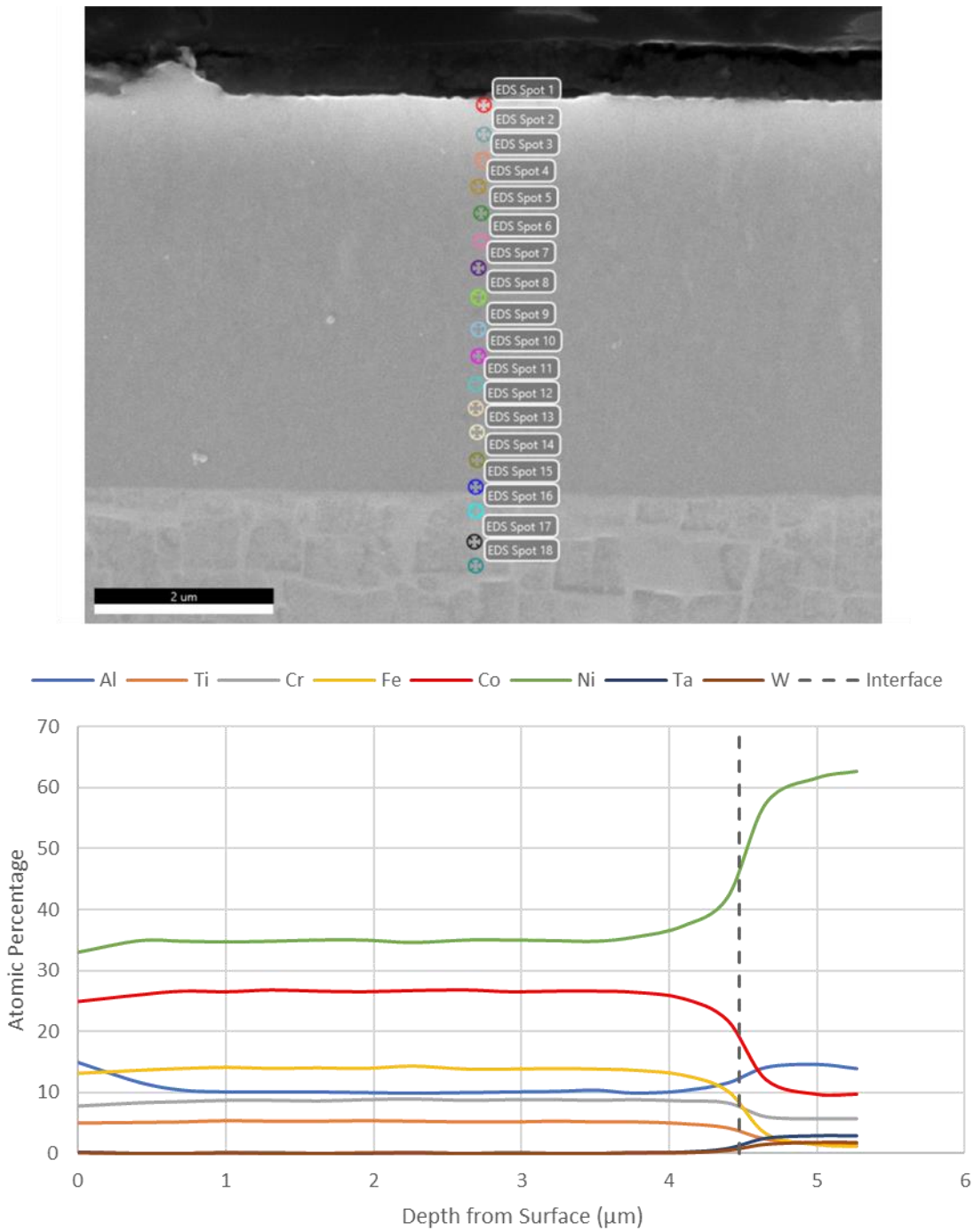

Figure B-2: (a) SEM image of the region of analysis and (b) corresponding EDS composition profile for a Series 2 coating deposited at 5 mTorr. Substrate plate Position 2.

Figure B-3: (a) SEM image of the region of analysis and (b) corresponding EDS composition profile for a Series 2 coating deposited at 5 mTorr. Substrate plate Position 3.

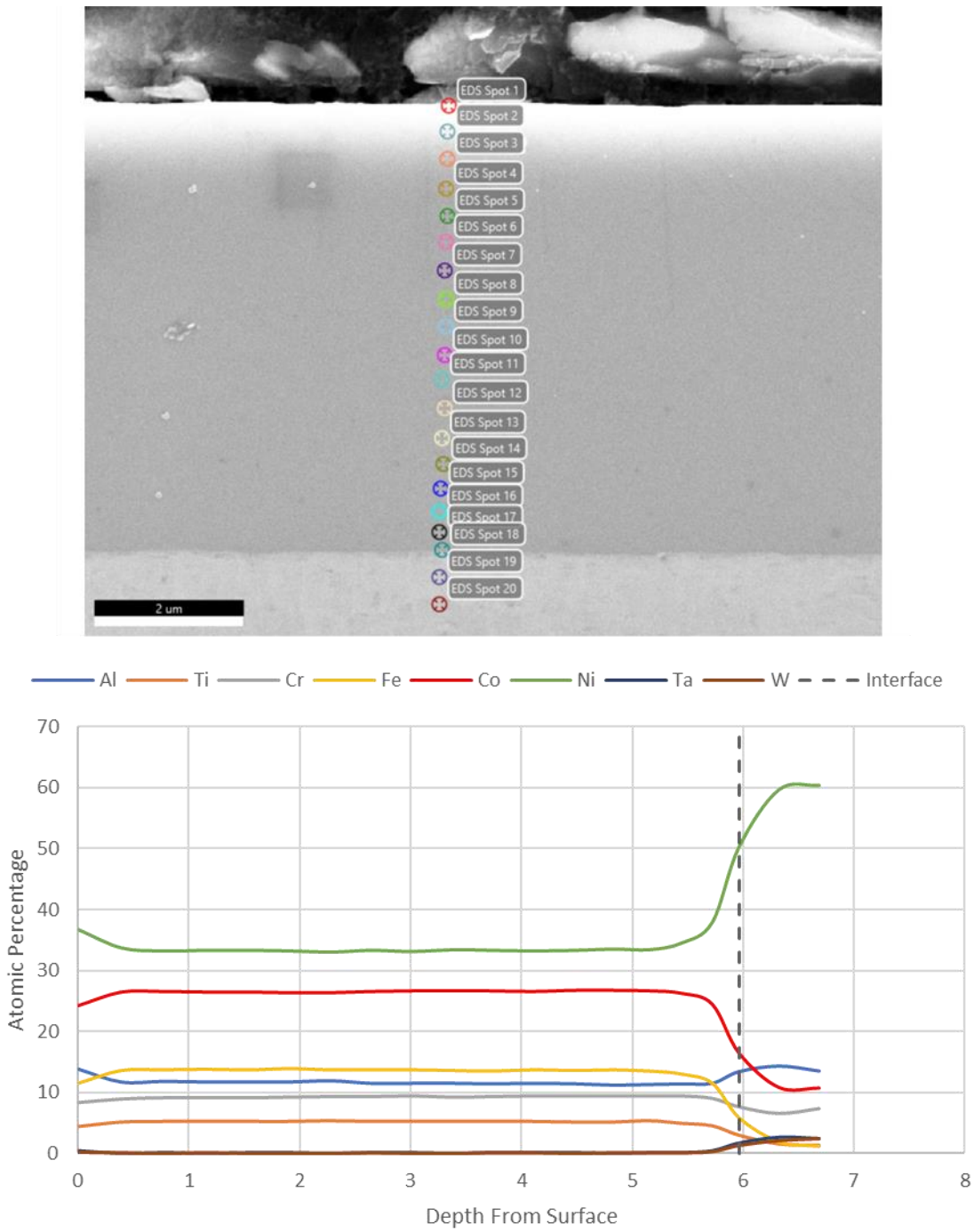

Figure B-4: (a) SEM image of the region of analysis and (b) corresponding EDS composition profile for a Series 2 coating deposited at 5 mTorr. Edge position on substrate plate.

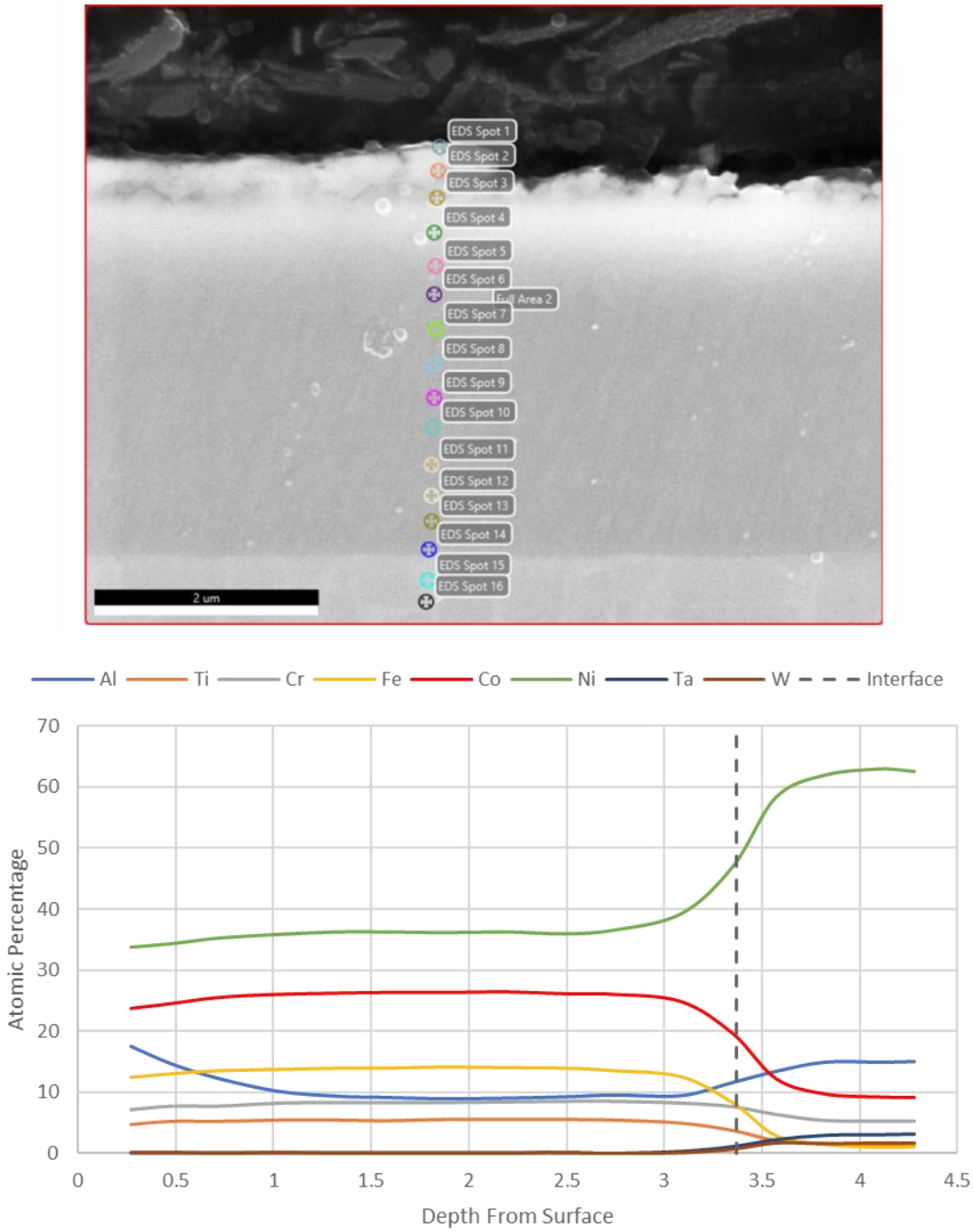

Figure B-5: (a) SEM image of the region of analysis and (b) corresponding EDS composition profile for a Series 2 coating deposited at 15 mTorr. Position 2 on substrate plate.

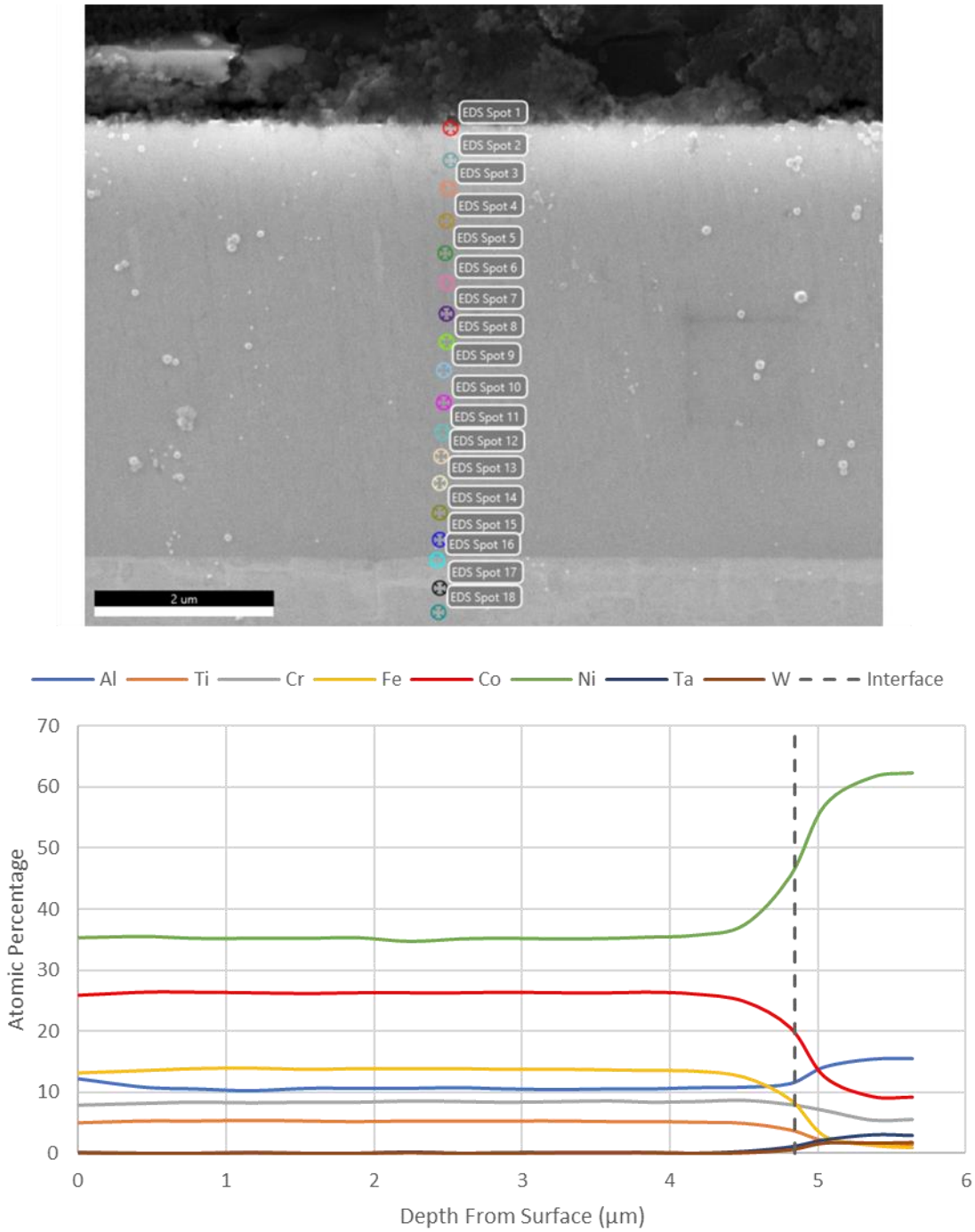

Figure B-6: (a) SEM image of the region of analysis and (b) corresponding EDS composition profile for a Series 2 coating deposited at 15 mTorr. Position 3 on substrate plate.

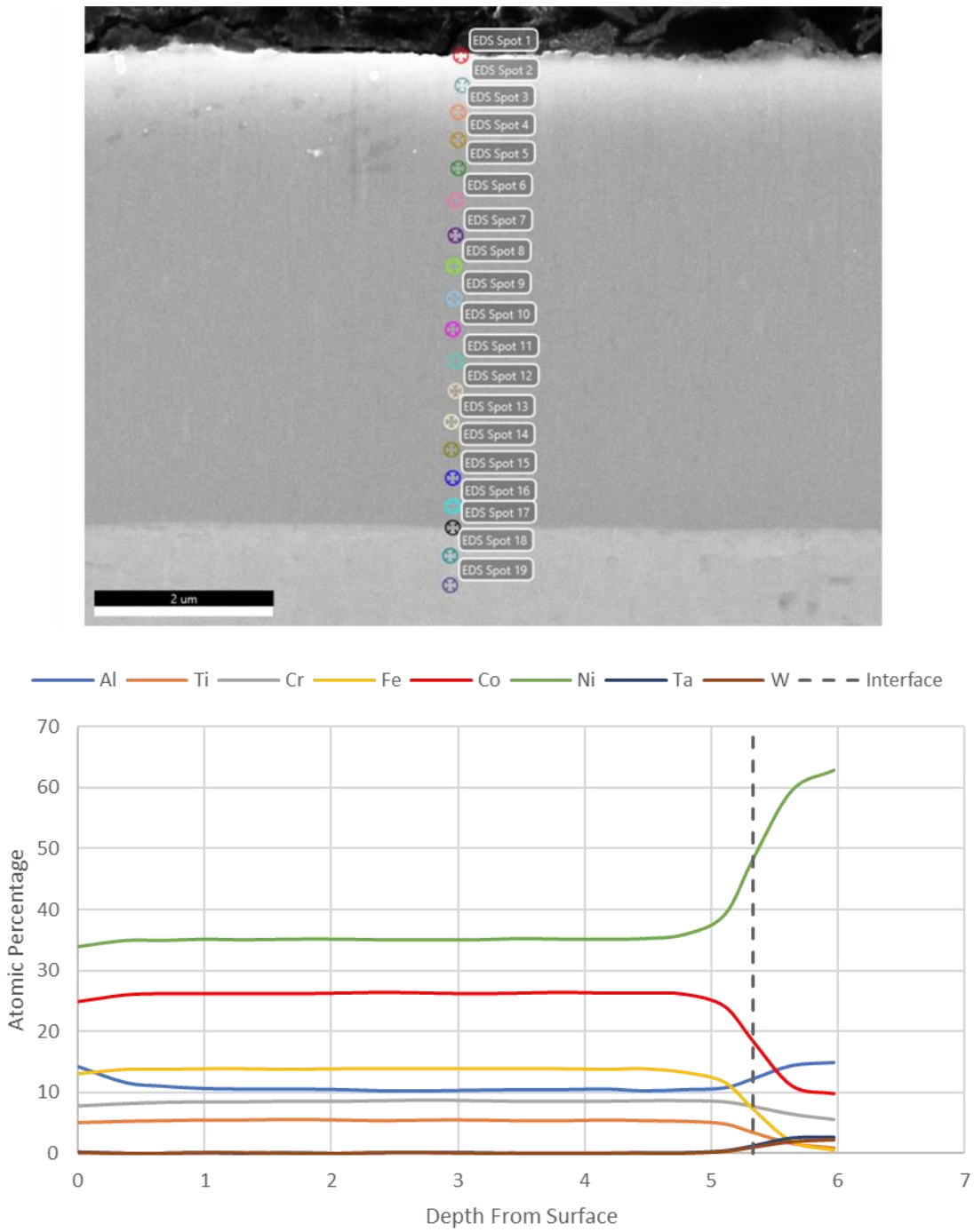

Figure B-7: (a) SEM image of the region of analysis and (b) corresponding EDS composition profile for a Series 2 coating deposited at 15 mTorr. Edge on substrate plate.

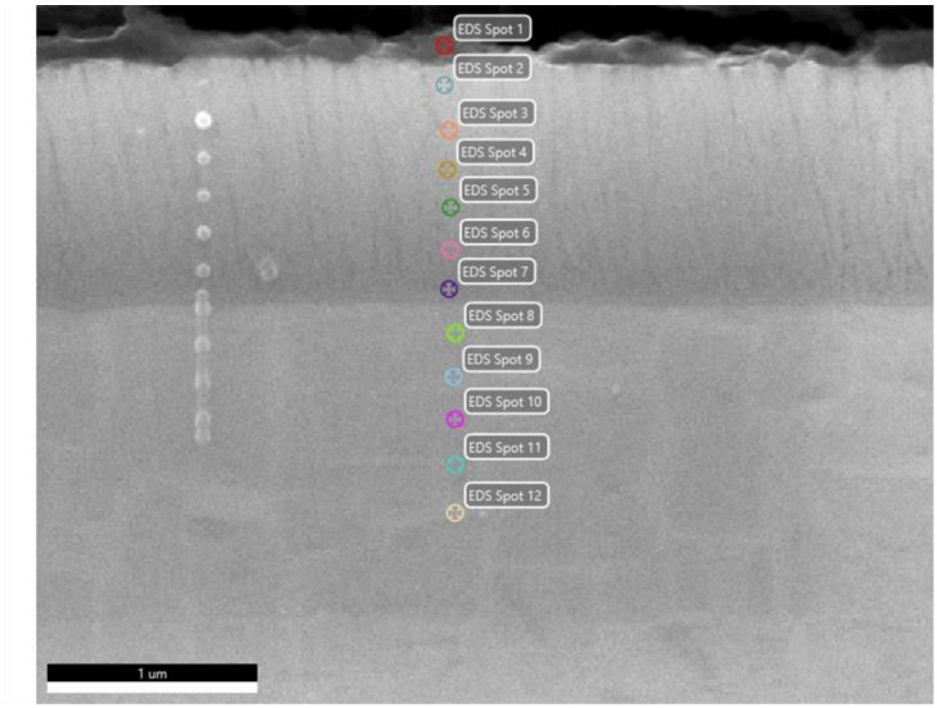

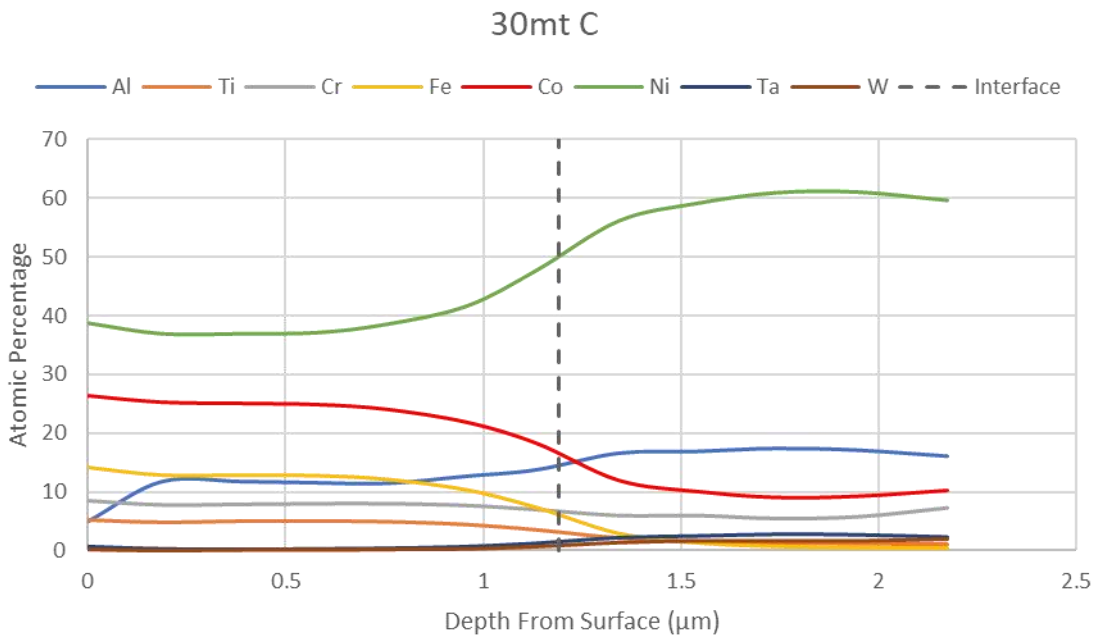

Figure B-8: (a) SEM image of the region of analysis and (b) corresponding EDS composition profile for a Series 2 coating deposited at 30 mTorr. Center position on substrate plate.

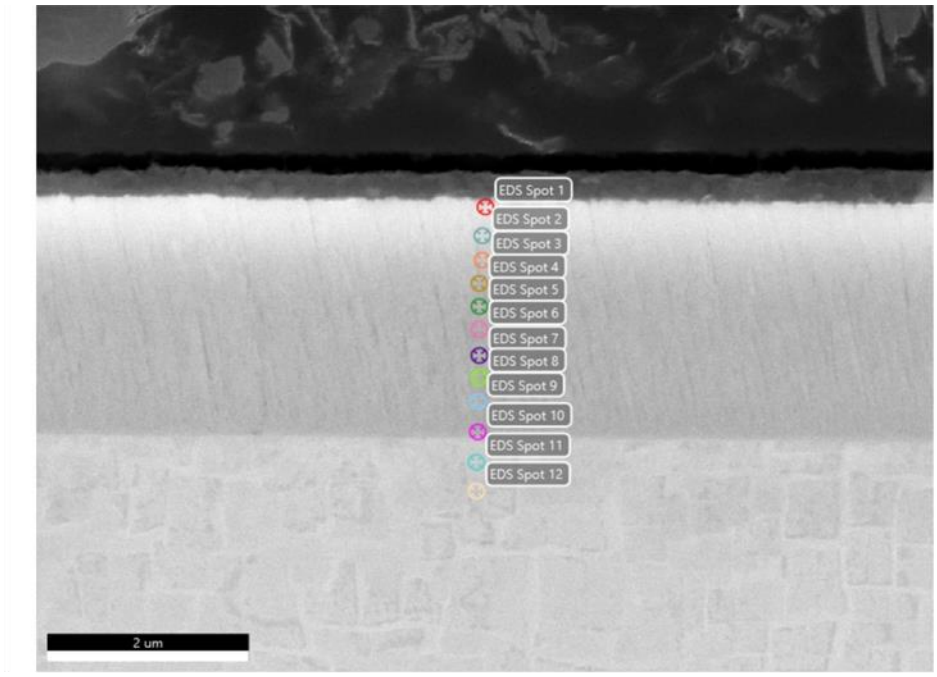

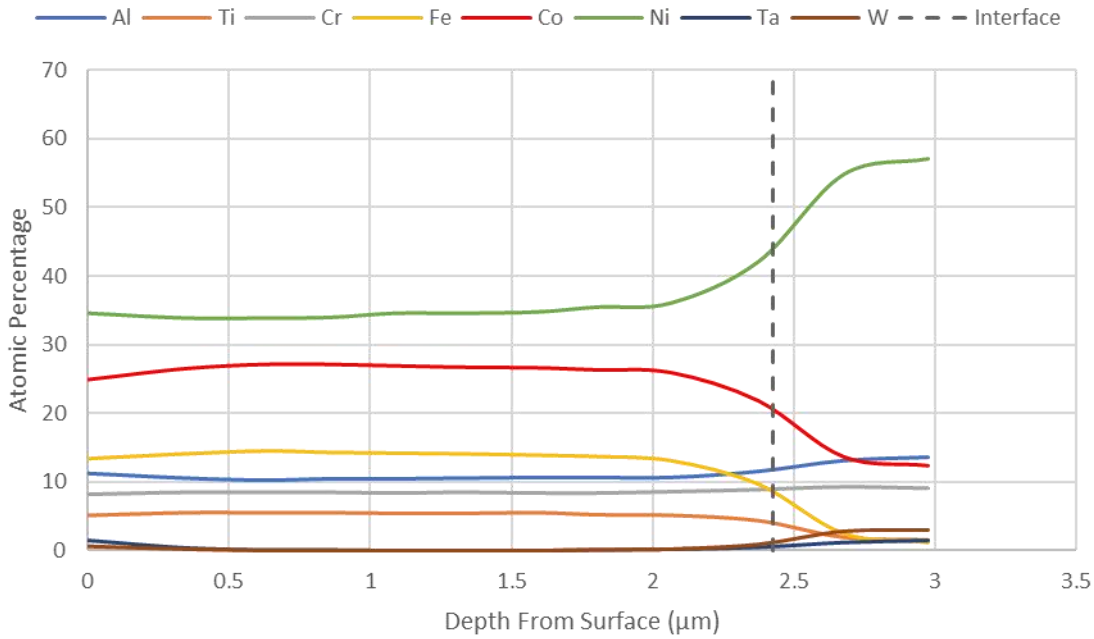

Figure B-9: (a) SEM image of the region of analysis and (b) corresponding EDS composition profile for a Series 2 coating deposited at 30 mTorr. Position 2 on substrate plate.

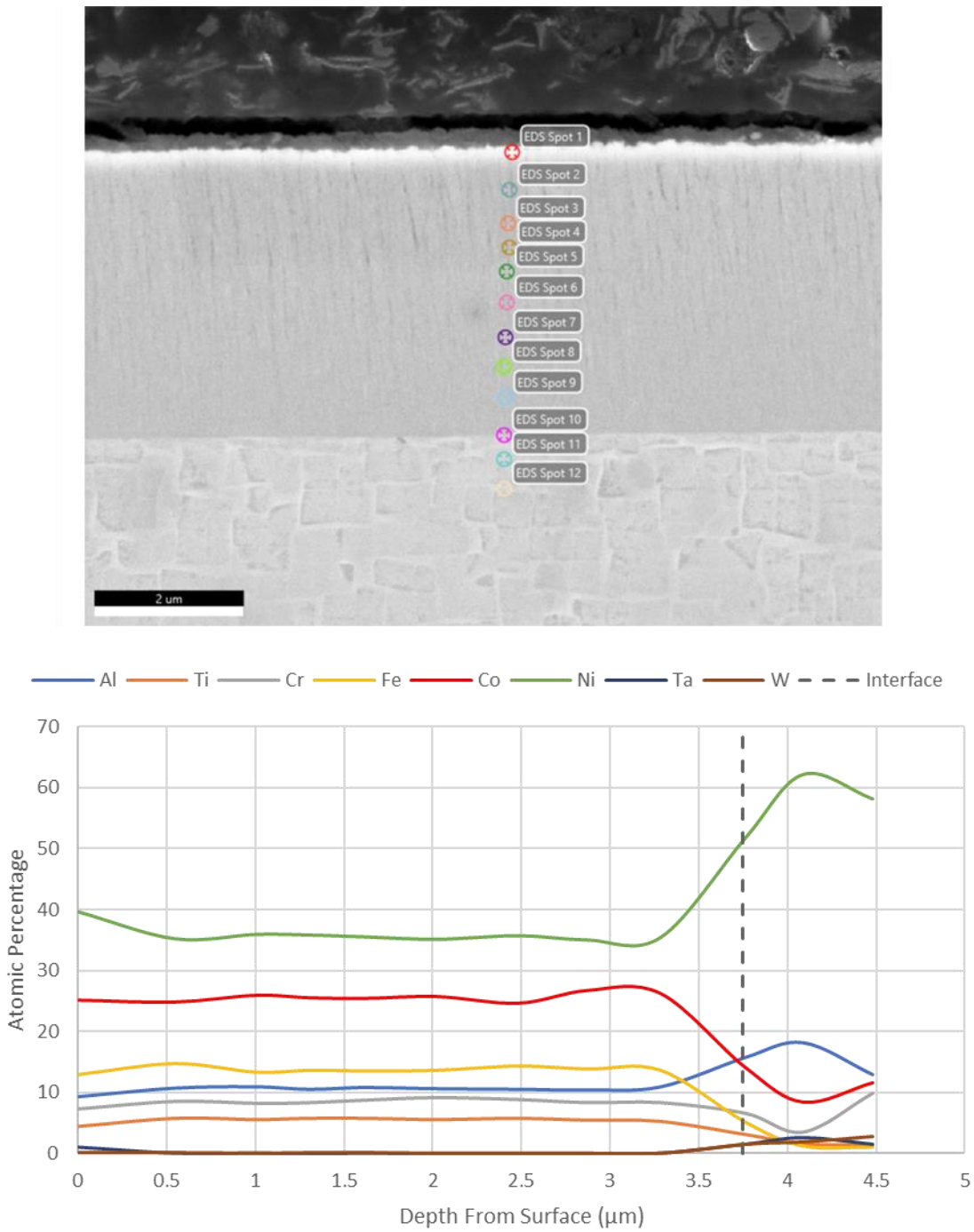

Figure B-10: (a) SEM image of the region of analysis and (b) corresponding EDS composition profile for a Series 2 coating deposited at 30 mTorr. Position 3 on substrate plate.

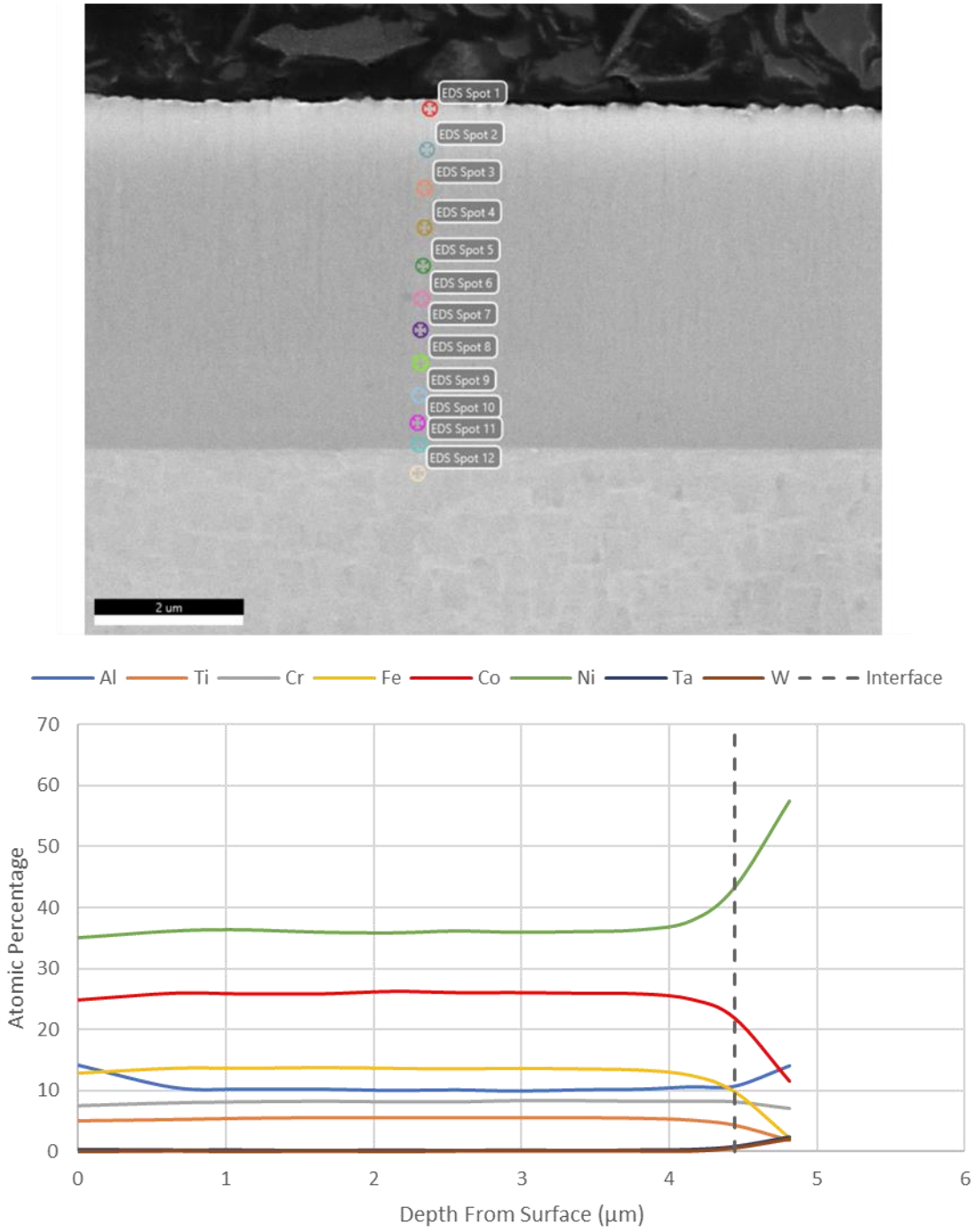

Figure B-11: (a) SEM image of the region of analysis and (b) corresponding EDS composition profile for a Series 2 coating deposited at 30 mTorr. Edge of substrate plate.

APPENDIX C: COMPOSITION PROFILES FOR ANNEALED SERIES 2 COATINGS

The 12 figures provided in this appendix are the EDS the composition profiles for the Series 2 coatings after annealing at 1000°C/1h. The images reveal complete coating degradation for the porous Zone 2 coatings deposited at 30 mTorr. The profiles show that coating/substrate interdiffusion occurred with the most porous coatings exhibiting the highest degree of interdiffusion. The degree of interdiffusion generally decreased as coating density and thickness increased.

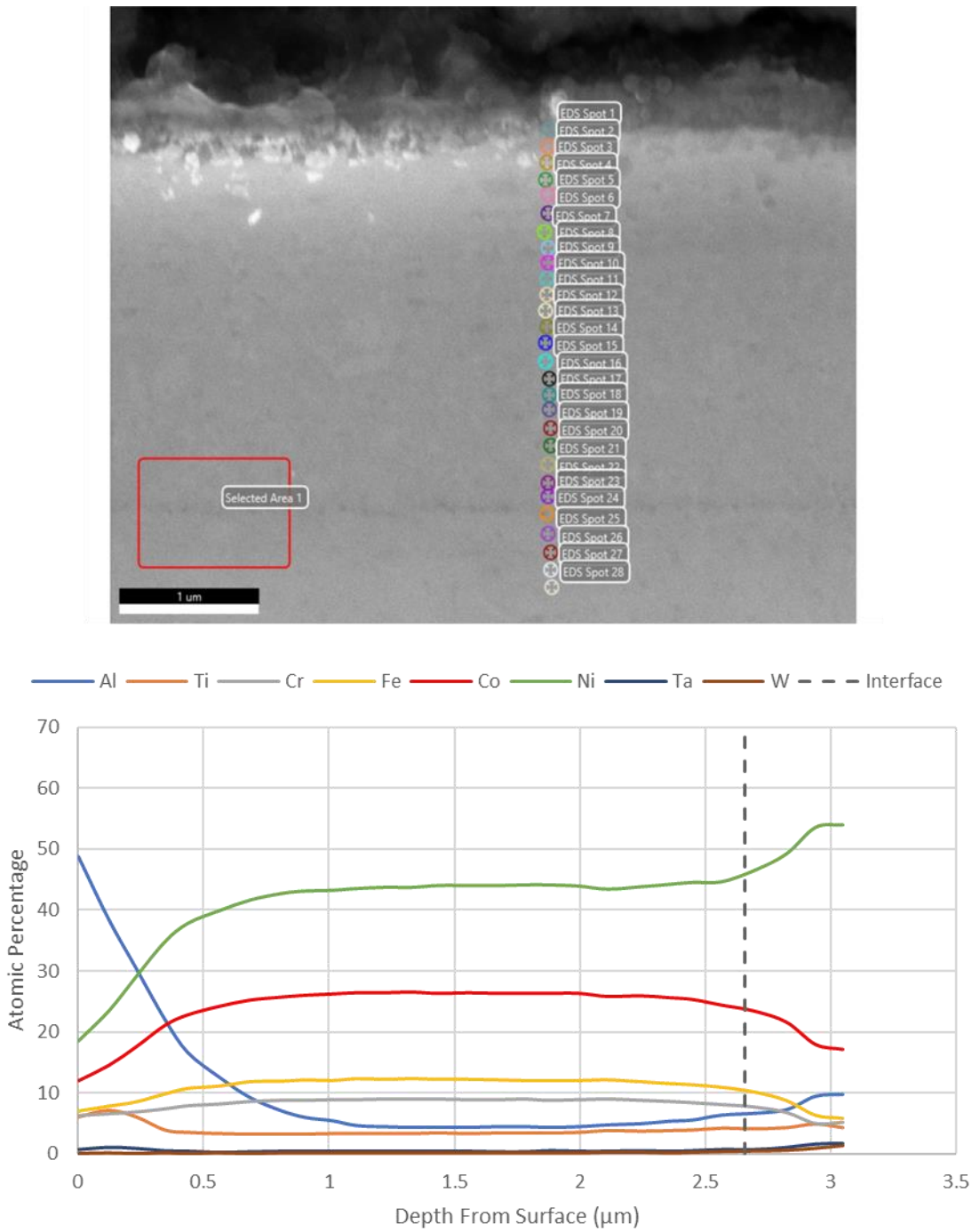

Figure C-1: (a) SEM image of the region of analysis and (b) corresponding EDS composition profile for an annealed Series 2 coating deposited at 5 mTorr. Center of substrate plate.

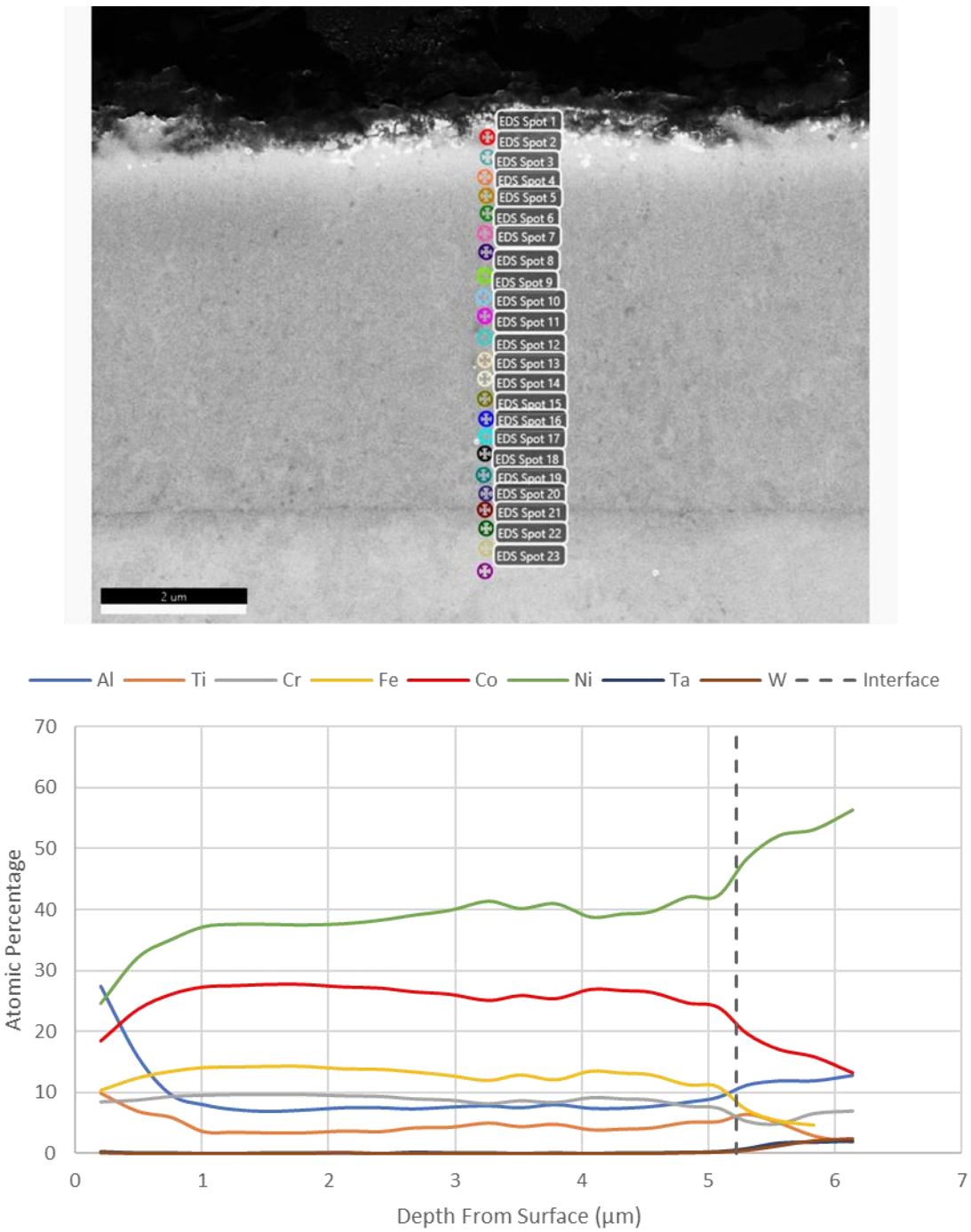

Figure C-2: (a) SEM image of the region of analysis and (b) corresponding EDS composition profile for an annealed Series 2 coating deposited at 5 mTorr. Position 2 of substrate plate.

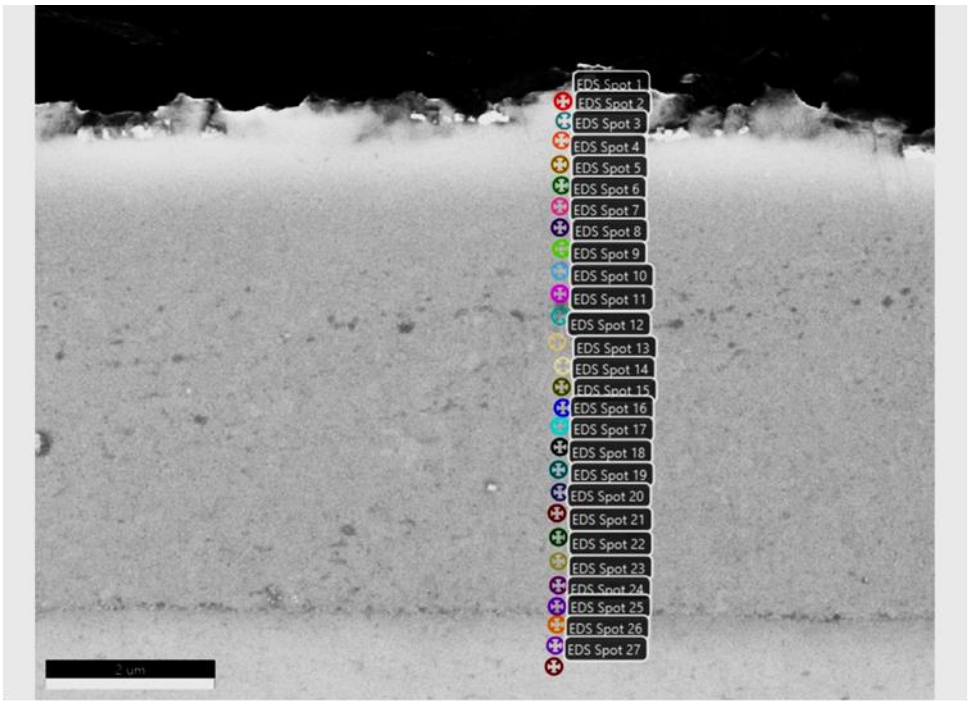

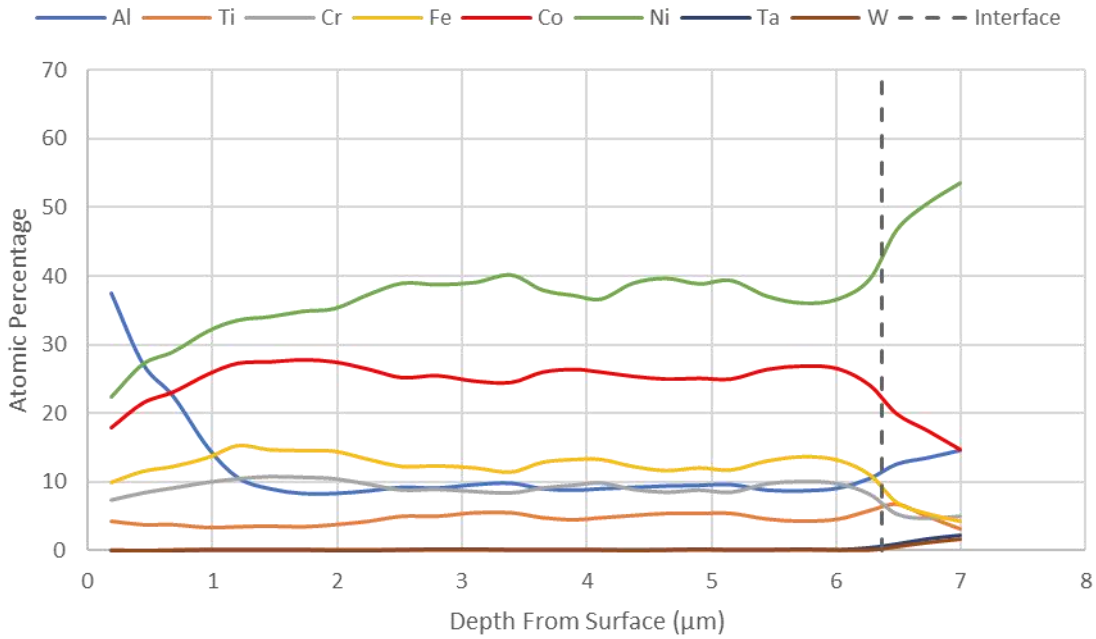

Figure C-3: (a) SEM image of the region of analysis and (b) corresponding EDS composition profile for an annealed Series 3 coating deposited at 5 mTorr. Position 2 of substrate plate.

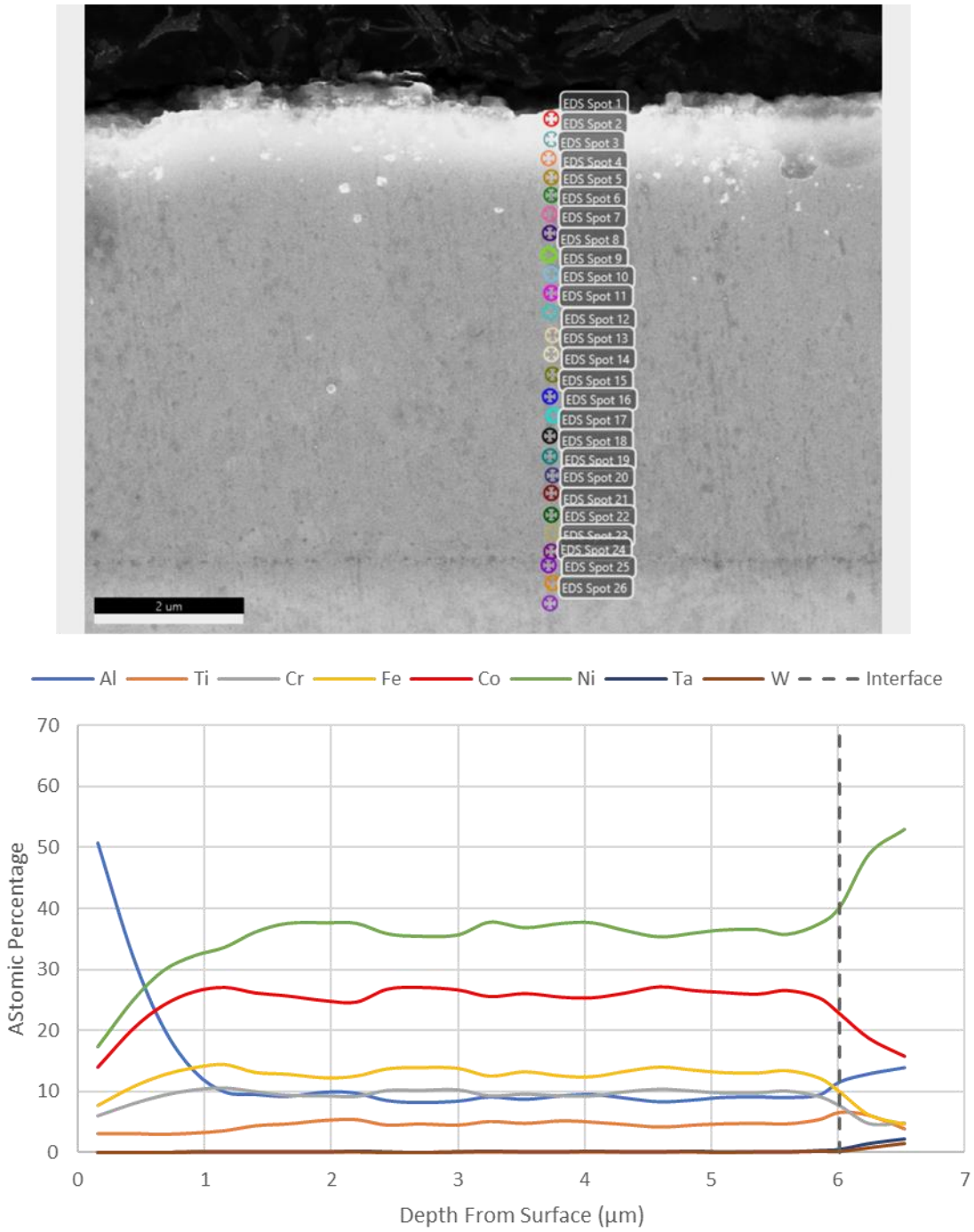

Figure C-4: (a) SEM image of the region of analysis and (b) corresponding EDS composition profile for an annealed Series 2 coating deposited at 5 mTorr. Edge of substrate plate.

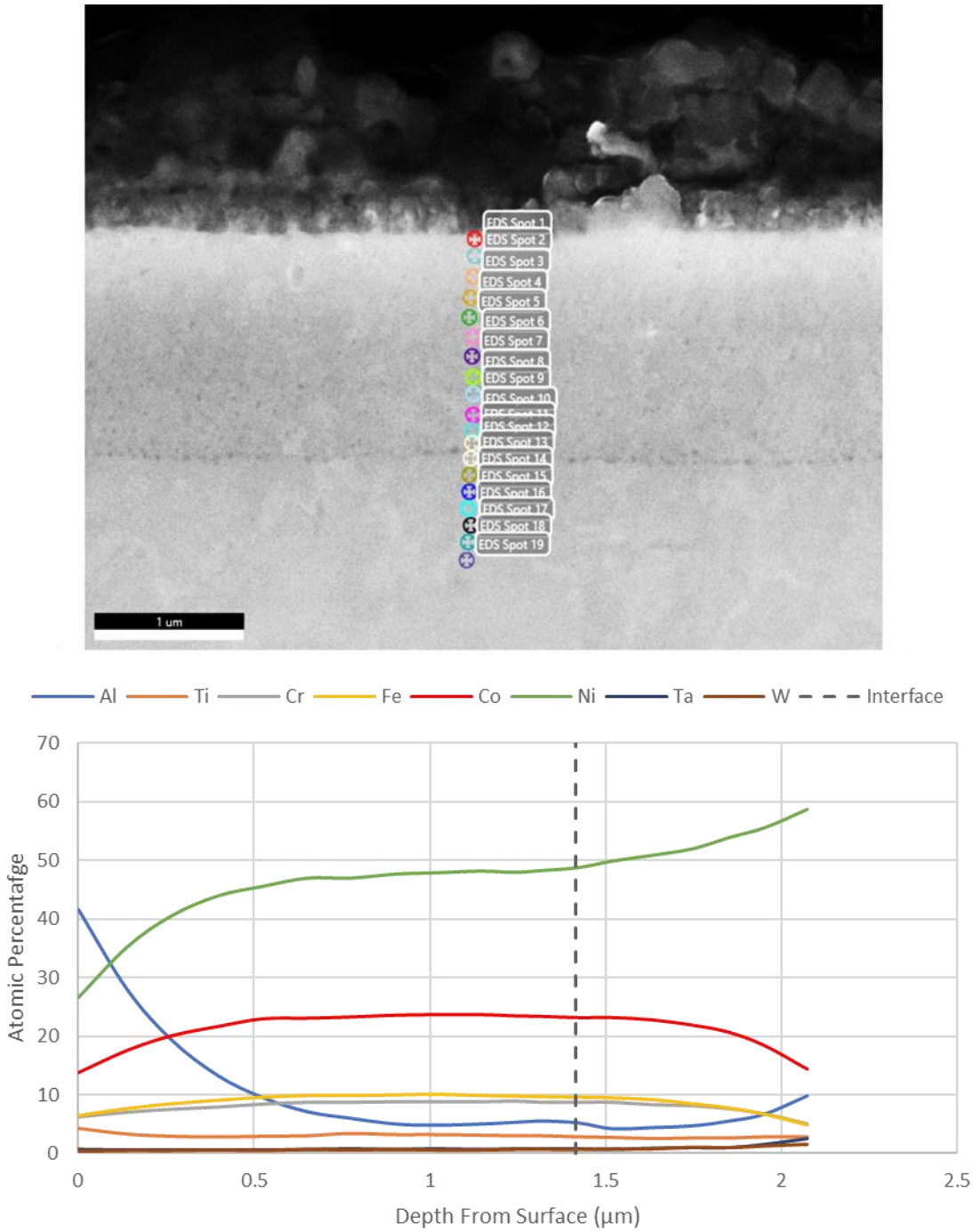

Figure C-5: (a) SEM image of the region of analysis and (b) corresponding EDS composition profile for an annealed Series 2 coating deposited at 15 mTorr. Center of substrate plate.

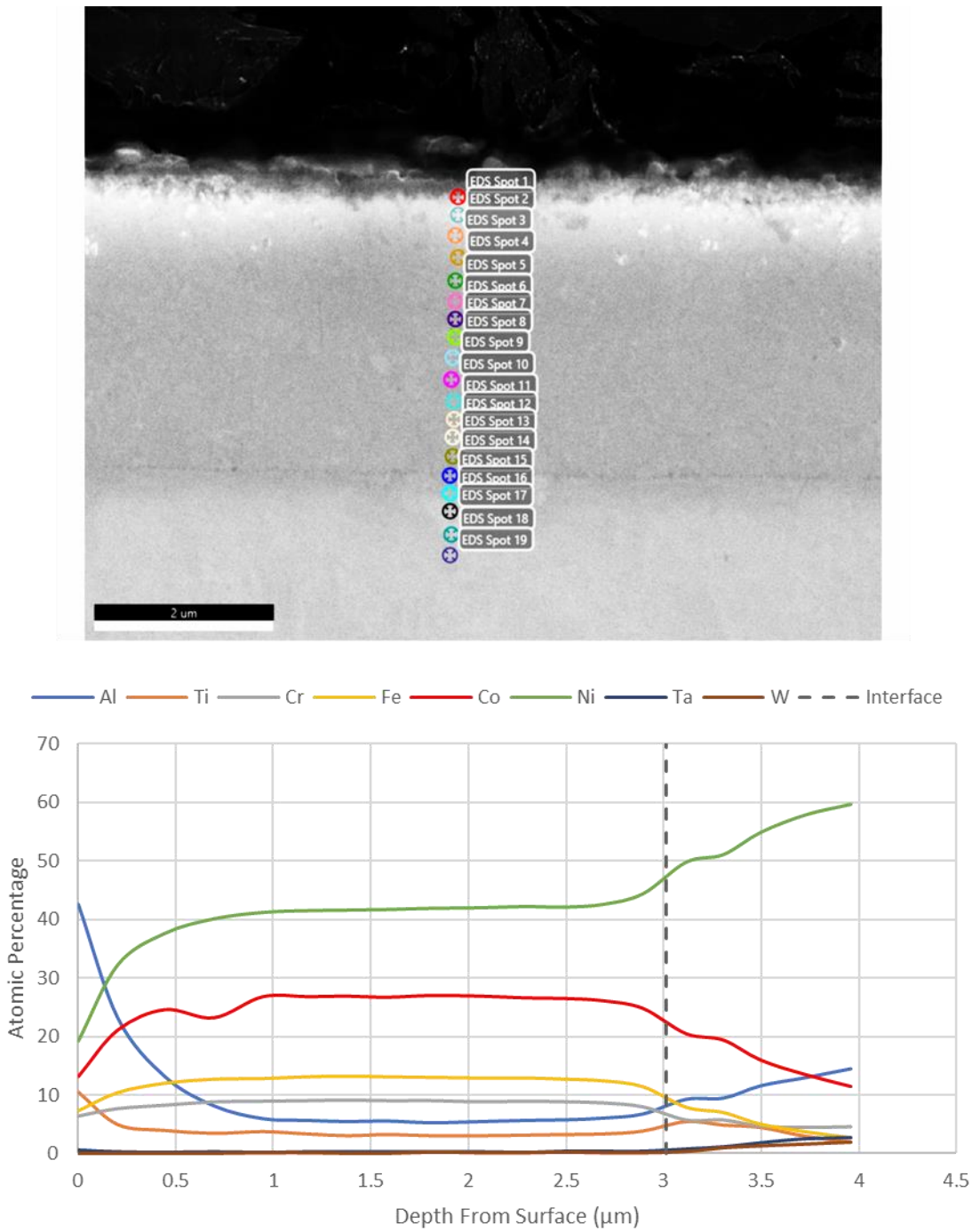

Figure C-6: (a) SEM image of the region of analysis and (b) corresponding EDS composition profile for an annealed Series 2 coating deposited at 15 mTorr. Position 2 of substrate plate.

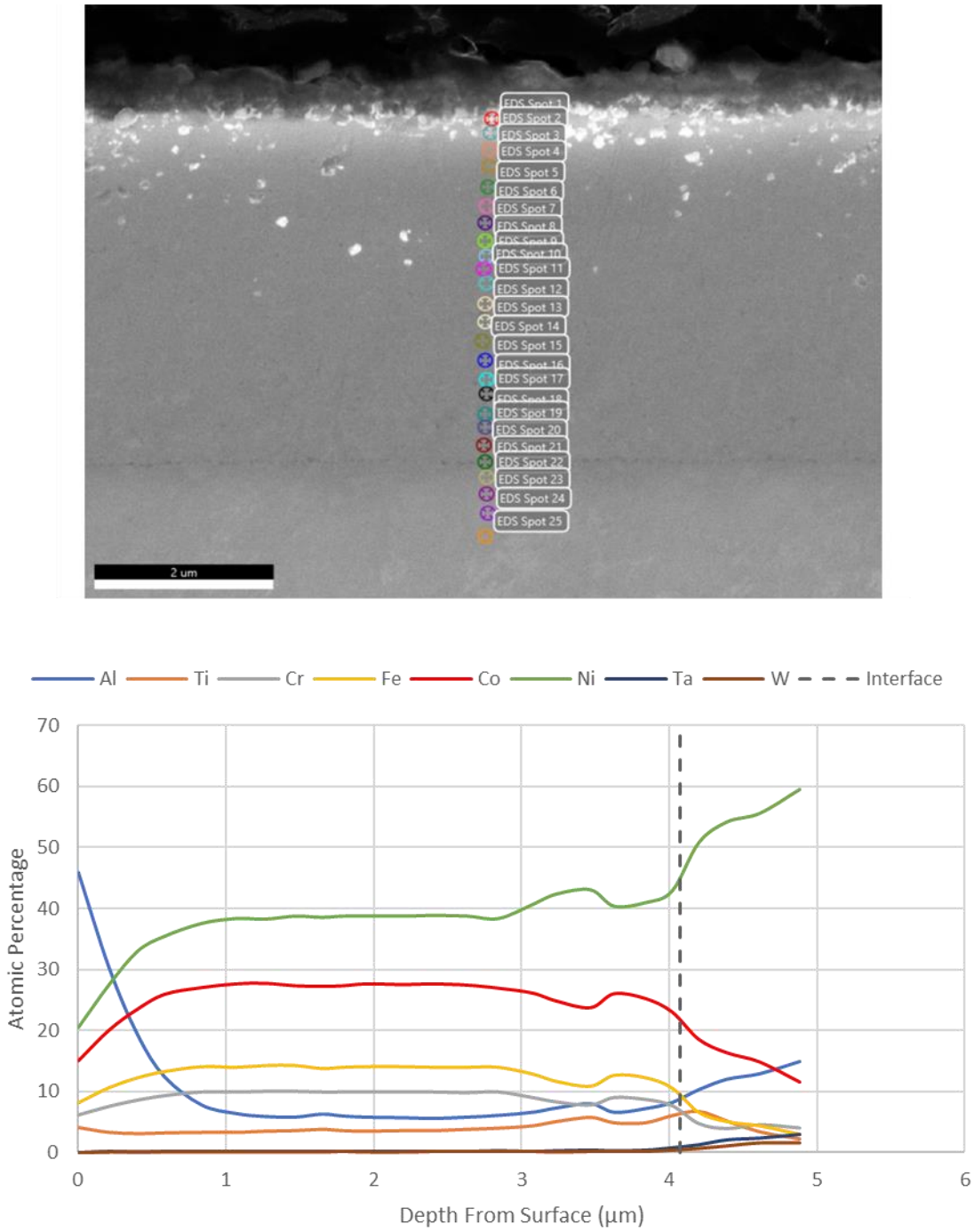

Figure C-7: (a) SEM image of the region of analysis and (b) corresponding EDS composition profile for an annealed Series 3 coating deposited at 15 mTorr. Position 2 of substrate plate.

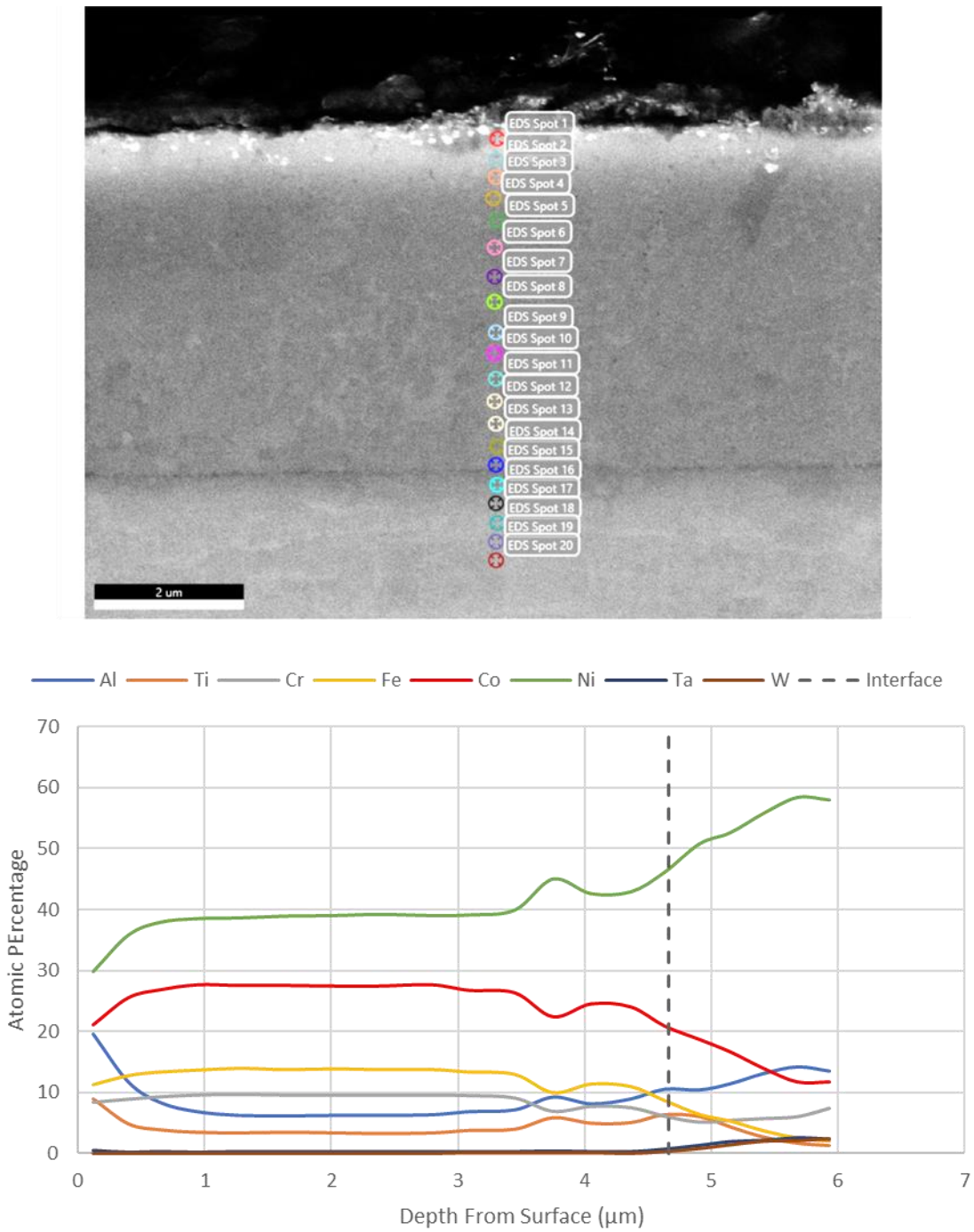

Figure C-8: (a) SEM image of the region of analysis and (b) corresponding EDS composition profile for an annealed Series 2 coating deposited at 15 mTorr. Edge of substrate plate.

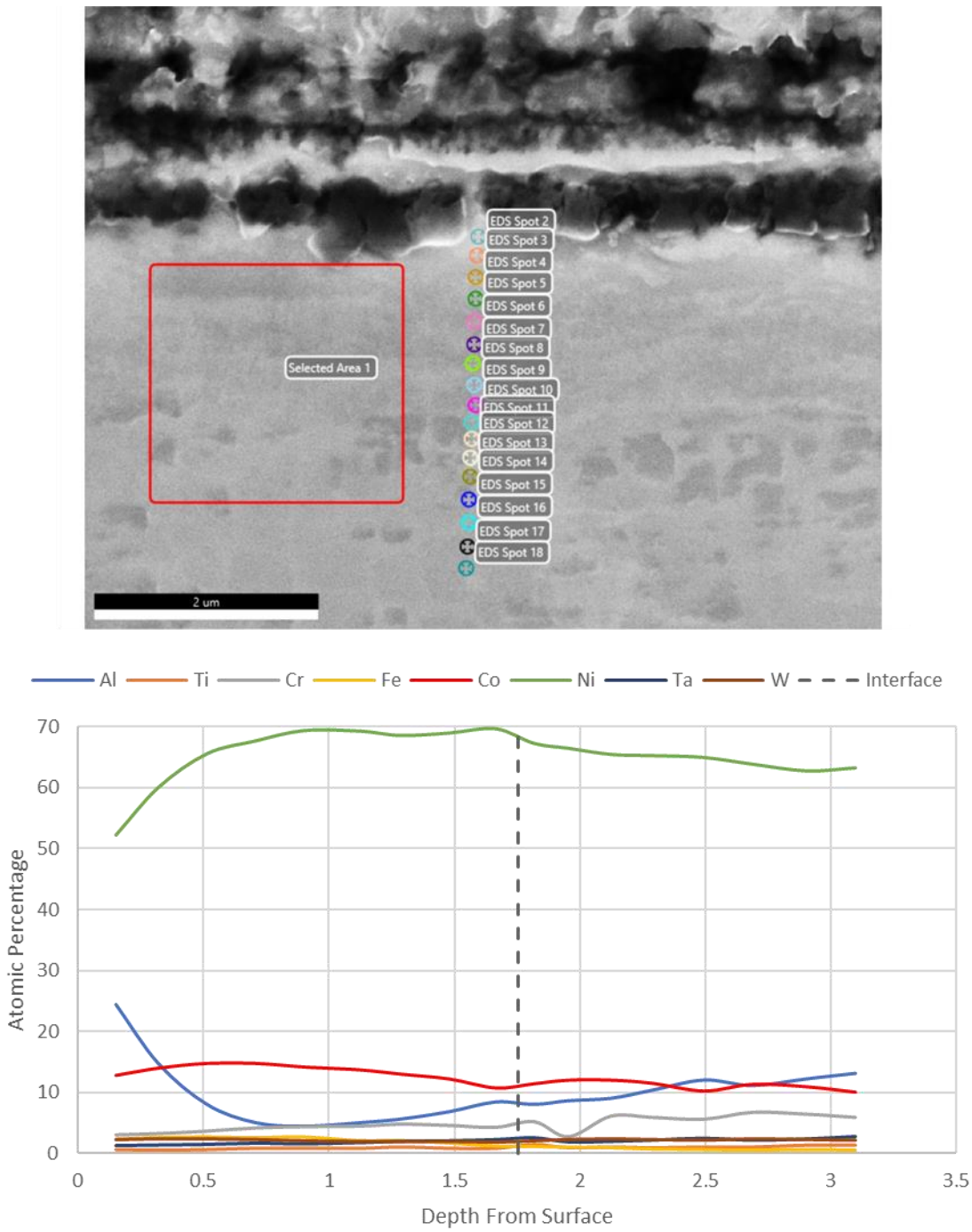

Figure C-9: (a) SEM image of the region of analysis and (b) corresponding EDS composition profile for an annealed Series 2 coating deposited at 30 mTorr. Center of substrate plate.

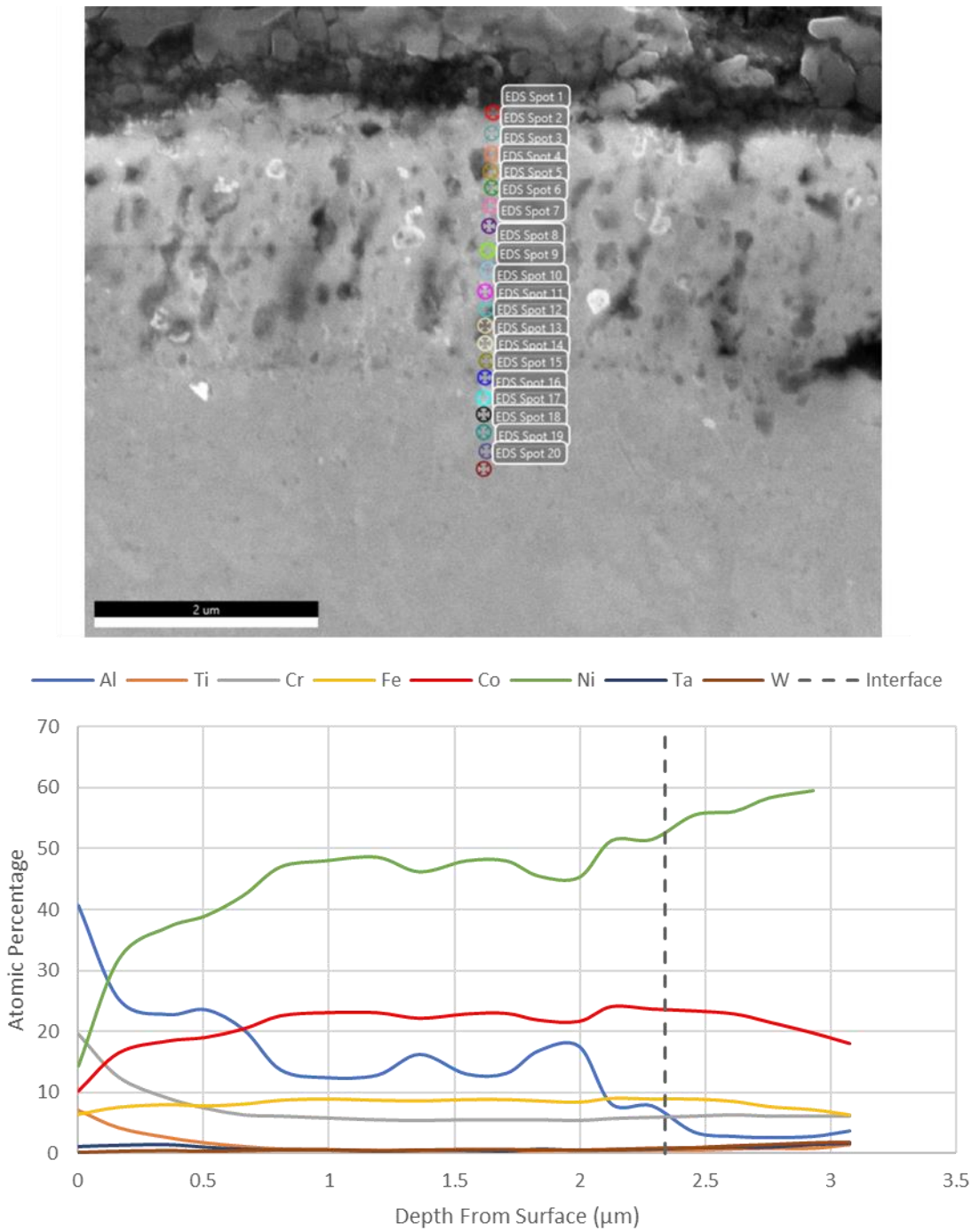

Figure C-10: (a) SEM image of the region of analysis and (b) corresponding EDS composition profile for an annealed Series 2 coating deposited at 30 mTorr. Position 2 of substrate plate.

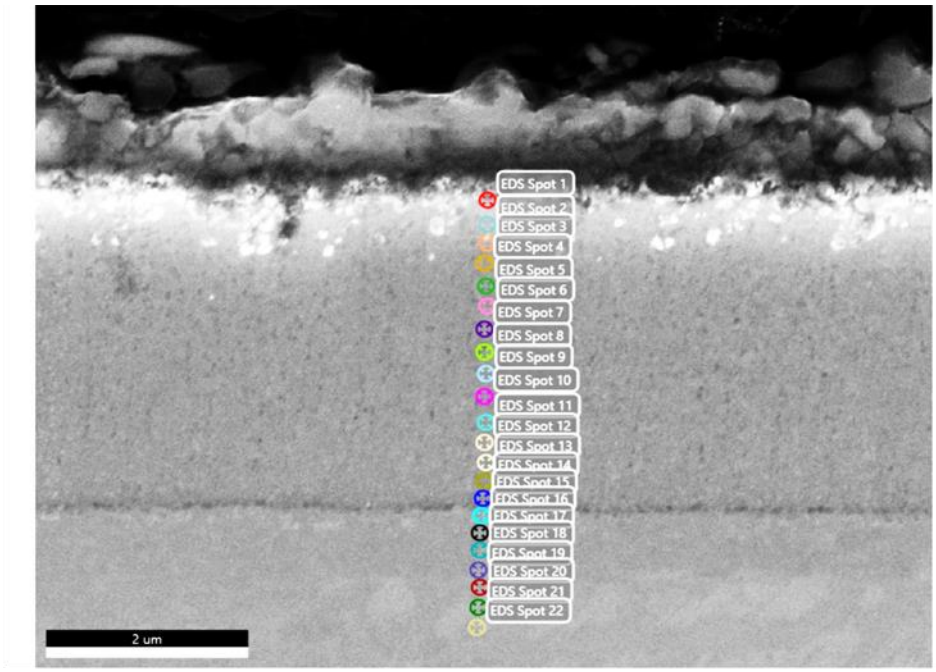

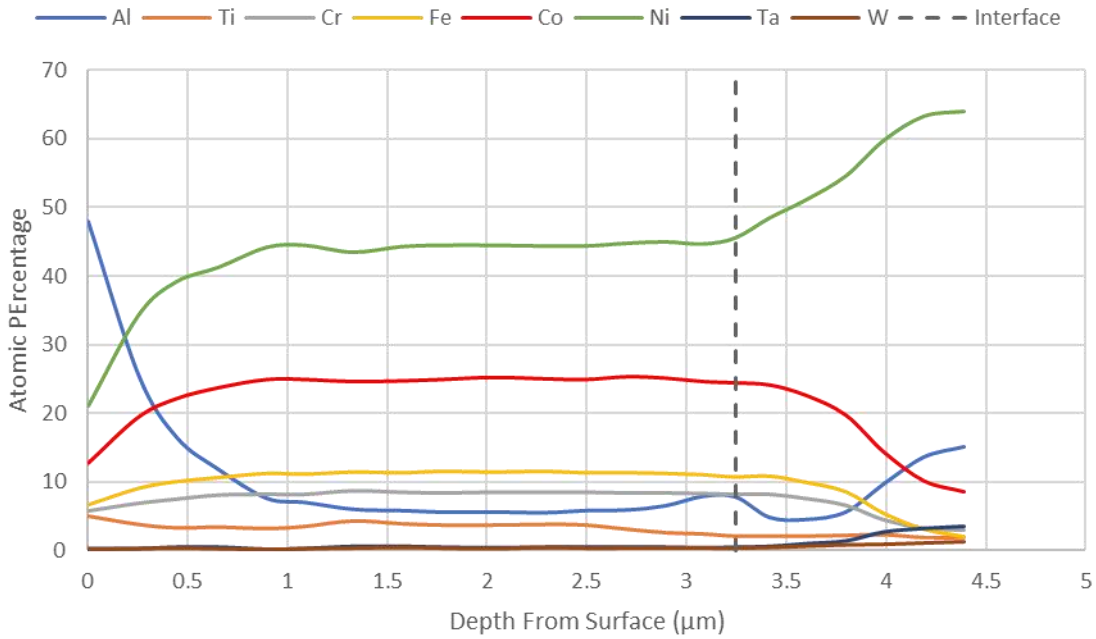

Figure C-11: (a) SEM image of the region of analysis and (b) corresponding EDS composition profile for an annealed Series 2 coating deposited at 30 mTorr. Position 3 of substrate plate.

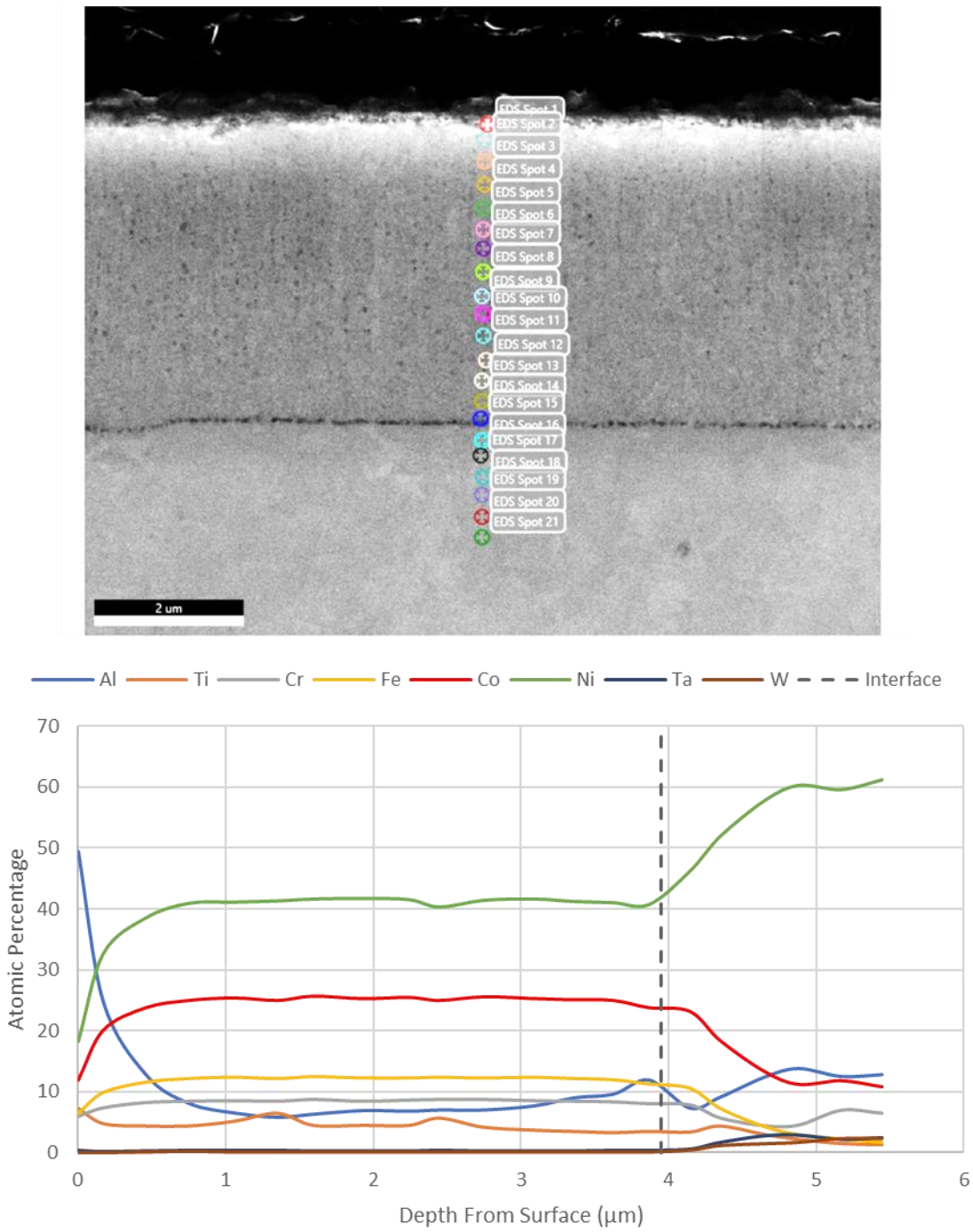

Figure C-12: (a) SEM image of the region of analysis and (b) corresponding EDS composition profile for an annealed Series 2 coating deposited at 30 mTorr. Edge of substrate plate.

APPENDIX D: SHORT OVERVIEW OF STRUCTURE ZONE MODELS IN PVD

Structure zone models (SZMs) are widely used to classify the morphologies of thin films and coatings deposited via physical vapor deposition processes. An establishment of the central phenomena responsible for the formation and evolution of structure along with their dependencies on processing parameters allow for the construction of SZMs.

The initial SZM was proposed by Movchan and Demchishin to describe the changes in surface morphology in some evaporated metal (Ni, Ti, and W) and ceramic (Al_2O_3 and ZrO_2) films in terms of their homologous temperature T/T_m, where T is the deposition temperature and T_m the melting temperature of the material being deposited, both in degrees Kelvin [134]. The SZM, shown in Fig. D-1, has three zones, each displaying a characteristic morphology (i.e., feature size, shape, and arrangement of phases).

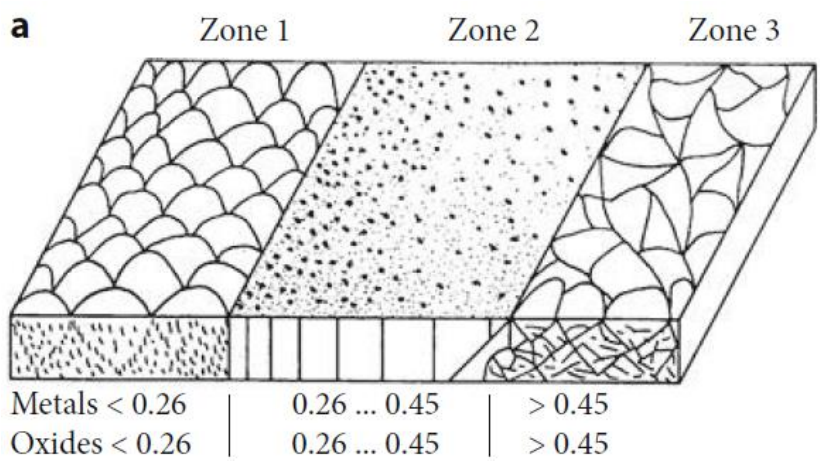

Figure D-1: Structure zone model proposed by Movchan and Demchishin for classification of thick film morphologies produced via thermal evaporation [134].

These same zones have also been found to occur in sputter deposited films. Thornton extended the Movchan and Demchishin model to sputter deposition by adding deposition

pressure as a variable to describe the influence of adatom mobility caused by energetic particle bombardment [25,120]. Thornton's SZM is shown in Fig. D-2.

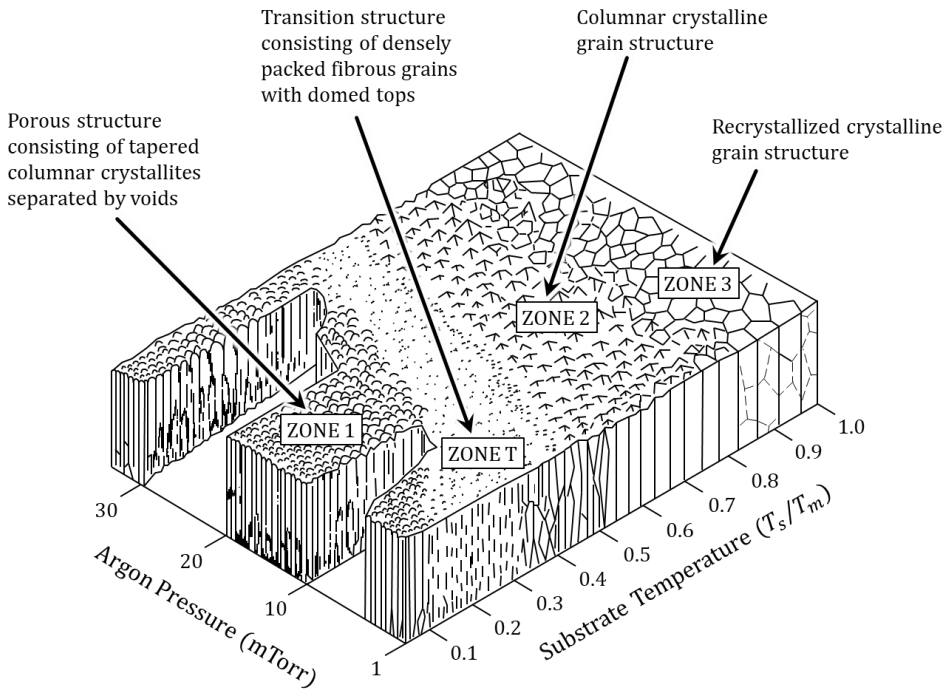

Figure D-2: Structure zone model for predicting coating morphology. This figure was adapted from Thornton [25].

Zone 1 structures are observed in amorphous and in crystalline films. They are a direct result of limited adatom mobility (and thus limited surface diffusion) which allows shadowing effects to dominate growth. Zone 1 films and coatings are composed of fibrous columns separated by networks of tapered voids with rough, convoluted and cauliflower-like surface morphologies. The void networks are hierarchical, often extending all the way from the substrate plane to the film surface. In terms of properties, metallic Zone 1 films are mechanically hard, are often in a tensile stress state, and are prone to high rates of chemical diffusion. Ceramic films produced in this regime tend to softer than films produced with other morphologies.

Zone 2 films exhibit columnar morphologies but with dense, well-defined grain boundary arrays and increased grain widths. This is because adatom mobility is higher resulting in increased surface diffusion which densifies the intercolumnar boundaries. In this regime, the films often develop faceted surface features and will exhibit very strong crystallographic textures. In thick coatings, the columns do not necessarily run from the substrate surface all the way to the coating surface. The properties of Zone 2 films are often comparable to those of bulk materials. In terms of diffusion and chemical attack, Zone 2 films are expected to be more resistant than Zone 1 due to higher density and reduced grain boundary area.

Zone 3 structures have been found to consist of near-equiaxed recrystallized grains due to the occurrence of bulk diffusion and recovery processes. In terms of properties, Zone 3 structures tend towards those of large grained recrystallized bulk materials. Further increases in the resistances to diffusion and chemical attack are expected due to reduced grain boundary area and increased density. Mechanically, these structures lead to properties that are like those of fully annealed bulk materials.

Thornton's model includes a transition zone between Zones 1 and 2. In this zone, called Zone T, surface diffusion governs film morphology just as it does in Zone 2. The films maintain the fibrous/columnar grain morphology of Zone 1, but the grains were more densely packed together with "fine-domed" surfaces and did not extend through the film thickness. The resulting films tend to be in a compressive stress state, and to exhibit smoother top surface morphologies. Internally, voids are still present (as in Zone 1) but the void networks are nonhierarchical with no direct connection between the substrate plane and top surface. At higher deposition pressures a matchstick-like morphology occurs within Zone T, often labeled Zone M

[124]. This zone is included in the SZM in Fig. D-3. Zone T films tend to be harder than Zone 1 coatings and are more resistant to diffusion or chemical attack than Zone 1.

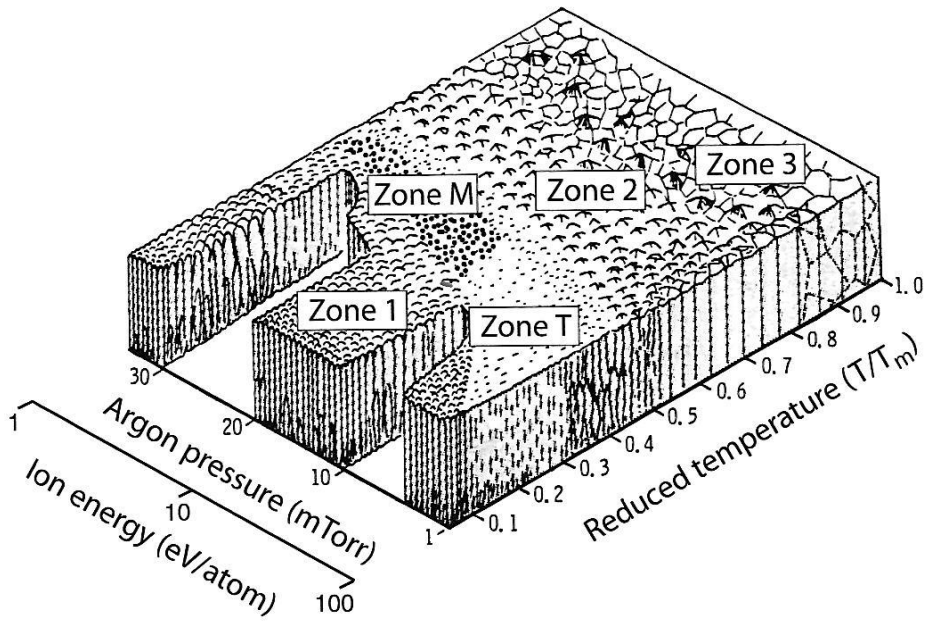

Figure D-3: Structure zone model that includes Zone M [124].

Though only qualitative in nature, SZMs are still widely used to estimate thin film morphology under specific deposition conditions. Messier et al. have further developed the SZM by incorporating substrate voltage bias and film thickness [56] (Figure D-4). Their proposed SZM illustrates the effects of both bombardment-induced and thermal-induced mobility. Increasing temperature and/or bombardment causes the rate of evolution of the dominant morphology (i.e., the average size of the morphological features) to decrease. They additionally considered how films evolved as thickness increased, resulting in an evolutionary SZM that predicts a surface morphology size that is almost linearly related to film thickness by a power of approximately 3/4 of the film thickness.

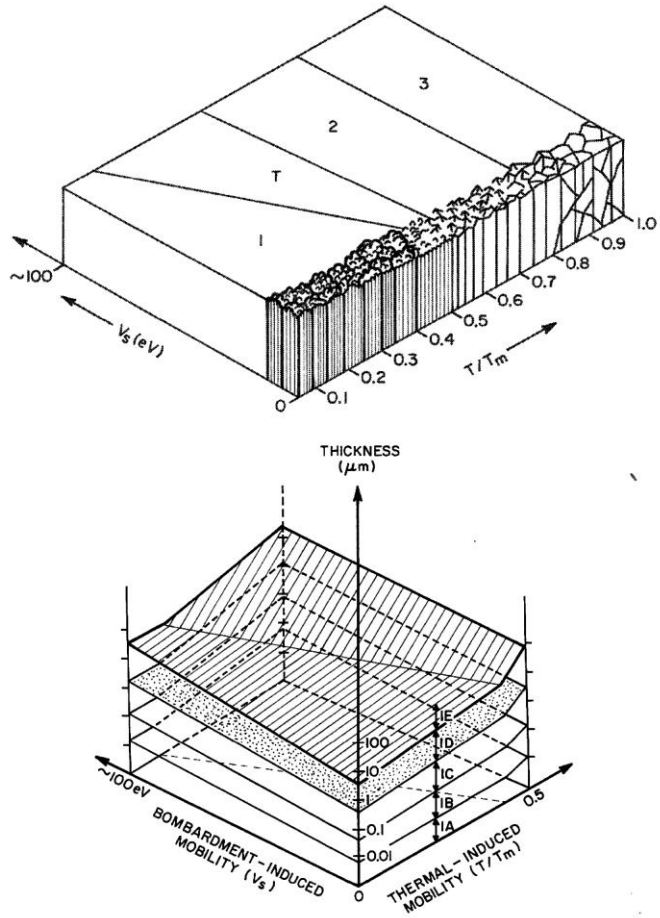

Figure D-4: Messier's modification of Thornton's SZM showing the expansion of Zone T with increasing bombardment. For radio-frequency (RF) sputtering, the substrate self-bias potential V_s increases as gas pressure decreases. The bottom figure shows the rate of column expansion with increasing thickness [56].

Grovenor et al. have offered a SZM for evaporated thin films that considers grain boundary diffusion to be the dominant process controlling grain structure in Zones T and 2 (Figure D-5). They additionally proposed that thicker Zone 2 morphologies would evolve due to the onset of granular epitaxy coupled with grain (i.e., column) growth [51].

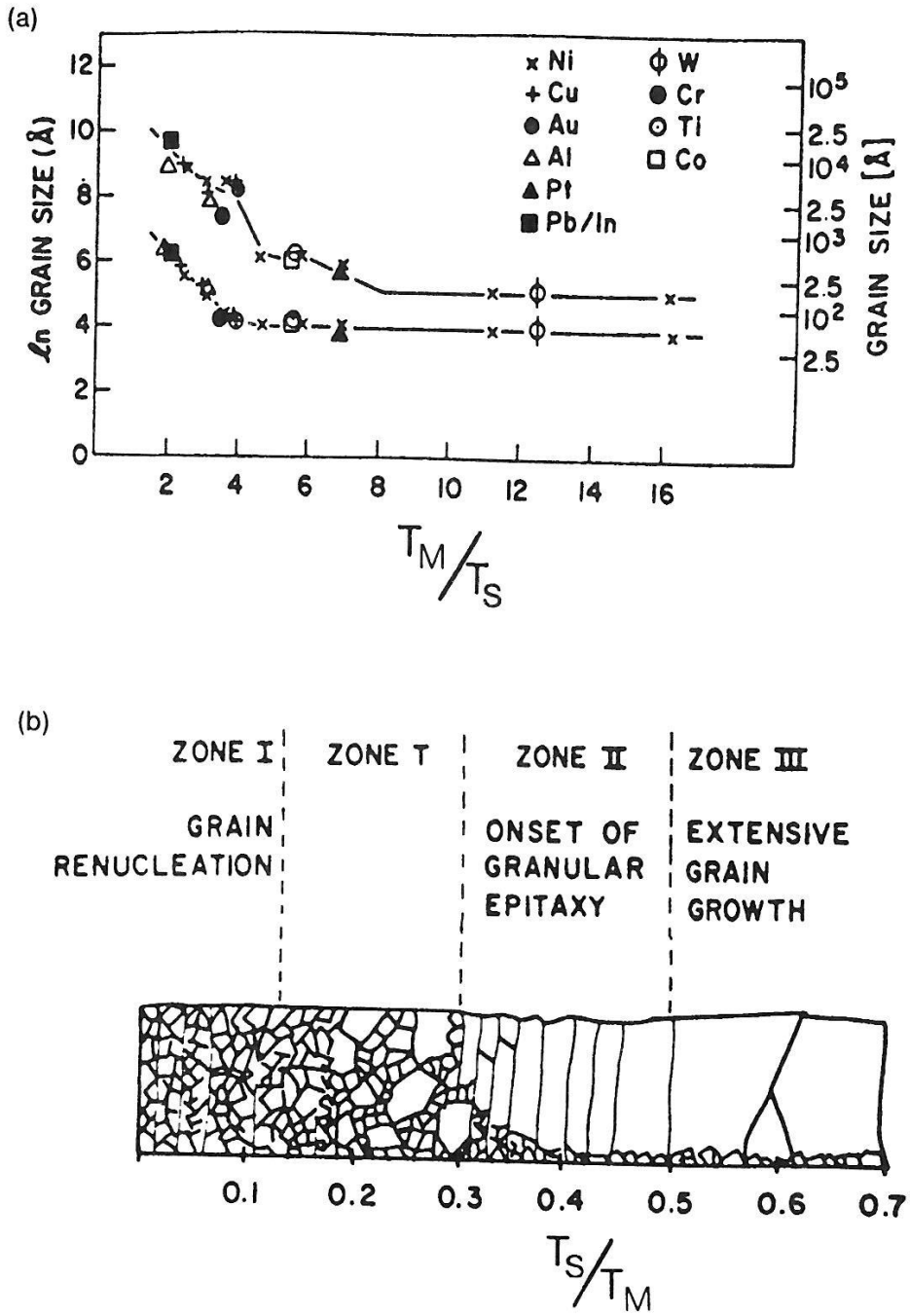

Figure D-5: Grovernor's SZM for evaporated metal films [51]. (a) Plot of maximum and minimum grain size variation with homologous temperature for various metals. (b) SZM for evaporated metal films.

Barna and Adamik have developed a model that integrates the concentration of impurities (co-deposited additives) as an additional factor controlling film morphology. This resulted in

their postulate of ‘real’ SZMs that could represent temperature-dependent structures as functions of impurity concentration [49]. Higher impurity contents would lead to enhanced tendencies for impurity segregation to grain boundaries, which in turn leads to the formation of smaller grains and a change of the growth morphology to a lower zone of the SZMs.

Similarly, Kelly and Arnell have published SZMs for Al, Zr, and W films deposited via closed-field unbalanced magnetron sputtering in terms of coating pressure, substrate bias voltage, homologous temperature, and ion-to-atom ratio incident to the substrate [135]. In unbalanced magnetron sputtering the magnets are configured such that magnetic field lines, and thus the plasma, are directed towards the substrate. The enhanced bombardment provided by this arrangement leads to higher rates of deposition and enhanced density. This model reports the same structures as Thornton but shifts them to lower homologous temperatures than observed in traditional sputtering systems.

More recently, Kusano has revisited SZMs for Ti, Zr, and Hf thin films and their corresponding oxides as functions of homologous temperature and Ar discharge gas pressure [53-55]. These investigations reiterated the validity of the original SZM concept, particularly the dependence on homologous temperature. Kusano additionally offered that replacing the traditional discharge pressure axis with that of energy transferred per particle to the surface of the growing film along with the incorporation of synergistic effects could allow one to more comprehensively describe the changes in film morphology that occur under different deposition conditions [55]. Kusano additionally notes that the effects of oblique incidence (aka shadowing effects) must also be integrated in to SZMs.

The mechanisms leading to the formation of columnar grain structures has been studied for decades. In his book, Ohring describes this morphology as a microstructure consisting of

networks of low density material surrounded by arrays of parallel rod-shaped columns of higher density [125]. The geometries of columnar grains formed via evaporation have been found to follow the so-called tangent rule:

$$\tan \alpha = 2 \tan \beta \tag{D-1}$$

In this equation β is the angle between the column axis and the substrate normal (i.e., tilt angle of columns) while α is the angle between the vapor flux (i.e., source direction) and the substrate normal (i.e., zenithal evaporation angle). In general, β is smaller than α. Barranco et al. note in their review on oblique angle deposition that the fundamental factors that establish the tilt angle is still undetermined and depends on the chemical nature of the material being deposited, along with the characteristics of the deposition reactor [131].

Mukherjee and Gall have devised an SZM to account for the angle of incidence during sputter deposition [126]. Like regular SZMs, their model showed a progressive change in morphology with increasing homologous temperature. However, the competition between surface diffusion and atomic shadowing gives rise to the formation of distinct zones with increasing temperature consisting of rods, columns, protrusions and equiaxed grains with whiskers rather than the traditional Zones 1, 2, and 3 observed at normal incidence. Careful control of the angle of sputter incidence and substrate motion have been used to generate sculptured thin films with tailored crystal and void morphologies. This process is often termed oblique angle deposition. The principles of oblique angle deposition and sculptured thin films are captured in the 2005 book by Lakhtakia and Messier and in the 2016 review by Barranco et al. [124,131].